Performance of Pillars in Rock Salt Mines

by

Linda I Hein Lau

A thesis
presented to the University of Waterloo
in fulfillment of the
thesis requirement for the degree of
Master of Applied Science
in
Civil Engineering

Waterloo, Ontario, Canada, 2010

AUTHOR'S DECLARATION

I hereby declare that I am the sole author of this thesis. This is a true copy of the thesis, including any required final revisions, as accepted by my examiners. I understand that my thesis may be made electronically available to the public.

Abstract

The viscoelastic and creep properties of salt create challenges in the design of salt mines. Salt undergoes steady state creep for a long period of time, and the time of failure is not easily predicted. Developing functions for creep behavior is important in predicting the deformation of salt pillars. Through literature reviews, it was found that there are many relationships to determine the deformation rate of salt specimens through constitutive models. Mine panels have also been modeled to understand the stress and deformational behavior of the pillars. The purpose of this was project was to develop a relationship that determines the convergence rate from knowing the pillar width to pillar height ratio and thickness of the salt strata immediately above and below the mine.

The third power law was adopted in the modeling of salt pillars, which is applicable to low stresses of less than 10 MPa that is typical of salt mine conditions. The finite difference software, FLAC3D was used for the simulations of salt pillar models. A square pillar was modeled using four pillar width to pillar height ratios from 1.5 to 4.6. In mining practices, the pillar width to pillar height ratios are designed to be 1.0 to 5.0. Three sets of pillar dimensions were used for each pillar width to pillar height ratio, this was done to determine whether different room and pillar dimensions for each pillar width to pillar height ratio resulted in different convergence rates. Eight salt thicknesses of 0 m to 26 m were modeled for each set of pillar dimensions, which was sufficient to determine the effect of salt thickness on convergence rate.

From the modeled results, general trends among the various pillar width to pillar height ratios were observed. The convergence rate increased as the pillar width to pillar height ratio decreased. In addition, an exponential relationship was found between the convergence rate and the pillar width to pillar height ratio. There was a strong correlation between convergence values calculated from the developed function and the modeled values for the power law exponent of three. The developed expression can be used to estimate the convergence rate due to pillar compression and room convergence.

Acknowledgements

I would to thank my supervisor, Professor Leo Rothenburg for all of his guidance and assistance in my research.

Table of Contents

List of Figures

List of Tables

Chapter 1 Introduction

Many factors need to be taken into consideration when designing a salt mine using the room and pillar method. The viscoelastic creep properties of salt cause many difficulties in the design of a mine. The time dependent deformation of salt has been researched by many scholars since the late 1800s for various salt mines in an attempt to create a reliable time-deformation predictive model. The behavior of salt pillars and rooms has been investigated through monitoring deformation measurements and calculating approximate stress values; and the deformations of salt pillars and rooms have been used to assess the stability of a mine.

The importance of salt mining has increased due to the high demand of this resource especially potash. Salt is not only used for human consumption, but it can also be used as a fertilizer. One of the variations of salt is sodium chloride which is mainly used for human consumption. Salt type material refers to materials that exhibit viscoelastic and creep properties. Some examples of salt material are carnallite, sylvinite, and tachyhydrite. The creep properties and creep law can be applied to each type of salt material.

Many researchers have developed formulas to determine the optimal dimensions of salt pillars and rooms for stability, and they have found that the ratio between pillar width and pillar height plays an important role in maximizing the safety and profitability of a mine. Empirical functions have also been developed to quickly and easily assess underground mine conditions. These functions usually contain pillar dimensions, average stress, and/or horizontal stress.

The dimensions of rooms and pillars are restricted to the capabilities of machinery and to the required extraction ratios. The general behavior of salt pillars and excavated rooms do not change between location sites, and the empirical relationships for all locations take the same form. However, the coefficients in the functions vary greatly between site locations. These functions predict the strain using variables of time and effective stresses, which is dependent on the depth of the pillars and the overburden material. Salt material has been tested in the

laboratory and in the mine. It has been found that laboratory results do not always reflect the findings in in-situ measurements, and this is due to different loading and confinement conditions.

Mechanical and physical properties of salt and the general behavior of salt pillars are described in this report. The objective of this research was to find an empirical relationship between convergence rate and the salt thickness above and below a salt mine. The mesh generator RECTPIL and the finite difference software FLAC3D were used to perform three dimensional analyses on the adopted salt pillar model. Pillar width to pillar height ratios and material properties were based on literature reviews and selected for simplicity.

The modeled results were used to develop the final expression that relates the pillar width to pillar height ratio and the salt thickness immediately above and below the mine to the convergence rate. The final function was not compared to laboratory measurements, but the patterns and trends found in the modeled results matched observations made by other researchers.

1.1 Thesis Organization

The organization of this thesis is presented in this section. The contents in Chapter 2 to Chapter 4 present the theoretical background and literature review of salt in order for better understanding of the researched material. Chapter 2 and Chapter 3 present the physical properties of salt and the associated creep laws. These two chapters present the main properties that create challenges in the design of salt mines. The justification for using the adopted creep laws in this project are presented in Chapter 3. Chapter 4 describes the convergence of rooms in salt mines in detail and the factors those influence this parameter. The Varangeville salt mine was used as an example to depict stress behavior, and the importance in investigating the convergence rate of salt rooms. The Saint-Maximilien mine panel of the Varangeville salt mine collapsed due to large loads that exceeded the bearing capacity of the pillars. The mechanisms that caused the collapse are described in detail in this chapter.

The literature review of past analyzed salt mines and the results of previous laboratory testing are presented in Chapter 5. There is extensive research completed in salt mining and salt properties, and only a select few research findings are presented in this thesis

The methodology used in the modeling of a salt pillar, and the method of analyses of the results from FLAC3D are presented in Chapter 6. Background information and calibration processes of the software used in this project are also presented in Chapter 6. The results obtained from FLAC3D are summarized and presented in Chapter 7. The conclusions and recommendations are presented at the end of the thesis.

Chapter 2 Properties of Salt

The term salt is not always restricted to halite or sodium chloride. Salt type material can refer to any material that exhibits creep properties. Salt has both elastic and viscous characteristics which allow it to have properties of hysteresis, stress relaxation, and creep. These properties give salt formations the ability to expand and contract as well as flow when given the space and time to do so. The time dependent deformation of salt causes difficulties in determining the convergence of salt pillars. Therefore, it is important to examine these properties before further experiments are performed or conclusions are drawn. The three stages of creep are primary creep, secondary creep, and tertiary creep. The rheological behavior of salt can be described by a generalized Kelvin model to explain its viscoelastic properties.

Halite and potash are one of the major types of salt material, and some of their properties are introduced in this chapter. The mechanical properties, rheological models, the stages of creep for salt, and Munson's mechanism map illustrating the micromechanics of salt are also presented in Chapter 2. This chapter provides the background information on the researched material.

2.1 Halite and Potash

Halite is a colorless mineral with a density of 2.16 g/cm^3. It has a low permeability of 10^{-21} m^2 to 10^{-19} m^2, and a low porosity of 0.05. Due to the low porosity and permeability of salt, salt can be used for dry storage in mined salt repositories, underground storage of fluids, and waste disposal of toxic and non-toxic solid wastes. The Young's modulus of salt is approximately 30 GPa (Jeramic, 1994). Halite is mined from evaporite deposits from all parts of the world, and some of the largest deposits are in California, Utah, Saskatchewan, and Poland. There are many shapes and forms of salt deposits, but the four main geological environments are sedimentary with tabular structure, flexural structures due to tectonics, domes created from diapiric processes, and vein-like structures originating from internal tectonics of deformed salt bodies (Jeramic, 1994).

Potash is the common name for various mined and manufactured salts with potassium in the water soluble form (Wikipedia, 2010). The common resources for potash are carnallite and sylvite. Some of the world's largest potash deposits are in Saskatchewan, Brazil, Germany, and Carlsbad, New Mexico. Potash is mostly used in fertilizers, with some uses in water softeners, ceramics, and explosives (Wikipedia, 2010). Carnallite and sylvite are both salt type materials, and they are important resources for potash. Carnallite is a hydrated potassium magnesium chloride $KMgCl_3 \cdot 6(H_2O)$, and it has a density of 1.60 g/cm^3. The color can vary from yellow to white, red, blue, and colorless. Carnallite must be stored in an air tight container because this mineral absorbs the moisture in the surrounding air. The geologic setting for this mineral is the upper layers of the marine saline deposits (Carnallite, 2010). Sylvite (KCl) has an isometric system similar to halite, and it is primarily used as a potassium fertilizer. It has a density of 2.00 g/cm^3. Sylvite is found in very dry saline areas because it is one of the last evaporite minerals to precipitate (Wikipedia, 2010). Sylvite occurs in sedimentary basins evaporites, and it sublimates in volcanic fumaroles (Sylvite, 2010).

2.2 Rheological Model of Salt

The Kelvin model is used to represent many creep materials. A Kelvin rheological model describes a material deforming at a decreasing rate while approaching steady state strain asymptotically under a constant stress. The material then returns to its undeformed state when the stress is removed. The Kelvin element is an elastic spring in parallel with a Newtonian damper, and a second spring element is connected to the Kelvin element in series to create the generalized rheological model of salt (Jeremic, 1994). Figure 1 is the rheological model of salt.

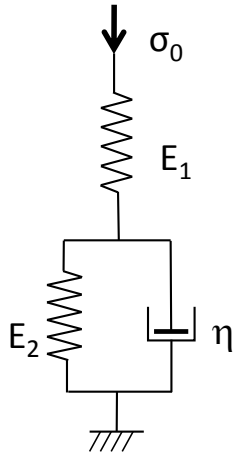

Figure 1. Rheological model of salt (Jeramic, 1994)

Where, σ_0 is an applied constant stress, K is an elastic spring, and η is a dashpot. This model only represents the primary and secondary creep of salt. The classical rheological models do not describe the tertiary stage well, where there is sudden failure after accelerating creep. Some simple functions can be generated from the understanding of the rheological model. The instantaneous strain can be calculated at time zero by the ratio of the constant stress to the elastic element.

$$\varepsilon_0 = \frac{\sigma_0}{E_1} \tag{1}$$

The viscous strain can be calculated by the following function (Jeramic, 1994):

$$\varepsilon = \sigma_0 \left[\frac{1}{E_2} + \frac{1}{E_1}(1 - e^{-\frac{t}{t_1}})\right] \tag{2}$$

Since the generalized Kelvin model only describes the transient and steady state creep stages, this model approaches a viscous strain value asymptotically after a long period of time. In underground mining, the salt pillar is represented by Figure 2. Figure 2 represents a material with steady state creep behavior with no creep recovery. The rheological model in Figure 2 was used in the modeling of salt pillars in this project.

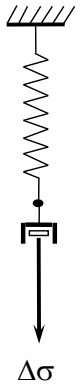

Figure 2. Rheological model of a salt pillar

Salt pillars in underground mining cannot be modeled solely based on the simplicity of rheological models because salt pillars and rooms exist, which complicates the known rheological models of salt. According to Mraz (1972), once salt or similar creep material is excavated, the material responds non-elastically depending on the confinement conditions and the in-situ pressure differential.

2.3 The Three Stages of Creep

A material will deform through three stages under constant load, and each stage undergoes a different type and rate of strain. Figure 3 is the creep curve simplified from Jeramic (1994) showing how the strain rate changes with time for metals and plastics.

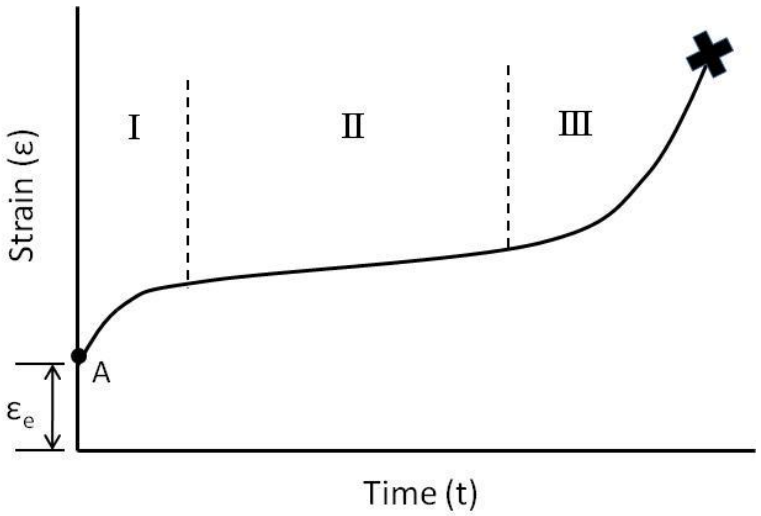

Figure 3. Typical creep curve of metals and plastics (modified from Jeramic, 1994)

When a load is first applied to a material, instantaneous elastic strain occurs that is not dependent on time and produces point A. Primary or transient strain then follows the instantaneous elastic strain which is shown as Region I. The deformation rate decreases until it remains constant and enters Region II, which is the secondary creep or steady state creep. Region III is the tertiary creep or accelerating creep that leads to the sudden failure of the material. The creep behavior of salt is different from metals and plastics. Salt only exhibits the transient and steady state creep stages, but not the tertiary creep stage. Figure 4 illustrates the typical creep curve for salt.

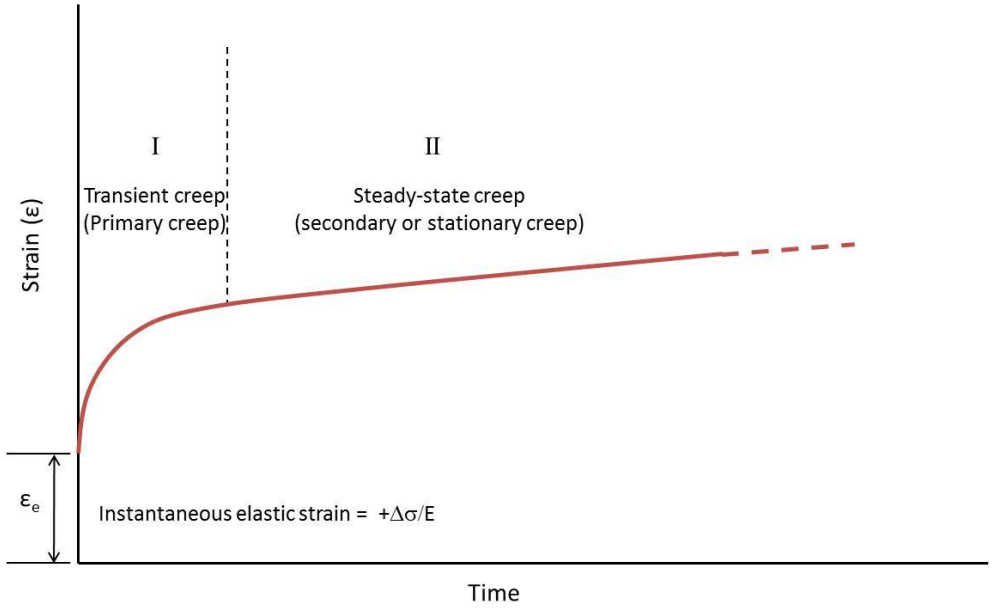

Figure 4. Typical creep curve of salt (Dusseault, 2008)

As illustrated in Figure 4, salt undergoes continuous deformation through time after the transient stage. 0.6 mm of deformation can occur in the first year for a salt mine. The transient stage may last up to two years, and the steady state creep stage occurs indefinitely.

Many equations were developed for the primary and secondary creep stages. These equations provide deformation information to predict when the material will fail. Each salt mine or each experiment will produce a different equation to determine the strain rate of salt due to different compositions of the material and loading conditions, but all equations will follow a similar form. According to Jeramic (1994), the following expression is the general form of the creep equation based on laboratory experiments and in-situ observations of scholars.

$$\varepsilon = e_t\ [1 - e^{-rt}] + \dot{\varepsilon}_s t \tag{3}$$

There are two components to the equation, the first term describes the primary creep and the second term describes the secondary creep. ε is the total creep strain; e_t and r are experimental fitting parameters which are different for each type of salt or a different salt mine; t is the time; and $\dot{\varepsilon}_s$ is the secondary creep rate. The secondary creep rate predicts a constant creep rate described by the following expressions.

$$\dot{\varepsilon}_s = A\sigma^n exp\left[\frac{-Q}{RT}\right] \quad (4)$$

Where, A and n are experimental fitting parameters, σ is shear stress, Q is the activation energy, R is the gas constant, and T is the absolute temperature. Temperature, humidity, and porosity can affect the creep rate of salt; therefore, experiments are conducted in rooms where temperature and humidity is constant, and salt samples are taken from the same mine panel to minimize inconsistencies in the material. In addition, different constants and coefficients are used for different sites and different compositions of salt.

2.4 Munson's Mechanism Map

Munson (1979) developed a deformation mechanism map to describe the deformations of rock salt at the micromechanics level, and it illustrates the major factors that control steady state creep at different levels of stress and temperature. The deformation mechanisms are caused by the dislocations within crystal and grain boundaries of salt. Dislocations are irregularities and crystallographic defects in a crystal lattice. Munson's mechanism map is shown in Figure 5.

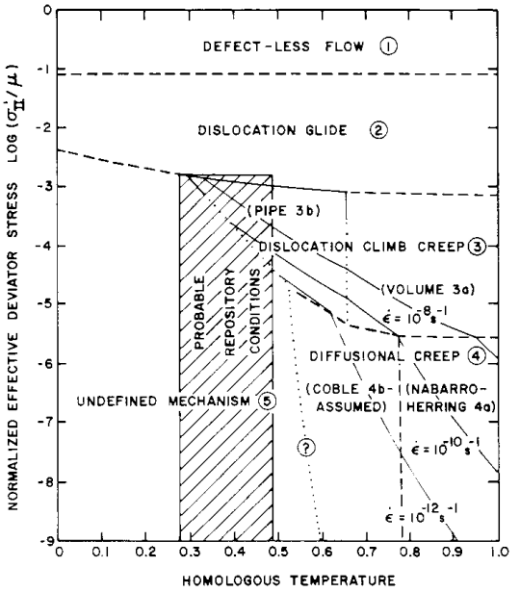

Figure 5. Munson's mechanism map (Munson, 1979)

Depending on the mining conditions, the controlling deformation mechanisms can vary. According to Munson (1991), steady state creep in underground mining of a repository is controlled by three main deformation mechanisms. The first one is the dislocation climb that occurs at low stresses and high temperatures; the second one is the undefined mechanism that occurs at low stresses and low temperatures; and the third one is the dislocation glide that occurs under high stress and all temperatures at rapid creep.

The dislocation climb is highly dependent on stress and can be represented by the Norton Power Law. The dislocation climb describes the alignment of dislocations and the formation of small boundaries at the sub-grain level. The dislocation glide is the increase in hardening and strength from dislocations moving through crystal grains and blocking the grains (Jeremic, 1994). The temperature and stress range of undefined mechanism has been observed in laboratory experiments, but the undefined mechanism did not describe a particular micromechanics system until recent. Costa, Poiate, Falcão, and Coelho (2005) found that the undefined mechanism describes the dissolution of salt under high pressures in between the salt grains.

The physical and mechanical properties were explored in Chapter 2. These properties are applicable to any salt type material, which exhibits viscoelastic and creep properties. The Kelvin model best represents the salt, but the salt pillars used for modeling were best represented by a spring in series with a dashpot. Salt type materials do not exhibit the tertiary creep stage like metals and plastics. Munson's mechanism map illustrated the deformation mechanisms for the steady state creep stage at various temperatures and stress conditions.

Chapter 3 Creep Laws

The single mechanism and two mechanism creep laws are explained in this chapter. Both laws have been adopted for a variety of salt specimens. Some examples are the single mechanism creep law was used for tachyhydrite from the Taquari-Vassouras potash mine in Brazil (Rothenburg, Carvalho Jr., & Dusseault, 2007), and the two mechanism creep law was adopted for the salt in the Palo Duro basin in Texas (Rothenburg, Dusseault, & Mraz, 2002).

3.1 Single Mechanism Creep Law

The single mechanism creep law has been adopted in many finite element models to calculate creep rates for salt behavior operating below 10 MPa of shear stress. Bachu and Rothenburg (2010) explained that a power function including shear stress is an assumption for the basis of the empirical relationship calculating for the steady state creep of salt. Shear stresses in salt are dissipated slowly as the time period increases due to the slow creep of salt, which results in the isotropy of initial and final stresses in salt. The single mechanism creep law is shown in the following:

$$\dot{\varepsilon_{ss}} = \dot{\varepsilon}_0 \left(\frac{\sigma}{\sigma_0}\right)^n \tag{5}$$

Where, $\dot{\varepsilon_{ss}}$ is the steady state creep; σ_0 is the transition stress; $\dot{\varepsilon}_0$ is the strain rate at σ_0; n is the power law exponents; and σ is the effective stress, which can be calculated from:

$$\sigma = \sigma_v - \sigma_H \tag{6}$$

Where, σ_v is the vertical stress and σ_H is the horizontal stress. The isotropy of initial and final stresses in salt can be rewritten as:

$$\sigma_v = \sigma_{H\,min} = \sigma_{H\,max} \tag{7}$$

The single mechanism creep law exhibit challenges where the effective stress is not always easily measured or determines in salt mines.

3.2 Two Mechanism Creep Law

A two mechanism creep law was derived later to include two deformation mechanisms. According to Rothenburg, Frayne, and Mraz (1993), two deformation mechanisms occur at typical mining conditions, the dislocation glide and the undefined mechanism. The two mechanism creep law can then be applied based on these two deformation mechanisms. The dislocation glide mechanism causes a decrease in the deformation of salt which describes the transient creep stage; and the undefined mechanism empirically describes the steady state creep stage. The two mechanism creep law is also the application of the Norton Law where there is a change in the power exponent at a certain stress level. The following expression is the two exponent creep law:

$$\dot{\varepsilon_{ss}} = \begin{cases} \dot{\varepsilon}_0 \left(\frac{\sigma_{eff}}{\sigma_0}\right)^{N_1} for\ \sigma_{eff} \geq \sigma_0 \\ \dot{\varepsilon}_0 \left(\frac{\sigma_{eff}}{\sigma_0}\right)^{N_2} for\ \sigma_{eff} < \sigma_0 \end{cases} \quad (8)$$

Where, $\dot{\varepsilon_{ss}}$ is the steady state creep; σ_{eff} is the effective stress; σ_0 is the transition stress; $\dot{\varepsilon}_0$ is the strain rate when the effective stress equals the reference stress; and N_1 and N_2 are the power law exponents. The power law exponents, reference stress, and the strain rate are parameters determined through laboratory testing and in-situ observations. The two mechanism creep law implies that a sharp change occurs between the dislocation glide mechanism and the unidentified mechanism which rarely occurs in practice. However, this law can simplify the calculations in predicting creep rate.

3.3 Creep Law Parameters

Creep law parameters are determined through laboratory experiments and computer modeling. The behavior of salt material does not change, but the coefficients of the creep laws do change. Creep tests are performed under a wide range of stresses to determine the corresponding strain rate. A creep test can take at least half a year and different stresses need to be tested for a set of samples which is not always feasible.

3.3.1 Power Law Exponents

One comprehensive set of uniaxial compression tests at low shear stresses were performed on Rocanville potash by Lajtai et al. (1988). An example of how the power law exponents are determined is shown in the following two figures. The steady state creep rate was plotted against the differential stresses on a logarithmic scale, and a direct least square fit was made for the data.

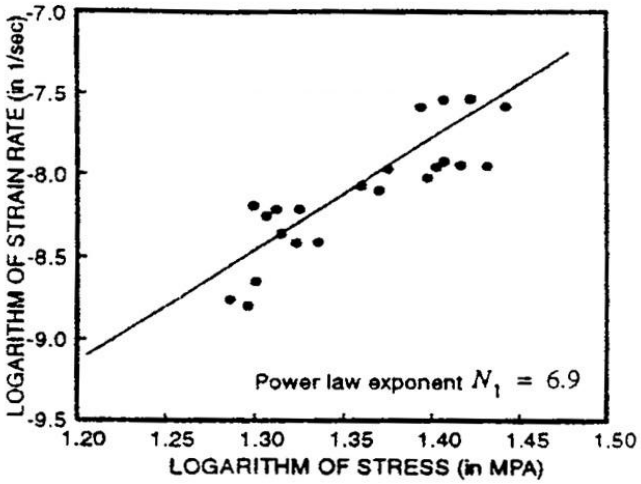

Figure 6. New Brunswick creep test results (Rothenburg, 1993)

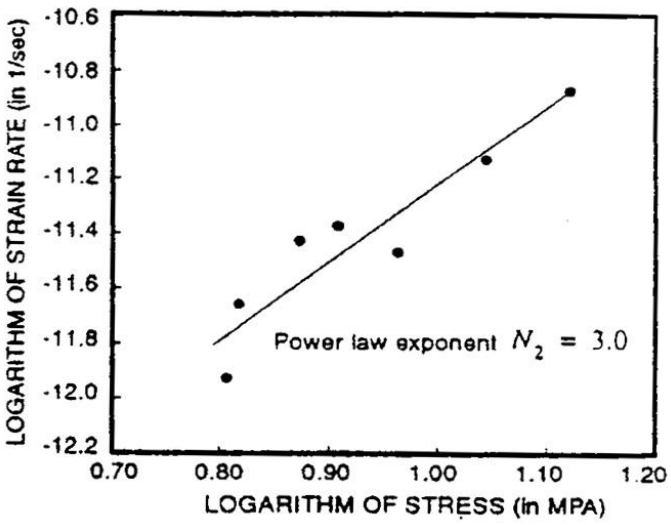

Figure 7. Rocanville potash creep test results (Lajtai and Duncan, 1998)

Figure 6 showed the results of creep tests under high shear stress for Sussex, New Brunswick potash; and Figure 7 showed the results of creep tests under low shear stress for Rocanville potash. Creep tests at high shear stresses determine N_1; and creep tests at low shear stresses determine N_2. From the data in Figure 6 and Figure 7, N_1 is 6.9 and N_2 is 3.0 for potash. The tested material may be from different locations, but it is very time consuming to perform a comprehensive set of creep tests for low and high shear stresses; therefore, a combination of test results from different areas may be used to predict the power law exponents.

3.3.2 Third Power Creep Law

Rothenburg et al. (2002) conducted a multi-parametric regression on the Palo Duro salt, and found that steady state creep for typical mining operations is dependent on the power law exponent to be three. The Rocanville potash and tachyhydrite at Taquari-Vassouras showed this for stresses of less than 10 MPa at room temperature. The third power creep law adopted for the tachyhydrite at Taquari-Vassouras included variables of pillar diameter and room width. One explanation for the power law exponent to be three is the differential stress is linearly proportional to the velocity of dislocations. Rothenburg et al. (2002) also concluded that the third power law corresponds to the unidentified mechanism in Munson's map. The

third power law is the single mechanism creep law with the exponent of three as shown below.

$$\dot{\varepsilon_{ss}} = \dot{\varepsilon}_0 \left(\frac{\sigma}{\sigma_0}\right)^3 \quad (9)$$

3.3.3 Transition Stress and Strain Rate of Creep Laws

The transition stress and strain rate is determined through laboratory experiments and observations in the field. The field conditions would be at steady state creep rates in virgin ground openings. The transition stress and the steady state convergence rates are linearly correlated on a logarithmic scale (Rothenburg, 1993). The experimental data from creep tests at a wide stress range exhibit two power law exponents. The strain rate at where the larger power law exponent starts is the strain rate used in the two mechanism creep law. Therefore, the strain rate of 3.24×10^{-11} sec^{-1} was determined from Figure 6 and Figure 7.

The parameters of the single and two mechanisms creep laws and the applicability of these laws were summarized in Chapter 3. The single mechanism law has been adopted due to its simplicity and ease of use. The two mechanism creep law includes two power law exponents, which is applied to involve two deformation mechanisms and for more sophisticated modeling methods. The single mechanism creep law was used in the modeling of the adopted salt pillar model for this project.

Chapter 4 Salt Mines

The room and pillar method is one of the most common methods in salt mining. Rotary cutters cut out material in long passes in two directions generally perpendicular to each other or at angles of 45° to 60°. The mined out material creates rooms, and the material remaining in the mine are the pillars. The rooms and pillars make up a mine panel, and a mine consists of numerous mine panels at incremental depths. The size of the rooms and pillars is determined by the limitations of mining equipment and design parameters.

The common observations made by Mraz (1973) from examining conventional potash mining in underground excavations is the closure rates or convergence rates undergo three stages for an isolated opening. The first stage is high closure rates decrease rapidly; the second stage is low closure rates decrease; and the final stage is constant closure rate. In addition, Mraz (1973) also concluded that some major components need to be considered when designing a stable room and pillar mine. These major components are: the overburden weight must be supported by pillars without excessive deformation; the roof span should not exceed the thickness of the overburden salt layer; there is enough clearance for the mining equipment at the entries of the mined rooms; and an appropriate extraction ratio. Salt strata situated in deep mines are in hydrostatic conditions due to high stresses compared to very low elastic limits of salts according to D. Mraz. The shape, size, age, and extraction ratio determines the stress fields and creep rates of a mined opening (Mraz, 1973). Many factors contribute to the stability of salt mine. The factor examined here is the time dependent behavior of salt.

This chapter presents the concept of the convergence of salt, the factors affecting the convergence of salt, and the general deformation pattern of salt. The behavior of salt mines is also presented in this chapter for better understanding of the failure mechanisms that are involved in salt mines. The collapse of the Saint-Maximilien mine panel from the Varangeville salt mine was used as an example to illustrate failure mechanisms in salt mines.

4.1 Convergence of Salt

Convergence in mining is the result of the rock material adjusting to the changes in in-situ stresses. Creep is a long term phenomenon that exhibits different rates during different time periods, and it is a parameter used to measure the stability of salt pillars. High convergence rates require less time for pillars to reach stability, but may also result in failure. The rate of convergence or creep rate is also dependent on the presence of impurities and defects within the salt rock material. Therefore, Munson's mechanism map is commonly used to understand the effect of micromechanics of salt rock behavior and to further predict creep rate. The term creep or convergence refers to the total displacement in the roof and the floor in this project. In other words, the measurement of creep and convergence is the amount of closure in the rooms of the mine.

From Hedley (1967), "In room and pillar mines the convergence of the roof and floor is made up of two components: the vertical deformation of the pillars because of the weight of the overlying strata; and the local sag or heave of the immediate strata." The factors that affect convergence measurements in salt and pillar mining include: time since mining, depth below surface, extraction ratio, pillar height, geological structure of salt, temperature, and humidity. These factors are explained in the following section summarized from Hedley (1967).

4.2 Factors Affecting the Convergence of Salt

Time

In order to compare convergence measurements between mines, convergence measurements need to be taken from the whole mine operating period starting right when the mine was initially excavated until the closure of the mine. This is difficult to achieve, and the constant rate of convergence is used instead.

Depth below Surface, Extraction Ratio, and Pillar Height

Calculating for the in-situ stress is not exact, so the average pillar stress is used in the formulations of laboratory experiments and computer models. The average pillar stress is calculated by the following function (Potts, 1976) which was later used in the code for modeling convergence rates.

$$\bar{\sigma} = \frac{\gamma D}{1 - r} \tag{10}$$

Where, γ is the unit weight of the overburden material, *D* is the depth below surface, *r* is the extraction ratio, and *γD* is actually the vertical stress.

According to Hedley (1967), the strain is constant as the pillar height changes. This causes the convergence to change proportionally to the pillar height. The pillar height does not affect the extraction ratio because the extraction ratio is only dependent on the area.

The extraction ratio is a function of the pillar width and the room width, and it is defined by the following:

$$extraction\ ratio = \frac{(W + W_R)^2 - W^2}{(W + W_R)^2} = \frac{excavated\ room\ area}{repository\ area} \tag{11}$$

Where, *W* is the pillar width of a square pillar and W_R is the room width. The extraction ratio is decided based on the depth of the mine and strength of the rock salt. Most room and pillar salt mines use an extraction ratio of approximately 0.55, which is generally the most accepted economical and stable value in practice. However, there have been extraction ratios ranging from 0.20 to 0.90 for some room and pillar salt mines. Low extraction ratios are usually due to pillars widths much larger than room widths which result in low convergence rates.

Geological Structure

The geological structure of the salt formation affects the creep properties within a given formation. Where weak geological strata are present, the convergence of room and pillars is no longer caused by the vertical deformation of the salt but by the deformation of the gaps in the weak strata. The presence of impurities in salt also causes the salt to behave more brittle and fail at a shorter time period compared to salt with fewer impurities.

Temperature and Humidity

In general, the rate of convergence increases with increasing temperature. An example of this trend is the findings from the Lyon Salt Mine in Kansas (McClain, 1966).

All of the aforementioned factors influence the convergence rate. The factors incorporated into the research are depth below surface, extraction ratio, and the pillar height.

4.3 The Deformation of Salt

Many experiments from researchers resulted in mathematical relationships only calculating the transient and steady state creep stages. The following graph is a time versus deformation curve for various salt specimens, where the tertiary creep was not reached for material failure. This graph indicates that the initial instantaneous strain can vary from sample to sample, but the general shape of the curve does not change.

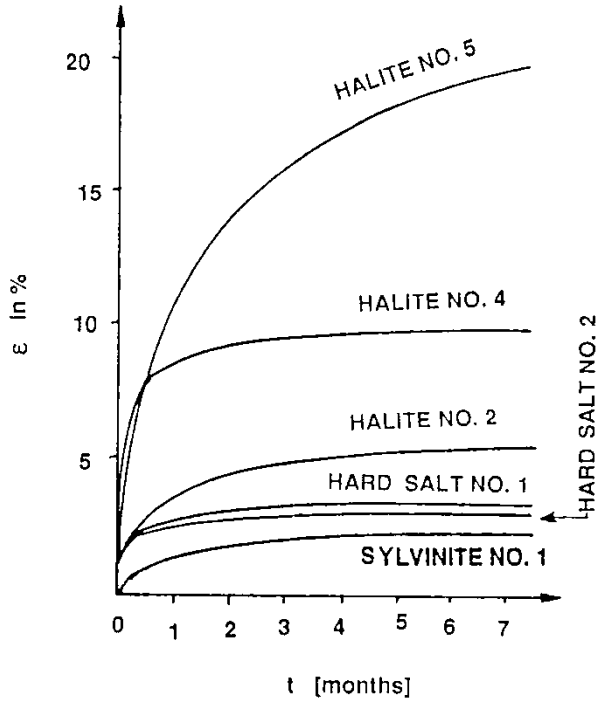

Figure 8. General deformation curve of salt specimens (Jeramic, 1994)

Some of the causes for the differences in the instantaneous elastic strain and the creep curve in Figure 8 are: the salt samples were tested at different temperatures, they were from different salt mines, or they contained various amounts of impurities or various types of evaporates in a single salt specimen. The temperature and the load applied to the salt specimen are constant in laboratory experiments. The deformation rate is high when shear stress is initially applied in the transient stage. The primary creep stage lasts a short period of time for a maximum of two months, but the duration of the secondary creep stage can last for a very long period of many years which can limit the duration of laboratory experiments. Salt specimens undergone laboratory tests exhibit the primary creep stage and steady state creep stage. In a series of triaxial tests, debonding occurs in the salt grains and fractures are created in the salt specimen. Shearing surfaces may start to develop, and bulging of the sample can occur (Dusseault, 2008). The behavior of salt specimens under a constant load in a laboratory is different from the behavior of rooms and salt pillars in a salt mine.

In a salt mine, the transient stage is not always recorded and only measurements from the steady state creep stage are recorded. Figure 9 is an example of convergence measurements in the potash mine in Brazil (Rothenburg, 2007).

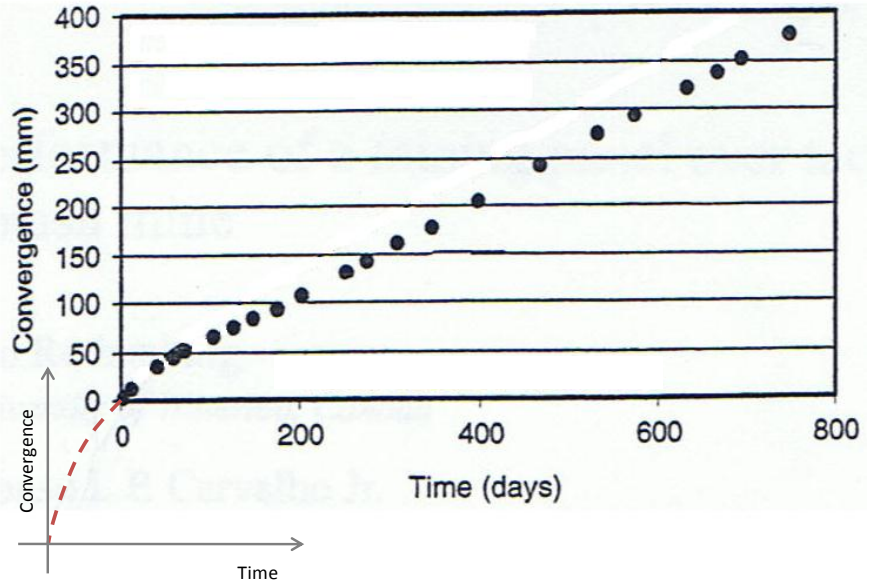

Figure 9. Deformation in a salt mine (Rothenburg, 2007)

As shown in Figure 9, there was a near linear relationship between the convergence measurements and the time which is typical of the steady state creep stage. If the graph was extended as shown by the red dotted line in Figure 9, the transient stage of the material can be extrapolated. This does not mean that the primary creep stage did not exist. When rooms and pillars were initially created in salt mines, there was not enough time for instrumentation to be installed in the mine to record the deformations in the primary creep stage. The overburden load is redistributed once a room is created. The load immediately above the rooms is shed and the abutments then carry the shed load. However, this is not the case with a salt specimen where abutments do not exist to allow for the redistribution of the overburden load. The applied load is carried solely by the salt specimen that results in specimen bulge, shear cracks, and/or debonding of the crystals within the specimen.

Many laboratory tests of salt specimens have been conducted to further examine salt behavior at specific mine locations. However, it is difficult to substitute the behavior

observed in the laboratory or measurements taken in the laboratory for in-situ behavior in the salt mine. These reasons were summarized from Mraz (1972): the specimen has been removed from the original loading condition and loaded again in the laboratory; the original confinement conditions have been removed, and the original confinement conditions are not easily reproduced; the relative crystal size of a specimen and a salt pillar is different; and the final reason is there may be temperature changes between the time of testing and the time of specimen extraction. Therefore, both laboratory experiments and in-situ measurements are required to further understand salt behavior in underground mining.

4.4 Changes in Stress with Time in Salt Mines

Since the overburden load is redistributed through time in a salt mine, stress changes also occur through time. Figure 10 is a schematic diagram of the stress distribution immediately after excavation, and a cross section of a mine panel was used to depict the stress distributions. The values in Figure 10 are for comparison purposes and not the exact values of a mine.

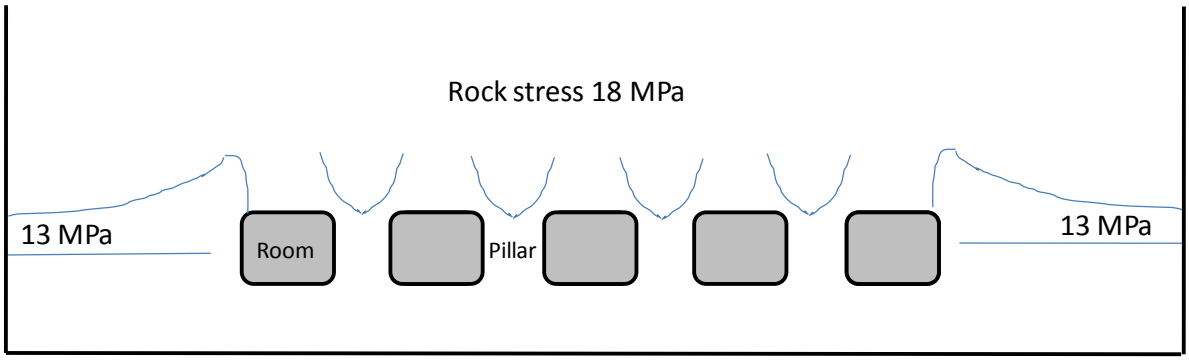

Figure 10. Stress changes immediately after excavation (Rothenburg, 2010)

In Figure 10, the grey areas are the excavated rooms; the white areas are the salt rock material; the white areas in between the rooms are the pillars; and the two large white areas on each side of mine panel are the abutments. The overburden load is the load due to the rock material immediately above the mine panel. Stresses are concentrated on the edges of the rooms, and there is less stress in the center of the pillar. There is minimal stress immediately

above the rooms since the load above the rooms has started to shed immediately right after excavation occurred. The stresses are high at the edges of the rooms, and the stress decreases into the abutments. For example, if the rock stress is 18 MPa for the overburden, the total stress in the abutments including the load shed from the excavated rooms remains less but close to the rock stress of the overburden.

Salt is a material that continuously deforms under applied load. Therefore, the stress distributions in the mine immediately after excavation are different from the stress distributions after a decade of mine operations. The following figure depicts the stress distribution in the mine after approximately 10 years since excavation has started.

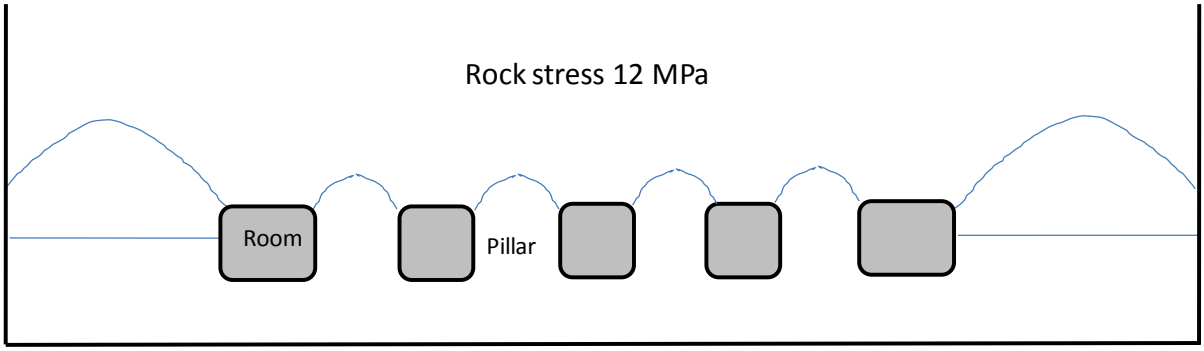

Figure 11. Stress distribution of a mine panel after 10 years (Rothenburg, 2010)

The stress distributions after 10 years of mine operations are almost the exact opposite of the stress distributions immediately after excavation. When the rooms were first excavated, the overburden load was carried by the pillars. However, there is only a certain amount of load that the pillars can carry until its' bearing capacities are exceeded and the pillars start to shorten. This results in higher stresses in the centers of the pillars. The shortening of the pillars also leads to roof sagging. The excess load carried by the pillars is then carried by the abutments, and the rock stress decreases in the overburden and increases in the abutments. The load that was originally carried at the edge of the abutments has been redistributed towards the center of the abutment.

If too much of the overburden was unloaded into the abutments, the rock stress of the overburden may decrease significantly. This results in shear stress developing at the edges of

the abutments and increasing the stress in the abutments, where the bearing capacity of the abutments can be exceeded. This is one of the main causes of sink holes at the surface of the salt mine. In many salt mines, an aquifer may exist above the mine. If the rock stress of the overburden decreases below the water pressure of the aquifer, cracking in the overburden material begins to occur. Water from the aquifer then seeps through the crack as it dissolves the salt material. As more salt material is dissolved in the overburden, more water is allowed to pass through into the mine and flooding occurs.

4.5 The Saint-Maximilien Panel in France

An example of mining failure due to large loads exerted on the pillars and abutments is the Saint-Maximilien mine panel from the Varangeville Mine in Lorraine, France. This mine panel failed in 1897, but it is still operational today. The two main causes for the failure of this mine panel are the large mining depths and a large extraction ratio of 0.82 that resulted in large loads, and the weak marl floor of the mine that was further weakened by water weathering it (Bérest, Brouard, Feuga, and Karimi-Jafaria, 2007).

Figure 12 is a schematic diagram of the Saint-Maximilien mine panel simplified from Bérest et al (2007). The room and pillar method was used, and the shape of the mine panel was considered to be a cylindrical cavern with a radius of 160 m. This mine panel was located at a depth of 160 m. The square pillars were 6 m in width and length, and the rooms were 5.5 m high and 8 m to 9 m wide. A 29 m×40 m pillar was left in the center of the panel to protect the access shaft. The mine panel was constructed in a 20 m thick salt layer, with a 25 m marl layer below the mine panel, and 60 m of roof salt that was divided by 0.5 m to 3 m of thin marl layers. The area outlined in red in Figure 12 is the area of the mine panel that failed, which was observed later from the ground surface to be a subsidence bowl. As shown in Figure 12, the excavated rooms are very long which are termed as galleries in this case.

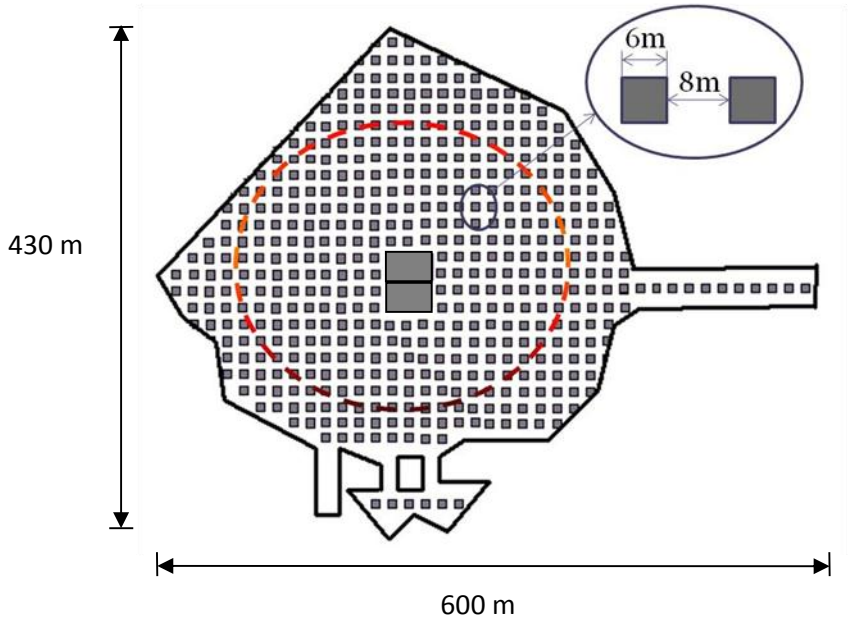

Figure 12. Saint-Maximilien mine panel (not to scale)

This mine panel was originally stable with eight rooms. However, this mine panel failed after the ninth room was created 15 years after the first room was excavated. If the horizontal dimension of the mine panel is small enough, the roof of the panel is stiff enough to prevent deformation in the pillars. Excavating the ninth room created more load for the overburden to carry which led to the pillars carrying more load. The pillars then started to deform and sink into the marl floor. Marl is a very soft material with a very low cohesion of 2 MPa, and it is sensitive to brine and water weathering (Bérest et al, 2007). There were small fissures in the marl floor, and the water that was used to cut to the pillars seeped into the fissures and further weakened the marl floor. The bearing capacity of the pillar and the floor was slowly exceeded and caused the pillars to sink more into the marl floors. As the pillars continued to push into the marl, floor heave started to occur as marl was displaced into the galleries. In some locations of the mine panel, the roof collapsed due to the continuous pillar punching. As the pillars deformed, the roof above the pillars started to bend and slabs of the roof fell into the rooms. This was the consequence of the roof adjusting to the horizontal stresses in the overburden, and resulted in the debonding of marl layers. Most of the overburden load was transferred to the abutments as the bearing capacities of the salt pillars were exceeded. Shear stresses then developed at the edge of the panel that damaged the salt material in the

overburden and decreased the roof stiffness significantly. An increased roof span and very soft floor material caused the failure of this mine panel.

The deformational behavior of salt and the factors affecting the deformation were explored in this chapter. The primary and secondary creep stages are exhibited in laboratory experiments and in salt mines. However, the behavior and results obtained from a salt specimen may not be representative of the behavior and results in the mine. This is due to different loading and confinement conditions between a salt specimen and in-situ material. The overburden load is a major factor in the stability of mines because it is not only carried by the pillars, but also the abutments. The Saint-Maximilien mine panel at the Varangeville Mine in France was used as an example for the causes of failure which were large extraction ratios and large mining depths.

Chapter 5 Literature Review on Salt

The mining of salt and evaporites have a long history. There is extensive research in material properties, mineral processing, material extraction, and the design of the mine. Laboratory experiments and in-situ measurements of deformation have been completed in many salt mines throughout the world. Many equations have been developed to predict the in-situ stress of salt pillars, and numerical modeling has been performed to help understand the behavior of salt mines.

Selected research on the design of salt pillars and salt behavior is presented in this chapter. Examples of the numerical modeling of salt behavior, laboratory results of compressive strength tests of salt specimens, and the comparison between laboratory results and in-situ measurements are included in this chapter.

5.1 Numerical Modeling of Salt Behavior

The appropriate size of a salt pillar to support the overburden load is very challenging to determine. Numerical modeling is not always easily accessible, and simple equations may allow for quick assessment of mine conditions. Van Sambeek (1997) used the finite element method to determine the pillar strain rates and room closure rates or deformation rates for various pillar width to pillar height ratios. The purpose was to validate the pillar design equations by comparing the results of the equations with modeling results. The pillar height and extraction ratio was kept constant. Pillar width to pillar height ratios of one to five were used in the modeling.

Van Sambeek (1997) proposed the average horizontal stress and the average vertical stress are related by 10 percent of the pillar with to pillar height ratio. When determining equations to predict the average effective stress, it was found that as the pillar width to pillar height ratio becomes large, the effective stress approaches zero rapidly. Also, plane strain conditions are approached when pillars are long in one dimension. When using the equations developed by Van Sambeek for determining pillar creep rates, it was found that the pillar

compression rate for rectangular pillars is 50 percent less than a square pillar with the same width, pillar height, and extraction ratio.

A study was performed to determine the influence of tachyhydrite on a mine panel in the Taquari-Vassouras potash mine. Tachyhydrite creeps two magnitudes faster than the surrounding potash, and it is highly hygroscopic. Sections of this mine have been successfully mined, but instrumentation has been installed to monitor the convergence of the openings. There was an interested lower sylvinite bed overlying a tachyhydrite layer that is 0 m to 20 m.

A circular and a square salt pillar were modeled with an extraction ratio of 0.50 using VISCOT, VELMINA, and FLAC3D for the Taquari-Vassouras potash mine (Rothenburg et al., 2007). The modeling results was the convergence rate of 0.12 m/yr, and the compression rate of all salt layers above the mine panel of 0.10 m/yr. A relationship was also found to determine the steady-state rate of penetration of a pillar into tachyhydrite. The variables used to determine the steady state rate was the tachyhydrite thickness, pillar diameter, room width, and average stress. In addition, analytical approximations were also first determined through pillar dimensions. The developed relationship was based on the single mechanism law with the power law exponent of three.

A series of plane strain axisymmetric runs were completed using VISCOT. The data showed that increasing tachyhydrite thickness increased the convergence of the rooms adjacent to the central pillar. The result of the modeling was the soft tachyhydrite material underlying the mine panel caused pillar punching and large amounts of floor heave. The amount of floor heave was the largest adjacent to the abutments. This was due to the abutments carrying more load than the pillars, which allowed the tachyhydrite to squeeze from under the abutment into the rooms.

5.2 Laboratory Experiments on Salt

A laboratory experiment was completed by Potts (1964) to examine the physical behavior of rock salt under rapid loading conditions and long periods of time. The salt specimens were from the Meadowbank Mine at Winsford, Chesire. The area of concern was the rooms and pillars underlying a 60 feet rock salt bed with a working height of 20 feet. The major factors affecting the compressive strength that were of concerned for the laboratory experiment were specimen size, width to height ratio, time dependent behavior, and the shape of the specimen.

Cube specimens with lengths of one inch to 14 inches were tested at a fixed loading rate of 1ton/in^2. This was to determine the effect of specimen size. It was found that the compressive strength did not decrease with increasing specimen volume. Width to height ratios of one to four with specimen length of two inches and four inches were tested. It was found that the specimen strength increased with increasing pillar width to pillar height ratio. When testing for the influence of the specimen shape, it was found that circular specimens resulted in higher compressive strengths compared to the square and rectangular specimens. Therefore, it was concluded that the perimeter to area ratio was a factor influencing the strength of the specimens. Different specimen shapes of the same height and surface area were then tested. The last set of tests indicated that the strength of the specimen decreases with increasing perimeter when the width to height ratio, surface area, and specimen height were the same for all specimens.

When testing for the creep effect, the specimens were reloaded at 30 minute intervals. It was found that the strain rate decreases suddenly at low stresses, but the maximum strain was not defined due to the short duration of the tests. A four inch square with 3.6 inch height was then tested at a constant load of 4000 psi, and it failed after 48 hours. The tertiary creep stage or the accelerated creep stage was observed before material failure. The creep rate approaching failure was 10 times the creep rate during the transient stage.

The conclusion for Potts' experiment on creep influence was the strain rate increases rapidly when approaching failure at high stresses. This is contradictory to the creep model where the

creep rate should be approaching zero. The following relationship was then proposed, where the stress is a function of strain, strain rate, and the loading stress rate. The maximum strain can then be estimated from the initial stress as a function of strain. A graph of stress versus maximum strain can then be plotted for different stress increments, and result in a limiting stress from the asymptotic value. This finding may allow for prediction of material failure, but this finding was based on salt specimens which do not always represent the in-situ conditions of the mine.

As mentioned before, laboratory test results alone are not sufficient in predicting salt pillar and excavated rooms behavior. In many studies, laboratory tests and in-situ measurements are taken simultaneously. Potts (1964) also took in-situ measurements of the pillars using borehole extensometers. The pillars were still undergoing development when measurements were taken. The major observations and conclusions made were the pillars were expanding laterally during mine operations due to load transfers; the expansions occurred at the edges of the pillar; the peak strain rate occurs at approximately 10 ft inside the pillar and not on the edge of the pillar; the largest displacement occurred at the edge of the pillar, but the largest displacement started to more towards the center of the pillar as time increased; and the creep rate reduced quickly when mining operations ceased.

5.3 In-situ Creep Measurements

Munson (1997) presented a process for predicting the creep closure of rooms in salt excavations. The Waste Isolation Pilot Plant (WIPP) was used for the disposal of Transuranic radioactive waste generated by U.S. defense programs. The WIPP is located in the deep bedded salt deposits of southeastern New Mexico. The facility is situated 655 m below the ground surface in a laterally extensive bedded salt deposit that is 600 m thick. The two major types of salt at this location are clean salt, and the argillaceous salt that contains up 5 % of clay. The salt layers contain thin, approximately 100 mm layers of clay and anhydrite. Due to the disposal of sensitive material, it was very important to be able to predict the closure rates of rooms. Also, salt creeps until the complete closure of the repository rooms and

encapsulating the radioactive waste, which would provide permanent coverage of the radioactive waste.

Parameter values of the constitutive model of salt were determined from compressive triaxial tests. The constitutive model for steady state creep used was based on Munson's mechanism map. The proposed model was workhardening and recovery transient creep governed by first order different equation with higher order kinetic functions. The Tresca criterion was chosen for the dislocation mechanism. Salt specimens were taken from around the underground openings. The selected constitutive model and its parameters were validated using the finite element method. The modeled results were then compared to in-situ measurements. The in-situ measurements were taken in excavated rooms that are 5.5 m wide by 5.5 m high by 93 m long. The comparison results were the vertical deformation and horizontal deformation were within 2% and 10%, respectively of the measured values for unheated rooms. It was found that the horizontal deformation was less than the vertical deformation due to different responses of the layers. It was also found that the radioactive waste increased the temperature of the rooms and thermal influences had to be considered. The argillaceous salt layers in the roof and floor are less resistant to creep compared to the more resistant to creep clean salt layers in the walls of the room. Comparisons were made between laboratory measurements and in-situ measurements for heated and unheated rooms.

Previous research was presented in this chapter. Results obtained from numerical modeling, laboratory tests, and in-situ measurements are all important. The stratigraphy of the salt mine is also a large factor that affects the salt behavior. Some of the research projects presented in this chapter were able to compare the laboratory results with modeling results, and modeling results with in-situ measurements. The purpose of the research presented in this chapter was to find methods to allow for the prediction of salt deformation due to its time dependent behavior.

Chapter 6 Methodology

The methodology used for this project was using RECTPIL and FLAC3D to perform three dimensional analysis of a salt pillar model. RECTPIL is a mesh generator and FLAC3D is a three dimensional finite difference software. A salt pillar model was created from RECTPIL in order for FLAC3D to model the behavior of a salt pillar at the depth of 500 m. The salt pillar model was composed of layers of roof salt, floor salt, a salt pillar, elastic material above the roof salt, and elastic material below the floor salt. The material properties used in the modeling were based on literature reviews. The initial stages of modeling determined 20 years was the time period that the adopted salt pillar reached mechanical stabilization in FLAC3D. Simulations were performed on the adopted salt pillar model to determine the mesh sensitivity of the software. After the appropriate mesh size was chosen, more than 100 simulations were completed using various pillar width to pillar height ratios with different pillar dimensions.

The adopted salt pillar model and the methods used to test for mesh sensitivity are presented in this chapter. Background information on both software used for this project and the method of analyses are also included in this chapter.

6.1 The Adopted Salt Pillar Model

One standard salt pillar model was adopted for the numerous simulations in this project. The adopted salt pillar model consisted of five major material layers, which is shown in Figure 13. The model was made up of a mesh of many rectangular elements, where the ratio for the number of elements to the material thickness was 1:2. However, this ratio did not apply to the pillar where 20 elements were used for the pillar height regardless of the height of the pillar.

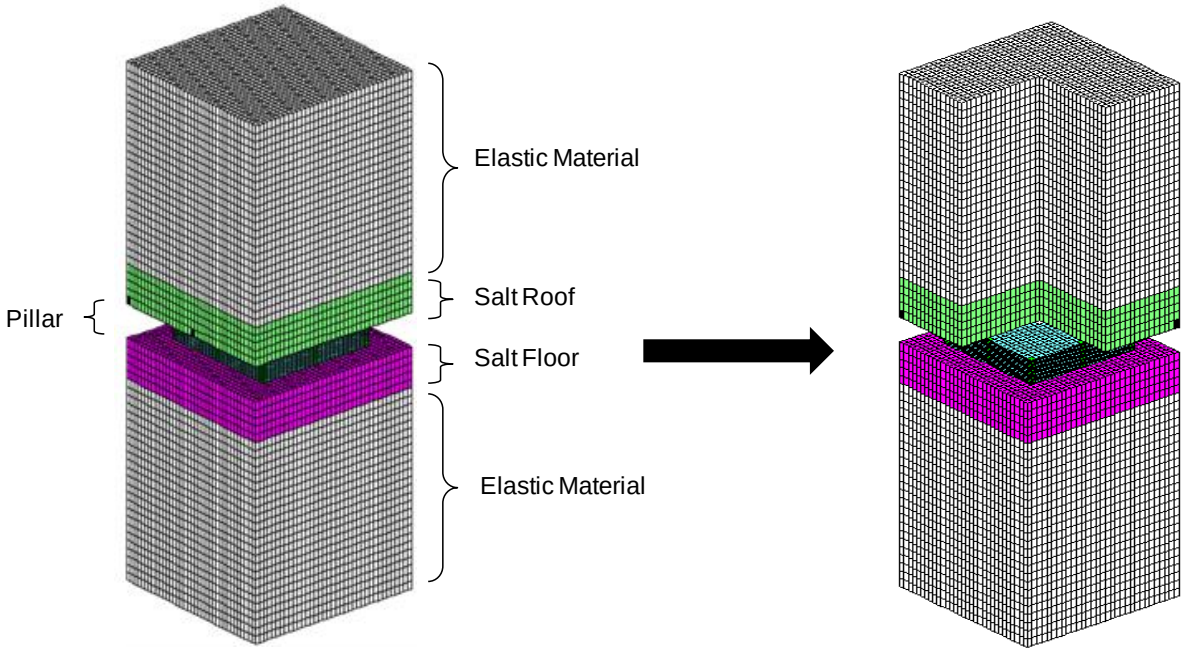

Figure 13. Adopted salt pillar model

The pillar model in Figure 13 was generated using RECTPIL and FLAC3D. The pink and green layers are the salt material, the white layers are the elastic material, and the blue is the pillar which is made up of the same salt material as the pink and green layers. The salt layers are the salt roof and salt floor. A cutout of the salt pillar is shown in Figure 13 to indicate the location of the salt pillar. In many salt mines, not only heterogeneous materials are situated above the interested salt layer, but also an indefinite layer of heterogeneous materials lie beneath the interested salt layer. Therefore, a 50 m elastic layer of homogeneous material was added above and below the salt layers in all of the models to replicate the heterogeneous materials. Each side of the model is exactly the same because only squared pillars were used in the modeling. Table 1 summarizes the material properties for each layer and the values used in all models.

Table 1. Material Properties of the Adopted Salt Pillar Model

Type of Material	Unit Weight (MN/m^3)	Young's Modulus (MPa)	Poisson's Ratio	Reference Stress (MPa)	Strain Rate	N_1 Exponent	N_2 Exponent
Elastic Roof	0.023	20000	0.33	10	0.000	1.0	1.0
Salt Roof	0.023	20000	0.33	10	0.002	3.0	3.0
Pillar	0.023	20000	0.33	10	0.002	3.0	3.0
Floor Salt	0.023	20000	0.33	10	0.002	3.0	3.0
Elastic Floor	0.023	20000	0.33	10	0.000	1.0	1.0

The unit weight, Young's modulus, and Poisson's ratio were determined after Hansen (1984); and the transition stress, strain rate, and power law exponents were taken from Rothenburg et al. (1993). The single mechanism creep law was used for the salt pillar models; therefore, both power law exponents were assigned the same value for the salt layers.

Modeling in FLAC3D not only requires material properties, but also boundary conditions for the system. The purpose of the adopted salt pillar model was to simulate salt behavior at the depth of 500 m. Roller boundaries were required on all sides of the salt pillar model to represent in-situ conditions. Figure 14 shows the boundary conditions that were used for the adopted salt pillar model.

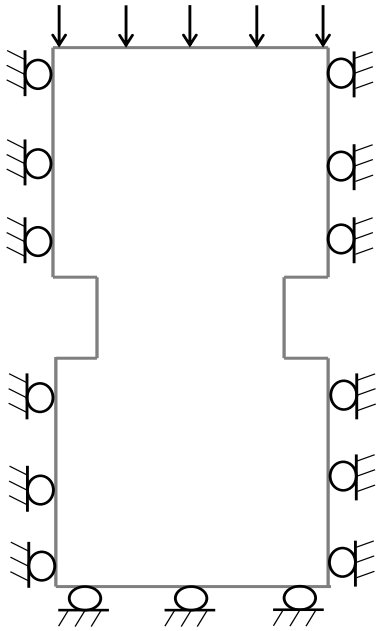

Figure 14. Boundary conditions of the adopted salt pillar model

Figure 14 is a cross section of the adopted salt pillar model. The material properties, dimensions, and boundary conditions of the adopted salt pillar model are symmetric on all sides. The roller boundaries confine the force that is exerted from the surrounding underground material, and there is the overburden load that exerts onto the salt pillar model from above.

Four pillar width to pillar height ratios were used to evaluate the change in convergence rates of the pillar among different pillar width to pillar height ratios. Four pillar width to pillar height ratios from one to five was thought to be sufficient. The laboratory experiments and modeling found in the literature review used pillar width to pillar height ratios of one to five (Potts, 1964 and Van Sambeek, 1997), Each pillar width to pillar height ratio used three sets of pillar dimensions for a constant extraction ratio of 0.54. Each set of pillar dimension consisted of eight scenarios, where the salt thicknesses immediately above and below the pillar varied from 0 m to 26 m for each scenario. Salt thickness in this project refers to the thickness of the roof salt and floor salt, which was shown in Figure 13. The thickness of the roof salt and the floor salt were varied for the same amount in the salt pillar models. For example, if the thickness of the roof salt was 10 m then the floor salt was also 10 m in the modeling of the salt pillars.

The dimensions of the modeled pillars were determined by the number of passes of a continuous mining machine. Each pass of a continuous mining machine can create a four meter wide and three meter tall room. Once the room width was determined, the pillar width was then calculated based on a low extraction ratio of 0.54. Pillar heights were then chosen to result in a broad range of pillar width to pillar height ratios for this project and for the simplicity of the model. Figure 15 shows the various dimensions used in the adopted model.

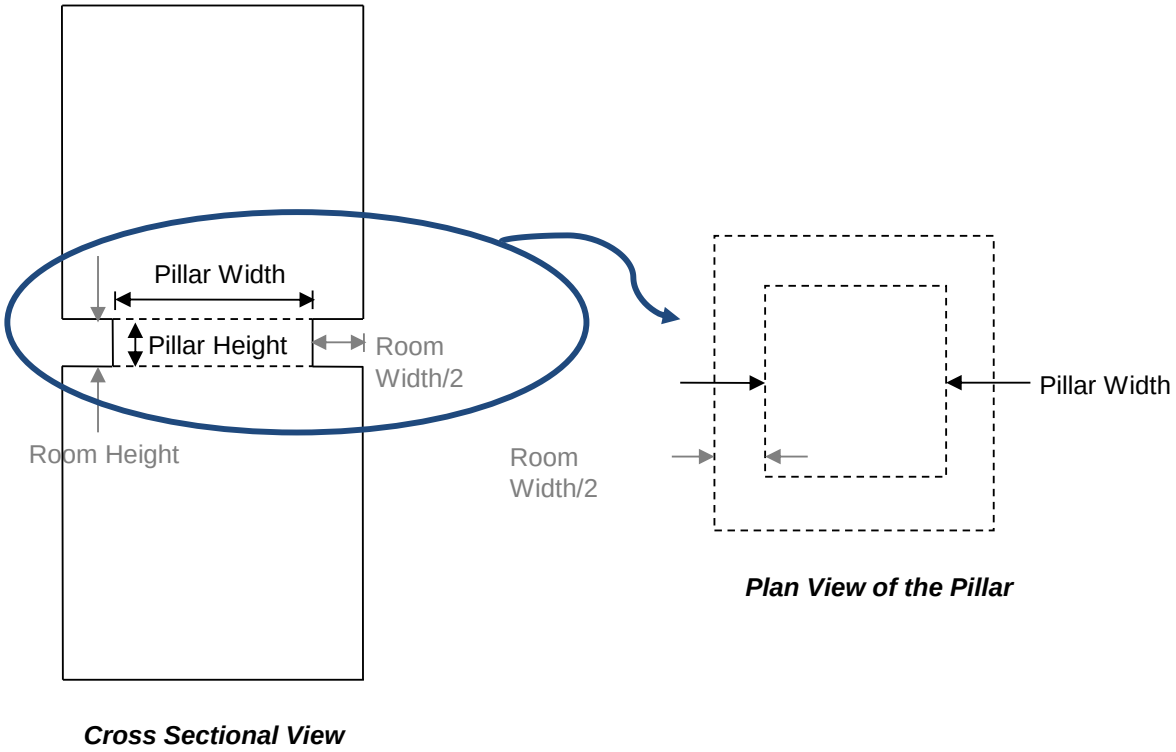

Figure 15. Dimensions of the adopted salt pillar model

The diagram on the left in Figure 15 is the cross section of the salt pillar model; and the diagram on the right in Figure 15 is the plan view of the pillar. Only half a room is shown because only one salt pillar was modeled. The room is the space created from the extracted material between adjacent salt pillars; therefore, the room width is the length between the sides of adjacent pillars after a room has been mined out.

To determine whether the room widths had an effect on the results in addition to the pillar widths, three different room widths were used for each salt thickness of each pillar width to pillar height ratio while maintaining the same extraction ratio. The extraction ratio is the function of the pillar width and the room width. Therefore, the room width changed proportionally to the pillar width, which allowed the pillar width to pillar height ratio and the room width to room height ratio to remain constant. This resulted in three sets of pillar and room dimensions for each pillar width to pillar height ratio. The pillar width to pillar height ratios used for this project were 1.5, 2.3, 3.8 and 4.6. Table 2 is a summary of the dimensions of the adopted model used for each pillar width to pillar height ratio.

Table 2. Model Dimensions

W/H	**Pillar Width (m)**	**Room Width (m)**	**Pillar Height (m)**	**W_R/H**
1.5	23.10	11.00	15.00	0.73
1.5	31.50	15.00	21.00	0.71
1.5	39.75	19.08	26.05	0.73
2.3	23.10	11.00	10.00	1.10
2.3	31.50	15.00	13.70	1.10
2.3	39.75	19.08	17.35	1.10
3.8	23.10	11.00	6.08	1.81
3.8	31.50	15.00	8.29	1.81
3.8	39.75	19.08	10.46	1.82
4.6	23.10	11.00	5.00	2.19
4.6	31.50	15.00	6.85	2.19
4.6	39.75	19.08	8.67	2.20

Where, W/H is the pillar width to pillar height ratio, and W_R/H is the room width to pillar height ratio. The room width to pillar height ratios and the pillar width to pillar height ratios were the same to the magnitude of one tenth. This inconsistency did not affect the trends found in the results.

The horizontal element sizes and the number of elements used to create the mesh for the adopted salt pillar differed for each room width. The vertical element size was constant at 2 m. The following table summarizes the number and horizontal size of the elements used for each set of room widths.

Table 3. Mesh Configuration for Salt Pillar Model

Element Size (m)	Pillar Width Elements	Pillar width (m)	Room Width Elements	Room Width (m)
1.10	21	23.10	10	11.00
1.50	21	31.50	10	15.00
1.59	25	39.75	12	19.08

The element sizes were initially calculated by the mesh generator RECTPIL, and they were adjusted to keep the extraction ratio constant as the pillar and room widths increased. Calibrations were performed to determine the appropriate mesh size for the adopted salt pillar model, and the calibration process is explained in Chapter 6.1.1. More than 100 simulations were performed for this project, and each model was simulated for a 20 year period. Before the adopted salt pillar model was completed, trial runs were performed to check that the computer code and the calculations were accurate in FLAC3D. In the trial runs, 20 years was the time period that the model would stabilize, where the system reached mechanical equilibrium. Each scenario for a specific pillar width to pillar height ratio took approximately 6 to 8 hours to complete.

6.1.1 Mesh Sensitivity

Various mesh sizes were used to determine the mesh sensitivity of the software. Two sets of calibrations were completed. The first set of calibrations varied the vertical element size of the pillar while keeping the mesh size of the elastic material constant. The second set of calibrations varied the horizontal cell size of all material layers and the pillar, and the vertical element size was changed for the pillar. The material properties used for the calibrations were the same as the values presented in Table 1, and the calibrations were modeled for 20 years. Salt layers above and below the pillar were not included during calibration. This setup eliminated any influence of salt material behavior above and below the pillar, and the only varying factor would be the behavior of the salt pillar due to different mesh sizes.

In the first set of calibrations, the horizontal element size was 1.10 m for all material layers and the pillar, and the vertical element size was 2 m for the elastic material above and below the pillar. The ratio for the number of elements to the material thickness remained at 1:2 for all calibrations. The mesh of a 5 m salt pillar was varied since the height of the salt pillar changed in the various modeled scenarios. The mesh of the salt pillar varied vertically in increments of five elements from five elements to twenty five elements, but the horizontal element size remained as 1.10 m with 21 elements in the horizontal direction. A total of five calibrations for the vertical mesh of the salt pillar were completed.

The vertical stress and the convergence rate were the parameters compared for the tested mesh sizes. For comparison purposes, the results of each vertical increment were compared to a pillar with five elements. The vertical stress values were taken horizontally across the center of the pillar as shown in Figure 32; and the convergence rate values were taken in the middle of the room as shown in Figure 20. Detailed descriptions of the locations where the results were obtained are described in Chapter 7.1 and Chapter 7.3. The vertical stress results were taken along a horizontal profile with numerous values, and the values were very similar for all mesh sizes. Therefore, the largest percentage difference in absolute values along the horizontal profile for each increment was presented. Table 4 is a summary of the percentage error of each vertical increment of five compared to a pillar with five elements for vertical stress.

Table 4. Absolute percentage difference of vertical stress for pillar calibration

Number of Elements	Absolute Percentage Difference (%)
10	3.08
15	0.00
20	3.83
25	4.35

There was no difference in the vertical stress values between five vertical elements compared to 15 vertical elements in the pillar. There was the most percentage difference of 4.35% in the vertical stress between 25 vertical elements and five vertical elements. The maximum

vertical stress always occurs in the middle of the pillar, and this is typical pillar behavior that is explained more in detail in Chapter 7.3. Table 5 presents the convergence rates and maximum vertical stress for all vertical increments of the pillar. The convergence rates in the middle of the room at the center of the pillar was found to be the same as the convergence rates at the corners of the salt pillar model. Figure 20 is a diagram describing where the convergence rates were taken.

Table 5. Convergence rates for pillar calibration

Number of Elements	**Convergence Rate (yr^{-1})**	**Vertical Stress (MPa)**
5	9.93×10^{-3}	50.91
10	1.10×10^{-2}	50.02
15	9.93×10^{-3}	50.91
20	1.14×10^{-2}	50.08
25	1.15×10^{-2}	50.13

For the various mesh sizes of the pillar, there was an average of 50.41 MPa with a standard deviation of 0.5 MPa for the maximum vertical stress. According to Table 5, there is very little variation in the convergence rates among all mesh sizes. The maximum difference between the largest and lowest convergence rate value was 1.52×10^{-3}. Different mesh sizes in the pillar resulted in some differences in the results.

In the second set of calibrations, the horizontal cell size was varied for the adopted salt pillar model to determine if the mesh size of the material above and below the pillar affected the data. The ratio for the number of elements to the material thickness was 1:2, where the vertical cell size remained constant at 2 m. Horizontal cell sizes of 1.10 m, 0.69 m, and 0.55 m were used to test the mesh sensitivity. The number of vertical elements for a 5 m pillar was also varied, but the number of horizontal elements for the pillar remained at 21 elements. Table 6 is a summary of the mesh size and convergence rate results for the second set of calibrations. The convergence rates in the middle of the room at the center of the pillar was found to be the same as the convergence rates at the corners of the salt pillar model.

Table 6. Mesh size for the second set of calibrations

Horizontal Cell Size	Number of Vertical Elements for a 5 m Pillar	Convergence Rate (yr^{-1})	Maximum Vertical Stress (MPa)
1.10	20	1.14×10^{-2}	50.08
0.69	30	1.26×10^{-2}	50.40
0.55	40	1.18×10^{-2}	49.86

According to Table 6, the convergence rate values do not seem to be affected by the mesh size. The horizontal cell sizes of 1.10 m and 0.55 m resulted in similar convergence rates of 1.14×10^{-2} yr^{-1} and 1.18×10^{-2} yr^{-1}, respectively. These convergence rates are less than the convergence rate of 1.26×10^{-2} yr^{-1} from the horizontal cell size of 0.69 m. The average maximum vertical stress from the second set of calibrations was 50.11 MPa with a standard deviation of 0.28 MPa. There is little difference in the results from varying the mesh size in the second set of calibrations.

From both sets of calibrations, different mesh sizes in the pillar and in the elastic material above and below the pillar resulted in different data values. However, both sets of calibrations had similar maximum vertical stress and convergence rate values. There was no relationship between the mesh size and the results. A finer or coarser mesh did not allow for the results to converge closer to a specific value.

6.2 Method of Analyses

The salt pillar model was made by using RECTPIL. RECTPIL is a mesh generating program that generates a two dimensional mesh from the inputs of pillar and room dimensions and then creates an output file which is used as an input file for FLAC3D. FLAC3D uses the FISH language for command inputs, and two files of calculations written in the FISH code were created. The salt pillar model was used for all scenarios where only the dimensions of the pillars and rooms were changed for each run of the model, but the shape and the material properties of the pillar remained constant. Chapter 6.2 provides background information on

the software used, and the verifications used in FLAC3D to validate the computer code and methods used.

6.2.1 RECTPIL Program

The RECTPIL program was written in QB4 by Professor Leo Rothenburg. The two dimensional mesh generator only displays the plan view of a pillar. The user can determine the number of elements, shape of the pillar, and the dimensions of the rooms and pillars etc. RECTPIL uses the above inputs to create a mesh of square elements and calculate the size of the elements, but the created mesh may not have the exact dimensions specified by the user. This is because the element sizes are only calculated to the accuracy of one hundredth of a meter using square shaped elements. An example of the output from the RECTPIL program is presented in Figure 16.

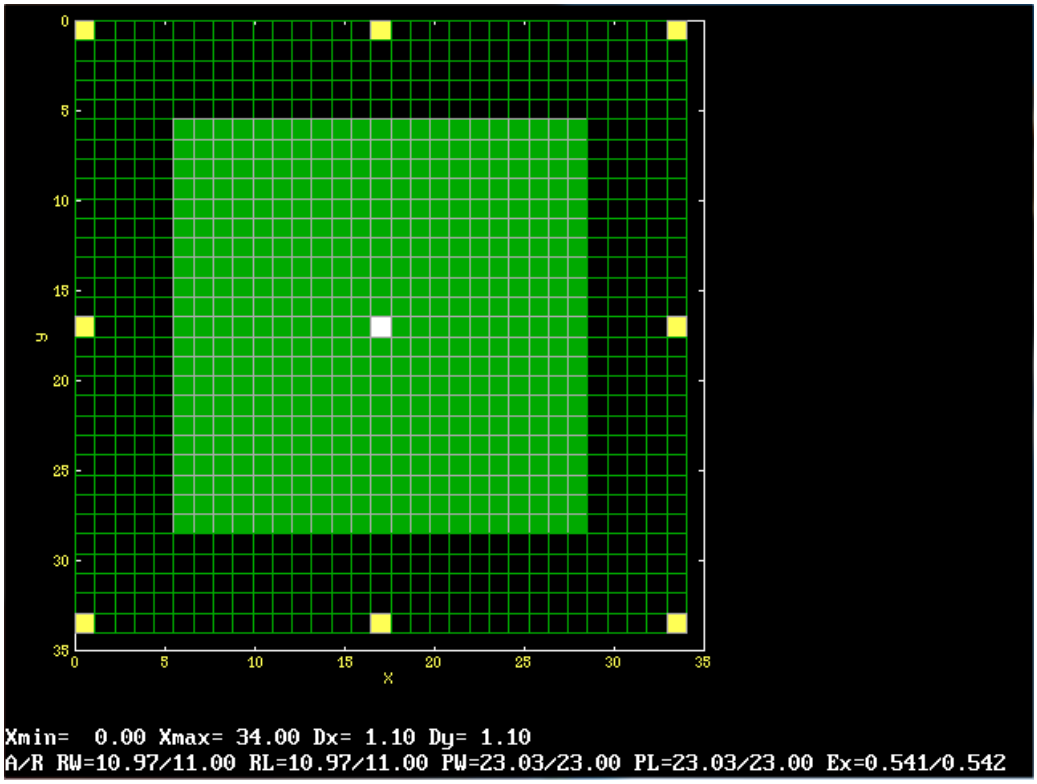

Figure 16. RECTPIL Output Screen

The text output at the bottom of Figure 16 shows the dimensions of the pillar. Dx and Dy are the element lengths in the direction of the x-axis and y-axis, respectively. In the short form A/R, A is the actual length, and R is the length input by the user; RW is the room width, RL is the room length, PW is the pillar width, PL is the pillar width, and Ex is the extraction ratio. The values presented in the RECTPIL program are accurate to the one hundredth value. The most accurate calculation of the pillar length and room length is by the number of squares and the element.

6.2.2 FLAC3D

The three dimensional version of the Fast Lagrangian Analysis of Continua (FLAC) was used for the three dimensional analysis to model the adopted salt pillar. FLAC3D is a finite difference software used for mechanics computations. FLAC3D calculates the mechanical behavior of a continuous three dimensional medium as the system reaches equilibrium or steady state plastic flow. FLAC3D adopts the explicit formulation where a time step is used for computations. This software is applicable to a wide range of geotechnical problems. Some examples are seismic excitation of structures in earth dam design, the influence of fault structures in mine design, and the evaluation of mechanical loading in foundations.

In FLAC3D, materials are represented by polyhedral elements on a three dimensional grid with x, y, and z coordinates. The material can yield and flow and the grid can deform in large strain modes with the material. Linear or non-linear stress/strain laws can be applied to each element in response to applied forces and boundary conditions. FLAC3D uses the explicit and Lagrangian calculation scheme and mixed-discretization zoning technique that allows for accurate modeling of plastic collapse and flow (Itasca Consulting Group, Inc., 1997).

There are similarities and differences in finite element and finite difference methods, and they are summarized here from the user's manual of the software (Itasca Consulting Group, Inc., 1997). The similarity is both methods solve differential equations using matrix solutions, which relates forces to displacements at each node. The first difference is FLAC3D uses a mixed discretization scheme as opposed to the reduced integration scheme for the

modeling of plastic flow and plastic collapse loads; The second difference is full dynamic equations of motions are used even for systems that are essentially static, which allows for computations of physically unstable systems without numerical complications; And the third difference is explicit solutions are used in FLAC3D as opposed to implicit solutions, which allows for much shorter time periods of modeling. The explicit solution takes the same time to solve for nonlinear problems of stress or strain as an implicit solution does for linear problems.

6.2.3 Verification of FLAC3D Results

There were certain parameters that were calculated during the modeling of a system in FLAC3D. These parameters were verified at key locations throughout the adopted salt pillar model. The parameters that were verified were vertical stresses, time, and the unbalance force ratio. The unbalanced force is the ratio between the total resisting and total loading force of a system. As the unbalanced force approaches zero, the system reaches mechanical equilibrium. If the unbalanced force approaches a non-zero value, the system has not reached mechanical equilibrium and the system is approaching failure. In this case, the system is the adopted salt pillar model. An example of the history of the unbalanced force ratio is shown in Figure 17.

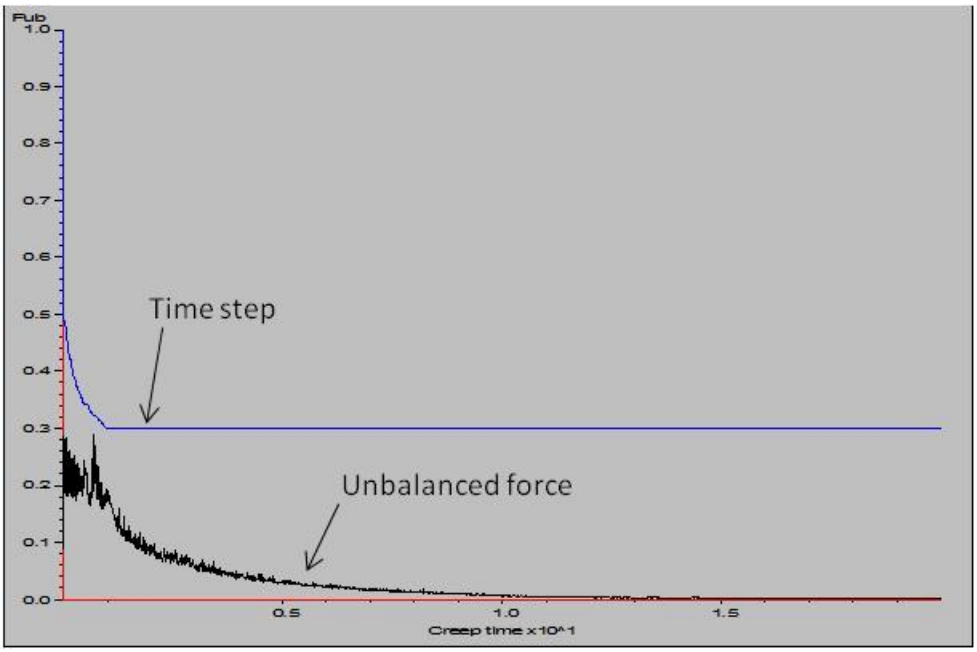

Figure 17. Unbalanced force ratio and time step

The above figure indicated that the ratio between the resisting force and loading force was very high for the first five years. The unbalanced force ratio declined exponentially and the ratio approached zero after 10 years. An unbalanced force ratio of nearly zero after 10 years indicates that the adopted salt pillar model has reached mechanical equilibrium after 10 years. FLAC3D uses explicit code, where computational steps are taken to perform calculations. As the system is approaching mechanical equilibrium, the time step is increased since less number of time steps are required to complete the computations. In Figure 17, the time step actually decreased exponentially through time as the system approached mechanical equilibrium. This is due to the time step displayed in Figure 17 are the negative logarithmic value of the actual time step used.

Vertical stresses were also observed to determine if FLAC3D were performing calculations correctly. Figure 18 is an example of how the vertical stress changes through time.

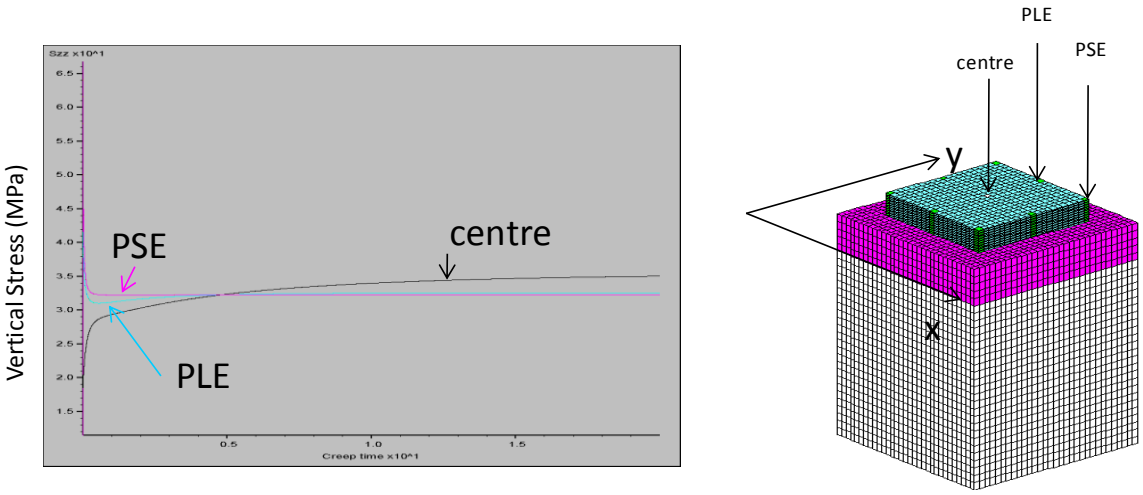

Figure 18. Vertical stresses calculated in FLAC3D

The captions in Figure 18 are the locations of where the vertical stresses were observed. In the diagram on the right of Figure 18, the adopted salt pillar model was split in half to show the detailed locations of where the vertical stresses were observed. The vertical stresses decreased exponentially for the edge (PLE) and the corner (PSE) of the pillar until approaching a near constant value; and the vertical stresses increased exponentially for the center of the pillar until approaching a near constant value. This behavior is observed in salt pillars where stresses are increased in the middle of pillar due to more load carried by the pillar as time grows. After a room was created, material was removed where the stress decreased as shown at the edge and the corner of the pillar. Since a square pillar was modeled, the behavior is symmetrical for the pillar. Therefore, pillar behavior on the right edge would be the same as the pillar behavior on the left edge of the pillar.

The displacement of the pillar was also calculated to ensure that FLAC3D computations were reasonable. Figure 19 is an example of the displacement behavior through time for two locations of the pillar

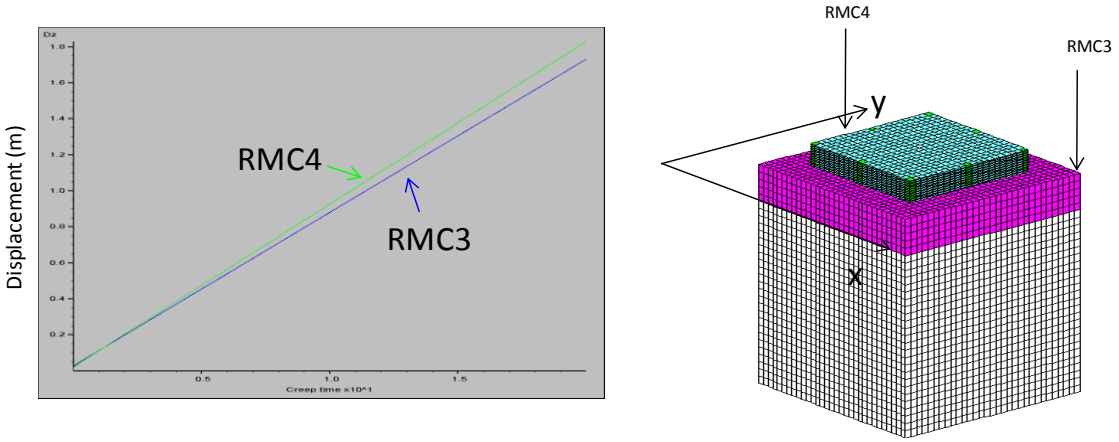

Figure 19. Displacement Calculations in FLAC3D

The displacement histories in Figure 19 were taken in the middle of the excavated room parallel to the center of the pillar (RMC4) and near the corner of the pillar (RMC3). Salt deforms continuously through time as displayed in Figure 19. The transient stage and the steady stage creep are both exhibited in the above figure. The transient stage is not very obvious, but it occurred rapidly. According to Figure 19, 0.04 m of deformation occurred when the model started, and steady state creep was reached shortly after.

The methodology for this project was for FLAC3D to perform three dimensional analyses of the adopted salt pillar. Calibrations were performed to test the mesh sensitivity of the software. From the calibration results, different mesh sizes resulted in different values of maximum vertical stress and convergence rates, but values did not converge with a finer or coarser mesh. The method of analyses was mainly governed by the processing of FLAC3D to produce results for data analyses.

Chapter 7 Results

Trends and patterns were concluded from the modeled results created from FLAC3D, and they are presented in this chapter. The data produced by FLAC3D were summarized to observe for trends and relationships. The convergence rate, vertical stresses, horizontal stresses, and the R value were parameters used for comparisons. The R value is a variable that describes the stress conditions, and it is described in detail in this chapter. All of the fore mentioned parameters were calculated by FLAC3D using either built in or programmed functions.

Patterns were established between the convergence rates and the pillar width to pillar height ratios from analyzing the results. Various parameters were not only used to find trends and patterns, but they were also used to confirm typical salt pillar behavior that has been observed in salt mines. The primary objective of this project was to develop a relationship between the salt thickness and the convergence rate. This was accomplished through simplifying the collected data, and comparing the results with mathematical functions and relations. The effect of room width on the convergence rata was investigated. The purpose was to determine whether various size dimensions with the same pillar width to pillar height ratio produced similar convergence rates. The developed relationship between the salt thickness and the convergence rate, and how the R value can be estimated is included in this chapter.

7.1 Convergence Rate

The behavior of salt pillars is dependent on the creep material immediately above and below the pillar; therefore, the convergence for the pillar is the same as the convergence of the salt roof and salt floor when the salt layer did not exist in the model. The convergence rate of the pillar was obtained by taking the convergence rate along a vertical section in the middle of the room. Figure 20 shows the location of where the convergence rates were taken for all scenarios.

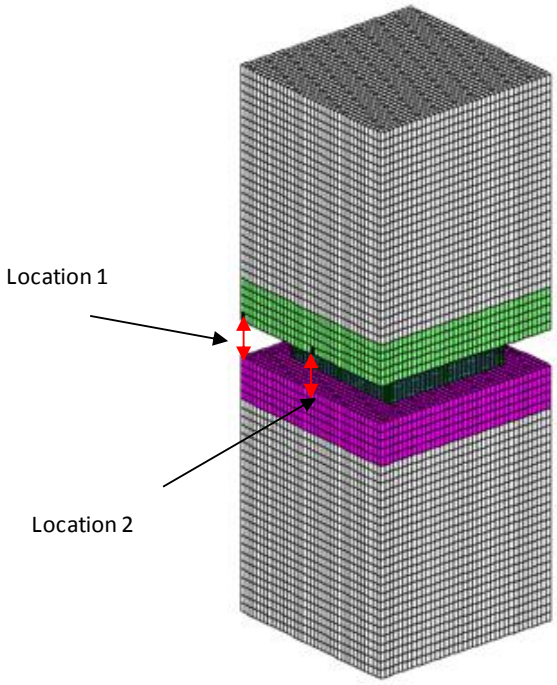

Figure 20. Convergence rate location

Convergence rates along the vertical section of Location 1 and Location 2 in Figure 20 were calculated. The convergence rates at each corner of the salt pillar model is the same as the convergence rates at Location 1; and the convergence rates in the middle of each side of the model is the same as the convergence rates at Location 2. The convergence rates of both locations are very similar, therefore only the convergence rates of Location 1 are presented in Table 7. The convergence rates of Location 2 can be found in Appendix A. The values from Table 4 are plotted onto graphs according to each pillar width to pillar height ratio. Figure 21 is a graph of the convergence rate for the pillar width to pillar height ratio of 1.5 for Location 1.

Table 7. Convergence rates results

W/H	Pillar Width (m)	Room Width (m)	Pillar Height (m)	Convergence Rates (yr^{-1}) at Various Salt Thicknesses							
				0 m	2 m	6 m	10 m	14 m	16 m	20 m	26 m
1.54	23.10	11.00	15.00	2.48×10^{-1}	2.74×10^{-1}	3.02×10^{-1}	3.15×10^{-1}	3.18×10^{-1}	3.18×10^{-1}	3.18×10^{-1}	3.18×10^{-1}
1.50	31.50	15.00	21.00	3.60×10^{-1}	3.89×10^{-1}	4.21×10^{-1}	4.43×10^{-1}	4.53×10^{-1}	4.55×10^{-1}	4.56×10^{-1}	4.57×10^{-1}
1.53	39.75	19.08	26.05	4.50×10^{-1}	4.84×10^{-1}	5.08×10^{-1}	5.47×10^{-1}	5.65×10^{-1}	5.70×10^{-1}	5.76×10^{-1}	5.78×10^{-1}
2.31	23.10	11.00	10.00	9.79×10^{-2}	1.24×10^{-1}	1.53×10^{-1}	1.68×10^{-1}	1.72×10^{-1}	1.73×10^{-1}	1.73×10^{-1}	1.73×10^{-1}
2.30	31.50	15.00	13.70	1.36×10^{-1}	1.66×10^{-1}	1.98×10^{-1}	2.22×10^{-1}	2.34×10^{-1}	2.37×10^{-1}	2.39×10^{-1}	2.40×10^{-1}
2.29	39.75	19.08	17.35	1.77×10^{-1}	$2.\times10\times10^{-1}$	2.35×10^{-1}	2.76×10^{-1}	2.96×10^{-1}	3.02×10^{-1}	3.09×10^{-1}	3.12×10^{-1}
3.80	23.10	11.00	6.08	2.24×10^{-2}	4.16×10^{-2}	6.84×10^{-2}	8.51×10^{-2}	9.07×10^{-2}	9.15×10^{-2}	9.20×10^{-2}	9.21×10^{-2}
3.80	31.50	15.00	8.29	3.07×10^{-2}	5.15×10^{-2}	7.05×10^{-2}	1.04×10^{-1}	1.18×10^{-1}	1.22×10^{-1}	1.25×10^{-1}	1.27×10^{-1}
3.80	39.75	19.08	10.46	3.97×10^{-2}	6.24×10^{-2}	9.38×10^{-2}	1.20×10^{-1}	1.41×10^{-1}	1.49×10^{-1}	1.58×10^{-1}	1.63×10^{-1}
4.62	23.10	11.00	5.00	1.14×10^{-2}	2.69×10^{-2}	5.17×10^{-2}	6.84×10^{-2}	7.45×10^{-2}	7.55×10^{-2}	7.61×10^{-2}	7.61×10^{-2}
4.60	31.50	15.00	6.85	1.58×10^{-2}	3.24×10^{-2}	5.86×10^{-2}	8.14×10^{-2}	9.56×10^{-2}	9.95×10^{-2}	1.03×10^{-1}	1.05×10^{-1}
4.58	39.75	19.08	8.67	2.07×10^{-2}	3.86×10^{-2}	6.65×10^{-2}	9.17×10^{-2}	1.12×10^{-1}	1.20×10^{-1}	1.29×10^{-1}	1.35×10^{-1}
4.60	38.01	10.86	8.26	3.26×10^{-3}	6.20×10^{-3}	1.19×10^{-2}	1.66×10^{-2}	1.89×10^{-2}	1.94×10^{-2}	1.99×10^{-2}	2.00×10^{-2}
4.60	16.20	10.80	3.52	2.74×10^{-2}	7.51×10^{-2}	1.42×10^{-1}	1.77×10^{-1}	1.86×10^{-1}	-	1.87×10^{-1}	1.87×10^{-1}
4.60	11.00	11.00	2.39	8.56×10^{-2}	2.76×10^{-1}	4.98×10^{-1}	5.80×10^{-1}	5.91×10^{-1}	-	5.92×10^{-1}	5.92×10^{-1}

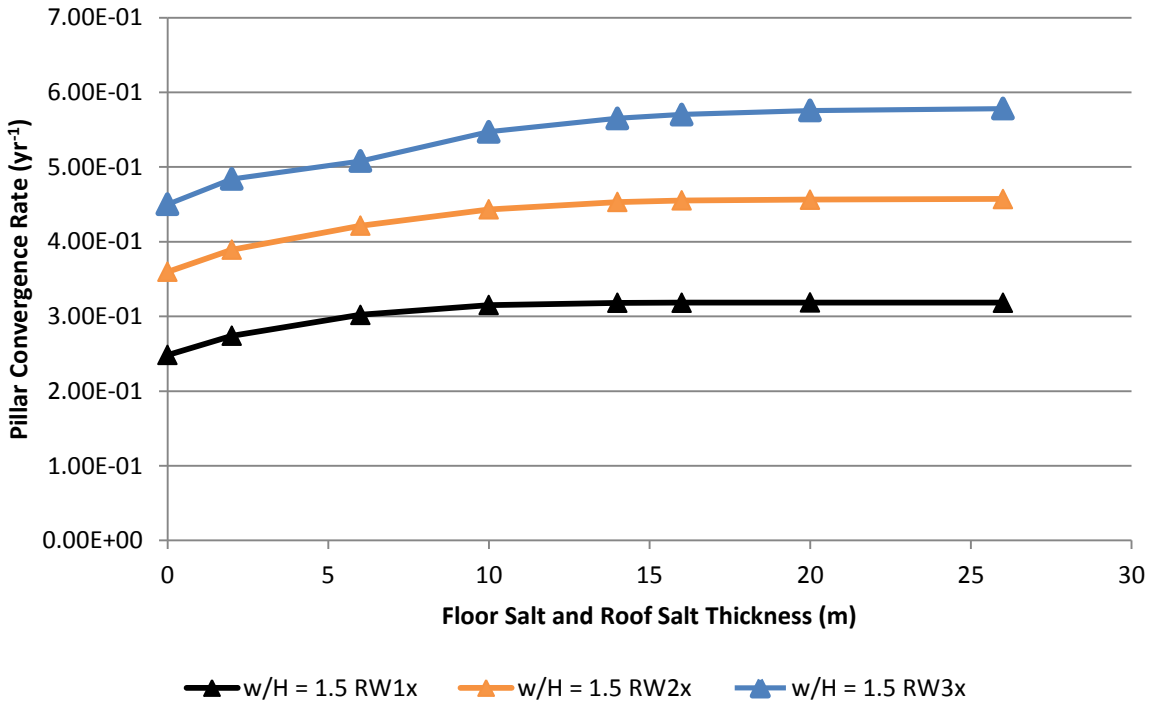

Figure 21. Convergence Rates for Pillar Width to Pillar Height Ratio of 1.5 for Location 1

The legend in Figure 21 explained that a different room width was used for each pillar width to pillar height ratio. RW1x is a room width of 11 m; RW2x is a room width of 15 m which is 1.4 times of the original room width of 11 m; and RW3x is a room width of 19.1 m which is 1.7 times of the original room width. Changing the room widths resulted in changing the pillar widths and pillar heights accordingly to maintain the same pillar width to pillar height ratio. Each set of pillar and room dimensions were summarized in Table 2. Figure 22, Figure 23, and Figure 24 are the graphs for the pillar width to pillar height ratios of 2.3, 3.8 and 4.6 respectively.

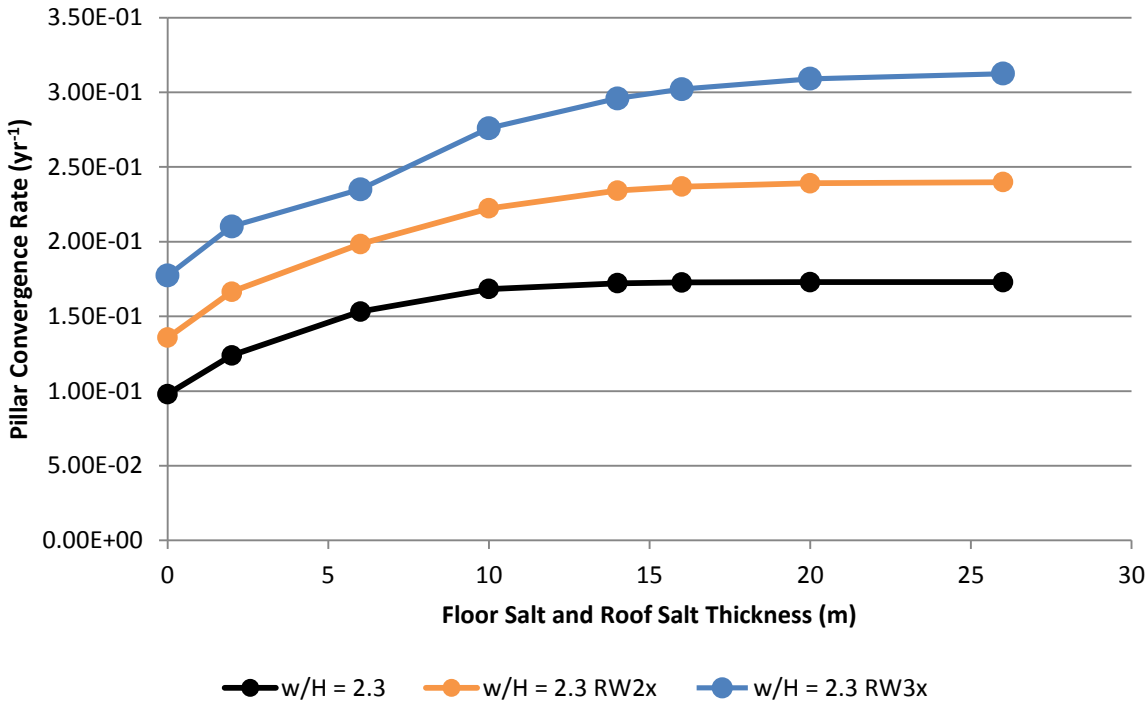

Figure 22. Convergence Rates for Pillar Width to Pillar Height Ratio of 2.3 for Location 1

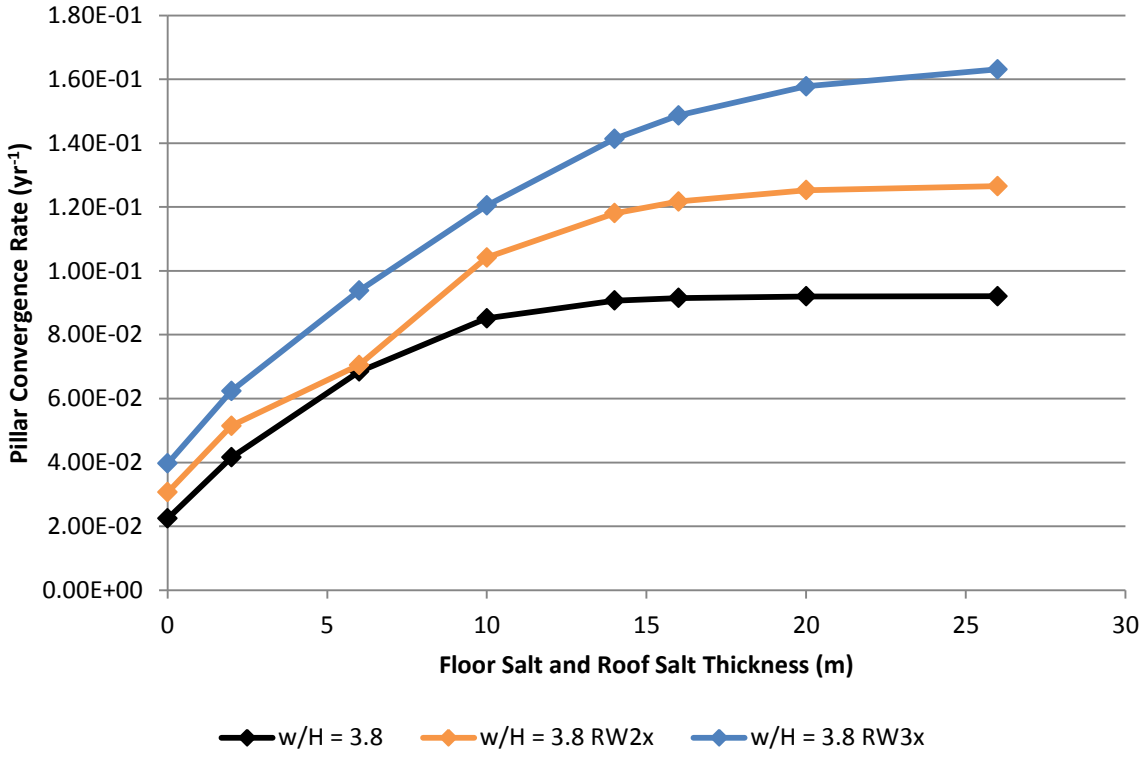

Figure 23. Convergence Rates for Pillar Width to Pillar Height Ratio of 3.8 for Location 1

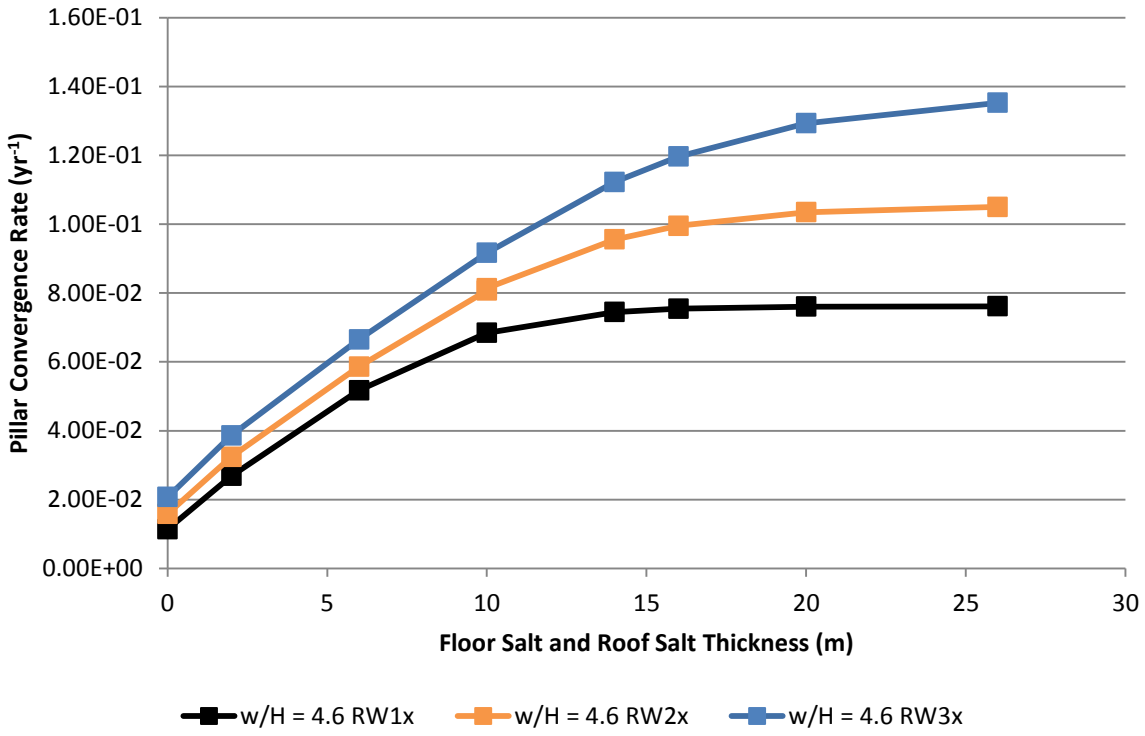

Figure 24. Convergence Rates for Pillar Width to Pillar Height Ratio of 4.6 for Location 1

The general trend of convergence rates shown in Figure 21 to Figure 24 was the convergence rates increased as the pillar width to height ratios decreased. Larger room widths resulted in higher convergence rates for each pillar width to height ratio. Therefore; the largest room width (RW3x) resulted in the highest convergence rate for each pillar width to pillar height ratio; and the smallest room width resulted in the lowest convergence rate for each pillar width to pillar height ratio. As the room width increased, the convergence rate increased for all thicknesses of salt. A common trend for all four pillar width to pillar height ratios was the convergence rates started to stabilize at approximately 15 m of salt thickness. This is due to the limitations of the stress bulb, where the overbearing capacity affects the stress in the underlying material until a certain depth.

The salt thickness at which the convergence rate stabilized decreased as the pillar width to height ratio decreased. For the room width of 11 m, the convergence rate began to stabilize at 10 m of salt for the pillar width to height ratio of 1.5; the convergence rate began to stabilize at 14 m of salt for the pillar width to height ratio of 2.3; and the convergence rate stabilized

at 16 m of salt for the pillar width to height ratio of 3.8 and 4.6. The salt thickness for which the convergence rate stabilized is also dependent on the size of the room width, and all four pillar width to height ratios exhibited the trend that larger room widths required thicker salt layers for the convergence rate to stabilize. There is the least difference in the convergence rates among different room widths at salt thicknesses less than 10 m for the pillar width to pillar height ratio of 4.6 compared to the other pillar width to pillar height ratios. As the pillar width to pillar height ratio decreased, the shape of the curves were nearly identical and the convergence rate at 0 m salt thickness determined where the curve begins. However, the convergence rates were very similar at thin salt layers until approximately 10 m, and then the curve stabilized at thicker salt layers for larger room widths for pillar width to pillar height ratios. The convergence rate at 0 m not only defined where the curves began within each pillar width to height ratio, but also for individual pillar width to pillar height ratios.

7.1.1 Convergence Rates of Location 2

All the fore mentioned trends can be found in the results of Location 2. The convergence rate graphs for Location 2 were very similar to the graphs in Figure 21 to Figure 24. Most of the data points at salt thickness of 6 m and 10 m for Location 2 were 10% larger than Location 1 or less. However, there were a few data points for Location 2 that were 15% to 20% larger than Location 1. All of the data for the pillar width to pillar height ratio of 1.5 was less than 4%; and all of the data for the pillar width to pillar height ratio of 2.3 was less than 7%. Figure 25 to Figure 28 show the percentage differences for convergence rates between Location 1 and Location 2 of each salt thickness at each pillar width to pillar height ratio.

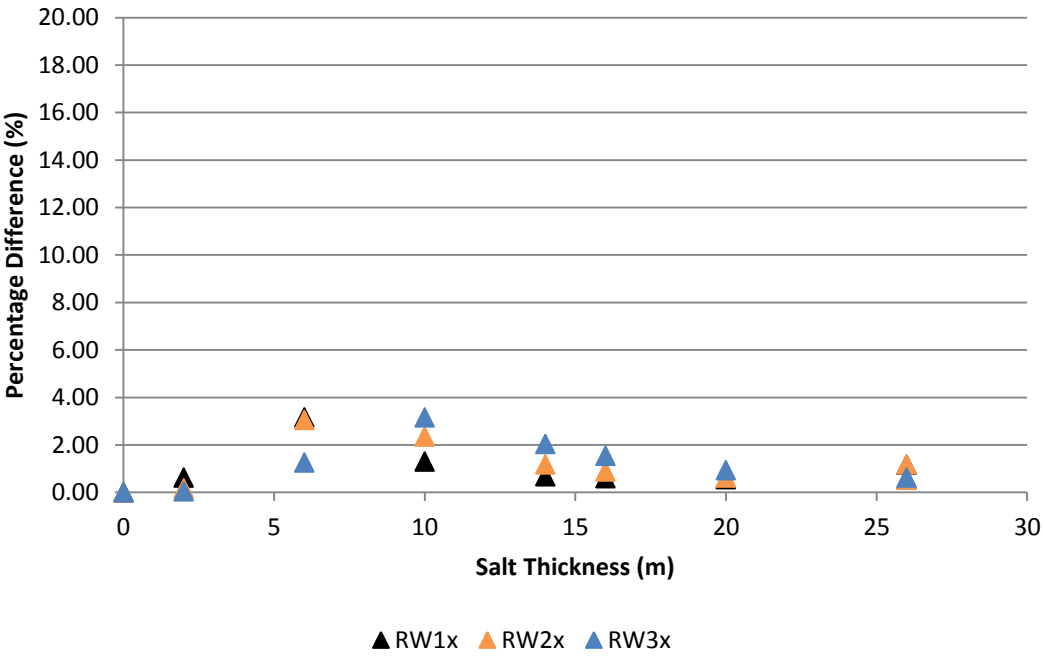

Figure 25. Percentage Difference for the Pillar Width to Pillar Height Ratio of 1.5

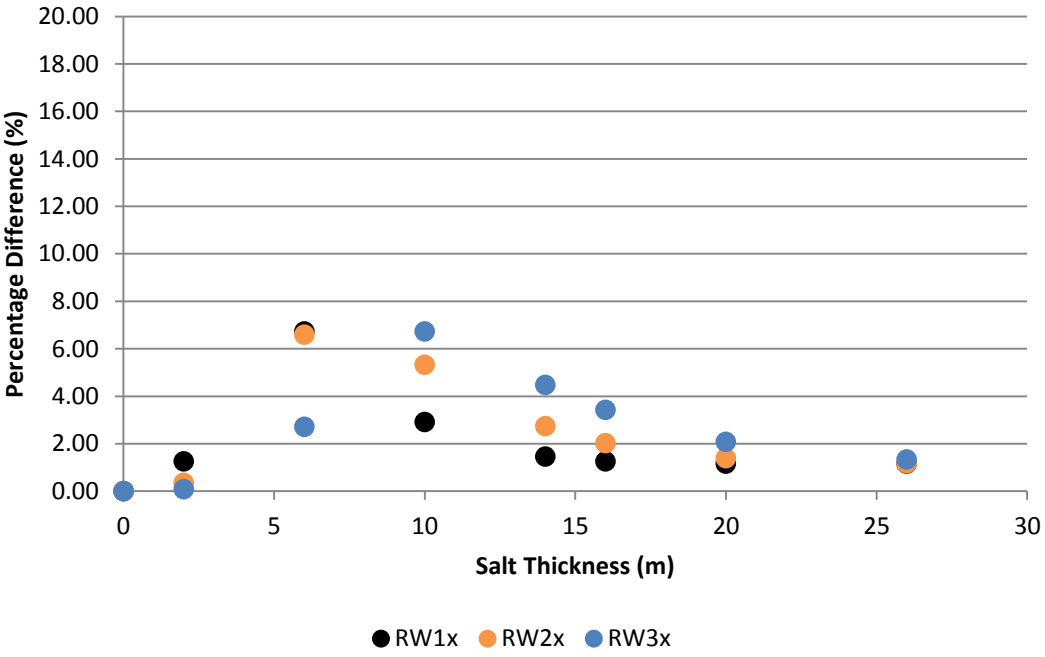

Figure 26. Percentage Difference for the Pillar Width to Pillar Height Ratio of 2.3

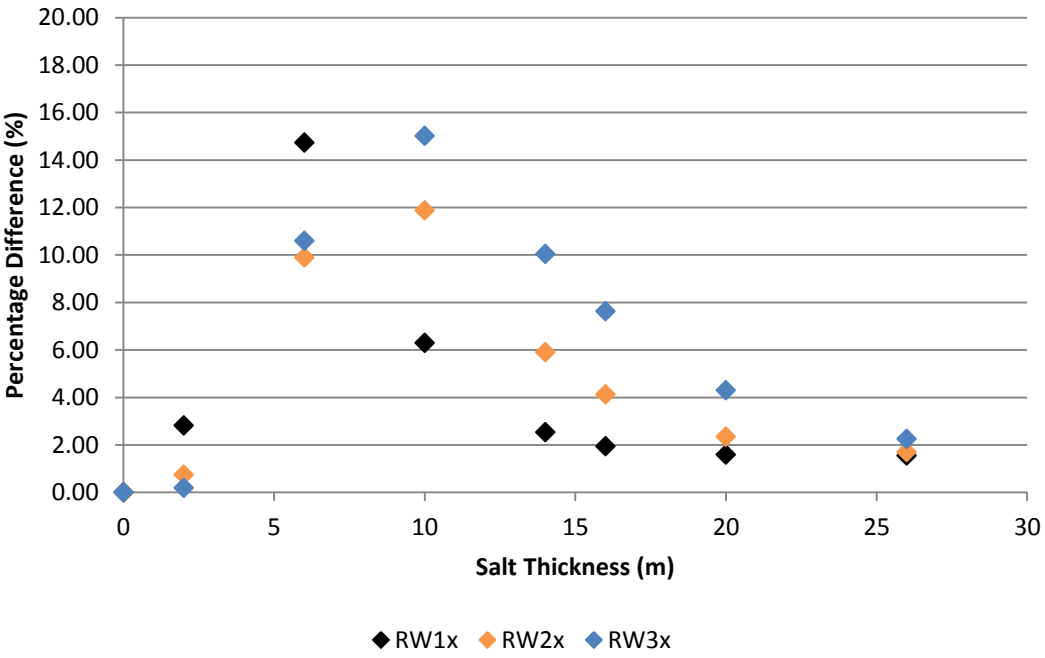

Figure 27. Percentage Difference for the Pillar Width to Pillar Height Ratio of 3.8

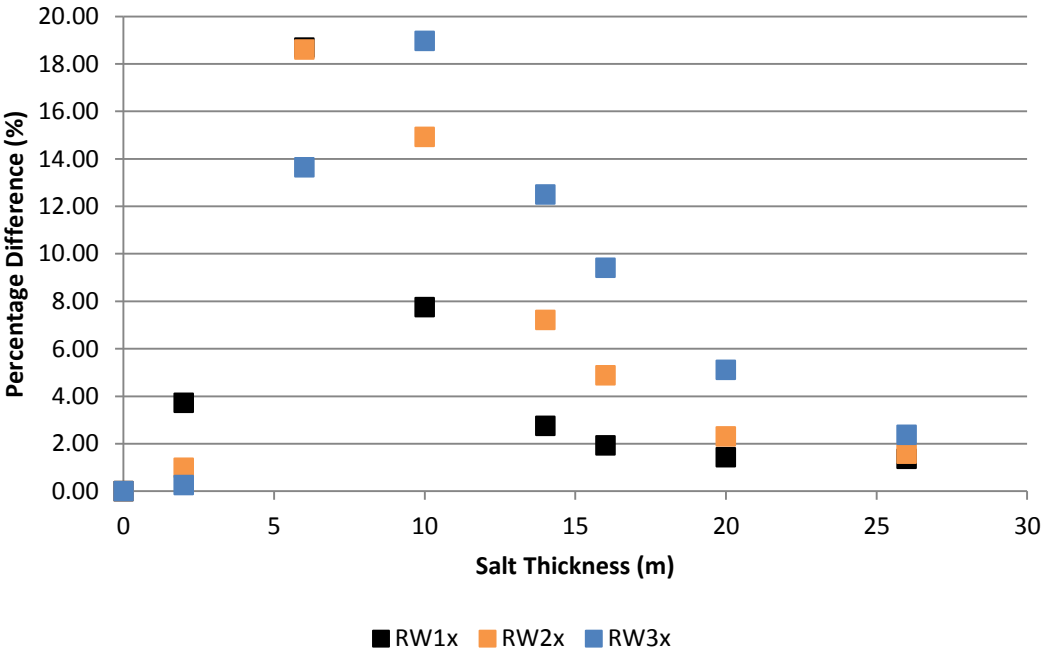

Figure 28. Percentage Difference for the Pillar Width to Pillar Height Ratio of 4.6

The percentage difference for the pillar width to pillar height ratio of 1.5 was the least for all salt thicknesses and the largest for the pillar width to pillar height ratio of 4.6. The percentage difference for the convergence rate decreased as the pillar width to pillar height ratio decreased. The largest percentage difference is at salt thicknesses of 6 m or 10 m for every pillar width to pillar height ratio. The percentage difference exponentially decreased as the salt thickness decreased and increased from the largest percentage difference at 6 m or 10 m. The percentage difference was the largest at the salt thickness of 6 m for room widths of 11 m and 15 m; and the percentage difference was the largest at the salt thickness of 10 m for the room width of 19 m. The room width had minimal effect on the percentage difference.

7.2 R Value

Before an empirical relationship was developed to relate the salt thickness and the convergence rate, the effective stress to reference stress ratio was examined. The single mechanism law was rewritten in the form of:

$$\dot{\varepsilon_{ss}} = \dot{\varepsilon}_0 \left(\frac{\sigma}{\sigma_0} \times \frac{\bar{\sigma}}{\bar{\sigma}} \right)^n \tag{12}$$

The above function was then rewritten as:

$$\dot{\varepsilon_{ss}} = \dot{\varepsilon}_0 \left(R \frac{\bar{\sigma}}{\sigma_0} \right)^n \tag{13}$$

Where, the R value is then the ratio between effective stress and average in situ stress which is a function of the vertical stress. The purpose for this R value is determining the R value would be sufficed to estimate for the compression rate of the pillar without knowing the effective stresses. Figure 29 displays the relationship between the R value the pillar width to pillar height ratio for various salt thicknesses.

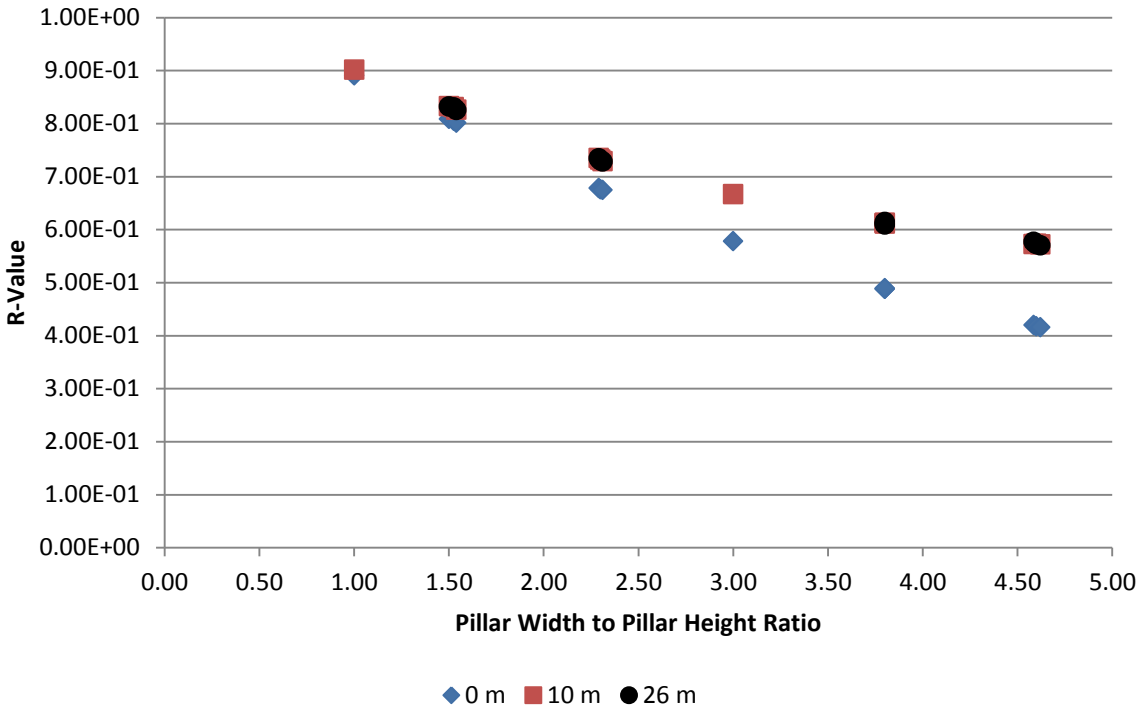

Figure 29. R values for 0 m, 10 m, and 26 m of salt thickness for pillar compression

Pillar width to pillar height ratios of 1.00 and 3.00 were modeled using room widths of 11 m and 15 m, respectively to complete the R value trend. According to Figure 29, there was a linear relationship between the R value and the pillar width to pillar height ratio for 0 m of salt thickness. However, the R value then began to exponentially decrease for salt thicknesses from 10 m to 26 m. Once the salt thickness was equal to and/or larger than 10 m, the R-value remained constant. There were very little differences in R values for the pillar width to pillar height ratio of 1.0 at various salt thicknesses. This difference increased as the pillar width to pillar height ratio increases. It can then be concluded that the R value is a function of the pillar width to pillar height ratio and salt thickness. Knowing the R value, average stress, transition stress, and strain rate can allow for the prediction of the rate of pillar compression.

7.3 Pillar Behavior

Pillar behavior is observed in terms of deformation and stresses. In a typical mine panel, the overburden weight is distributed among the pillars and the abutments. If one pillar fails, then

the load is redistributed among the remaining pillars and abutments. The stresses existing in the pillars directly affect the creep rates in the pillars. As the average vertical stress increases for the cross section of the pillar, the convergence rates increase as well. To further describe pillar behavior, numerous graphs were plotted but only a select few were included for detailed description. All of the graphs of vertical stress and R value for each salt stratum thickness can be found in Appendix B.

In a vertical profile of a salt pillar from the ground surface to the elastic material below the salt floor, the vertical stress decreased as the vertical and horizontal distance decreased from the center of the pillar until the stresses were redistributed through the strata above and below the pillar. In other words, the vertical stress is the largest at the center and edges of the pillar. When a salt stratum exists immediately above and below the mine, there is more salt medium to undergo deformation and stress redistribution. Figure 30 compares the vertical stress distribution at the center of the pillar for the pillar width to pillar height ratio of 3.8 for various thicknesses of salt stratum above and below the pillar.

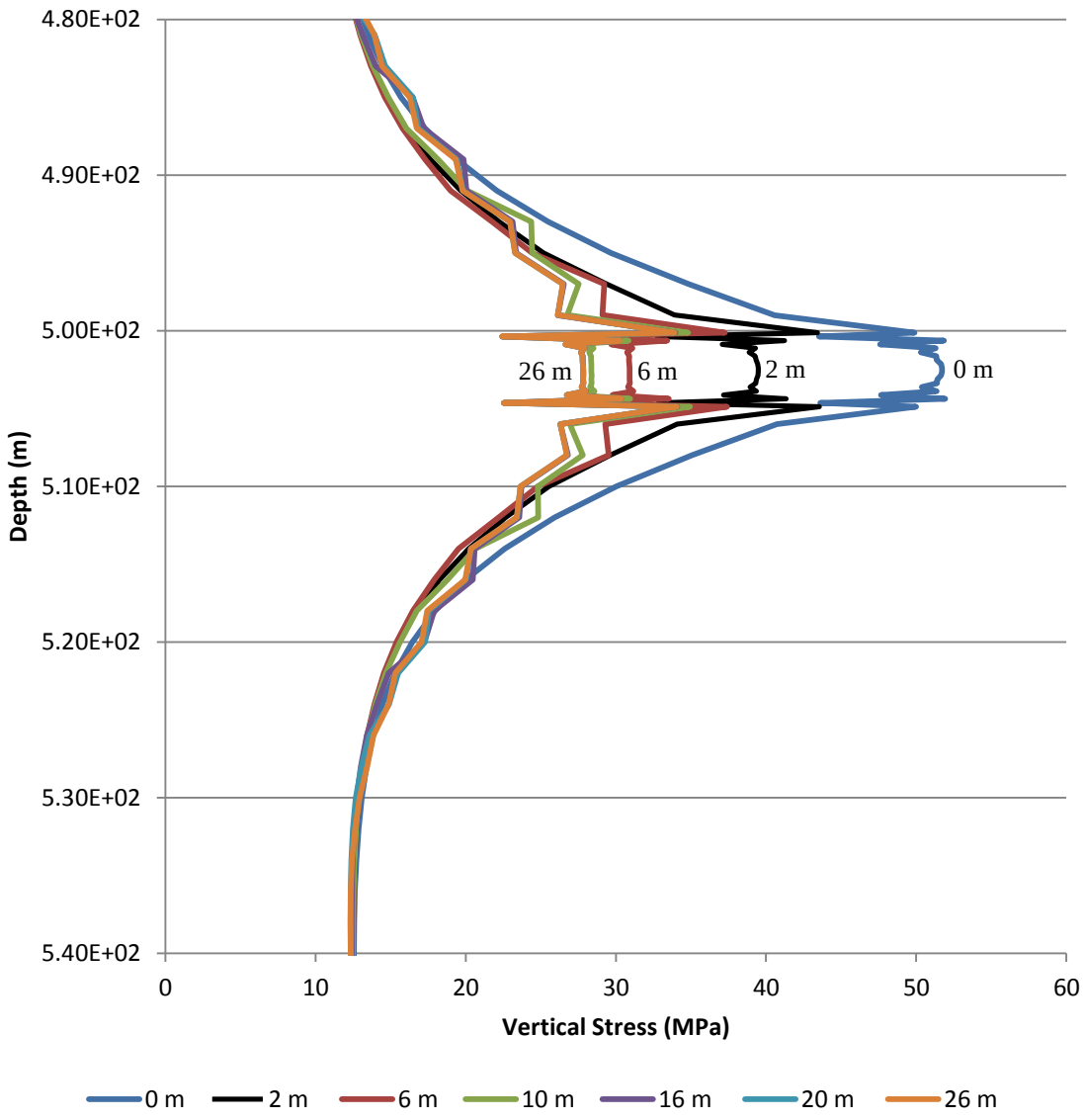

Figure 30. Vertical stress distribution at the center of a pillar

Figure 30 illustrated the vertical stress distribution for salt thicknesses of 0 m to 26 m for the pillar width to pillar height ratio of 4.6. Vertical stresses were the largest in the pillar for 0 m of salt thicknesses compared to salt stratum larger than 0 m. A non-existent salt stratum above and below the pillar confines the behavior of the pillar, and there is very little upheaval of the floor and sinking of the roof and nearly no displacement of the pillar. The existence of salt layers above and below the pillar increased deformation in the salt roof and salt floor. The floor up heave and sagging of the roof then increased as the salt stratum above and below the pillar increased, and pillar punching starts to occur. The vertical profile at the

center of the pillar for horizontal stress was also plotted and presented in Figure 31. The salt stratum above and below the pillar affected the horizontal stresses more than the vertical stresses. The horizontal stress immediately increased at the depth of where the salt stratum started, and the maximum horizontal stress existed at the center and edges of the pillar.

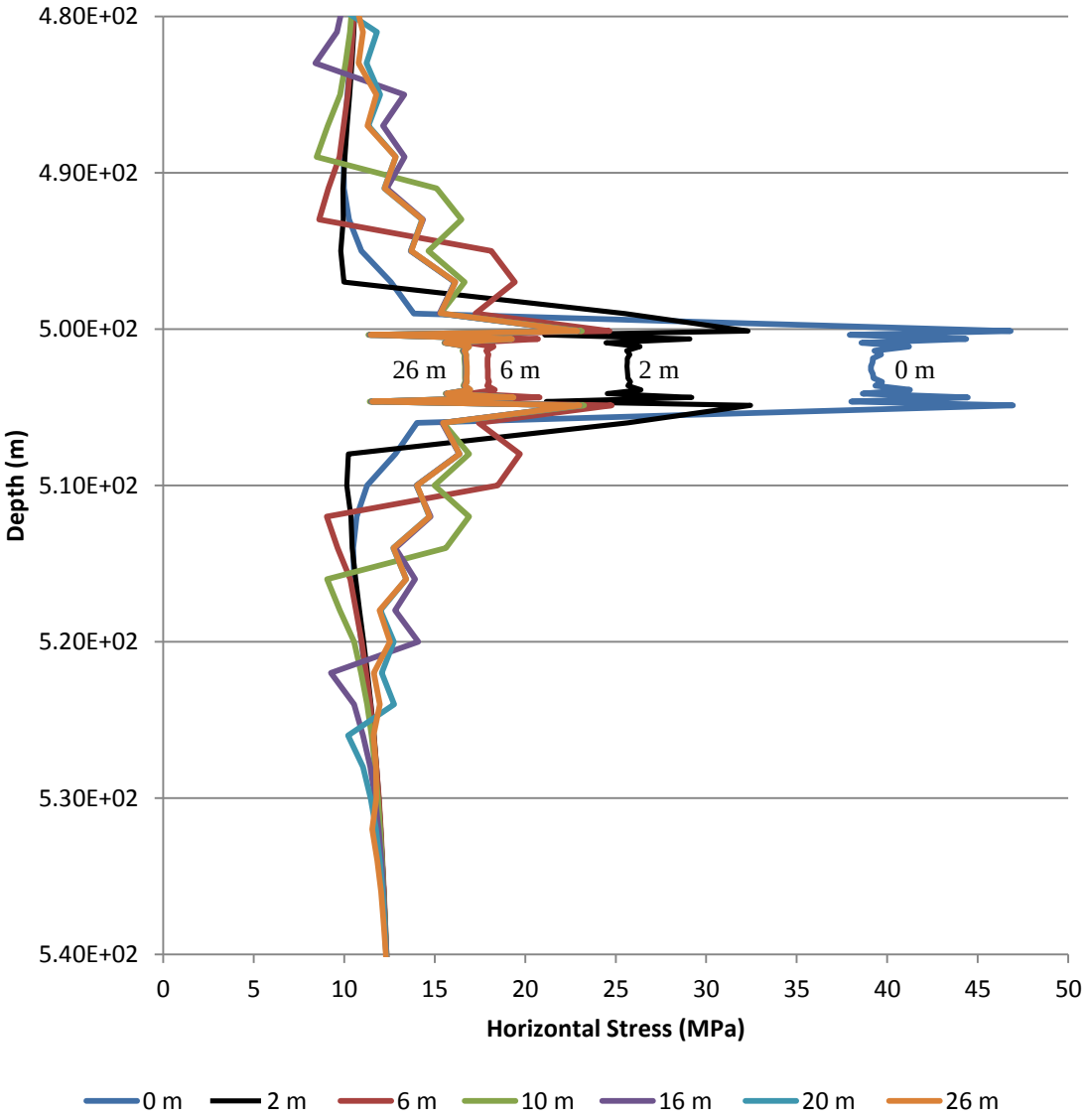

Figure 31. Horizontal stress distribution at the center of a pillar

The horizontal stress is proportional to the vertical stress; therefore, the horizontal stresses at the pillar were also the largest for no salt strata above and below the pillar, and the horizontal stresses decreased as the salt strata thickness increased. The horizontal stress was modeled to

be zero for the strata above and below the pillar, regardless of the thickness of the salt strata above and below the pillar.

The vertical and horizontal stress for a horizontal profile was also obtained from the center of the pillar as shown in Figure 32.

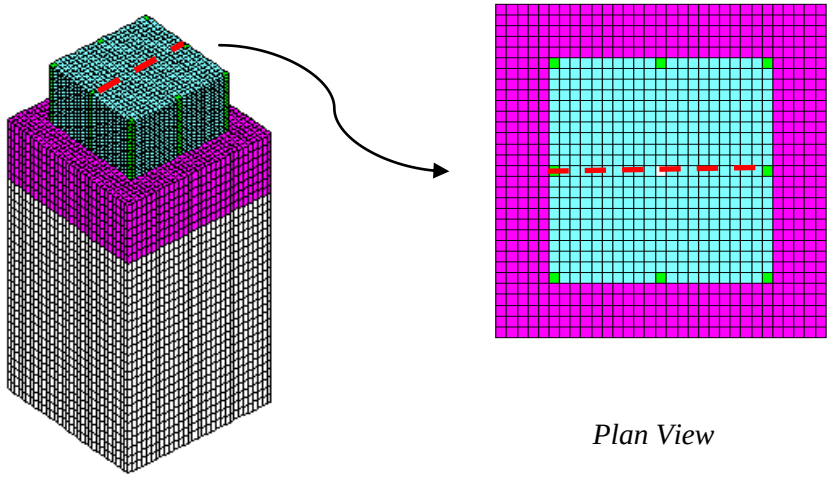

Figure 32. Cross Section of the Center of the Pillar

The average value along the height of the pillar of the vertical stress and R value for the cross section of the center of the pillar were taken. The relationship between vertical stress and the R value is shown in the following two figures for the salt thickness of 0 m for the room width and pillar width of 11.0 m and 23.1 m, respectively. In the case of the pillar width of 11.0 m, the center of the pillar is at 18 m in the x and y direction.

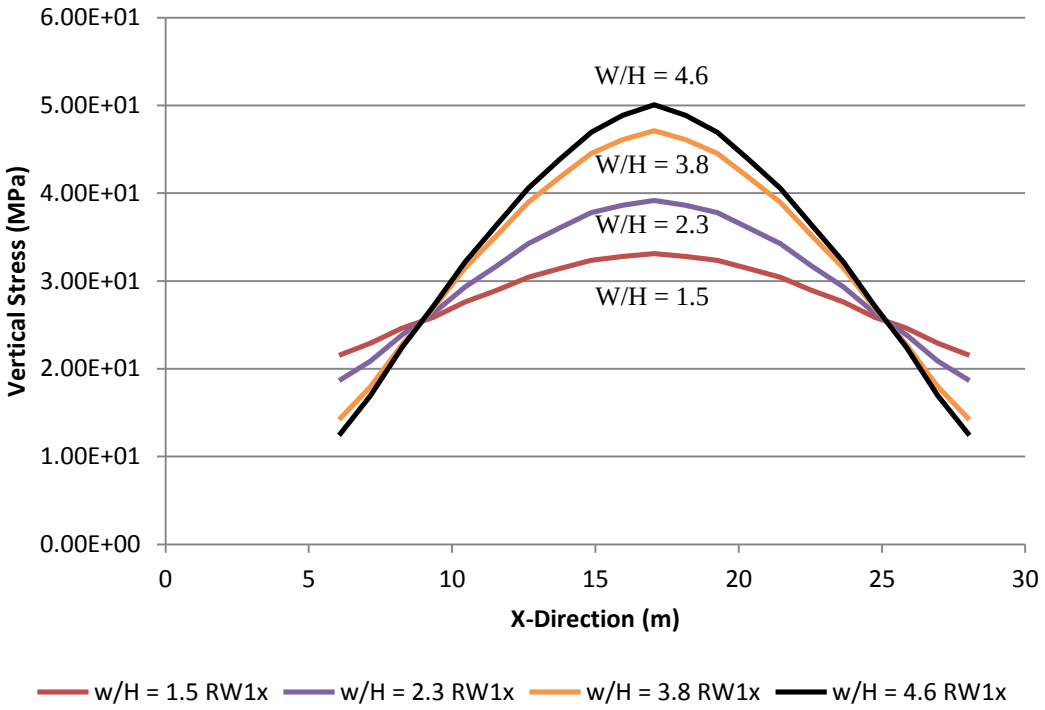

Figure 33. Vertical Stress for 0 m of Salt Thickness

Figure 33 showed the stress distribution for all four pillar width to pillar height ratios. The average vertical stress increased with increasing pillar width to pillar height ratio. This was also demonstrated by Potts (1964), the unconfined compressive strength increased as the width to height ratio increased for specimens of Winsford salt. The shape of the stress distribution is a typical stress distribution for pillars. The maximum stress existed in the middle of the pillar, and there was minimal or no stress at the edges of the pillar. This trend was also observed in the vertical profile of the center of the pillar, where the least pillar width to pillar height ratio exhibited the least amount of vertical stress. However, the vertical profile of the pillar in Figure 30 indicated large stresses at the top and bottom of the pillar. The reason for this difference is Figure 33 displayed average values vertically across the pillar, and Figure 30 displayed the values of elements along the vertical profile at the exact center of the pillar.

From observing the vertical stress distributions of all of the results, the vertical stress decreased for all pillar width to pillar height ratios as the salt layers above and below pillar

increased. The stress distribution curves began to flat out as the salt layers increased in thickness. The pillar width to pillar height ratios of 3.8 and 4.6 also exhibited the least stress when the salt stratum above and below the pillars were larger than 10 m.

The horizontal stress (σ_{xx}) exhibited a similar shape, where the maximum horizontal stress was in the center of the pillar too. Figure 34 showed the horizontal stress distribution for 0 m of salt thickness.

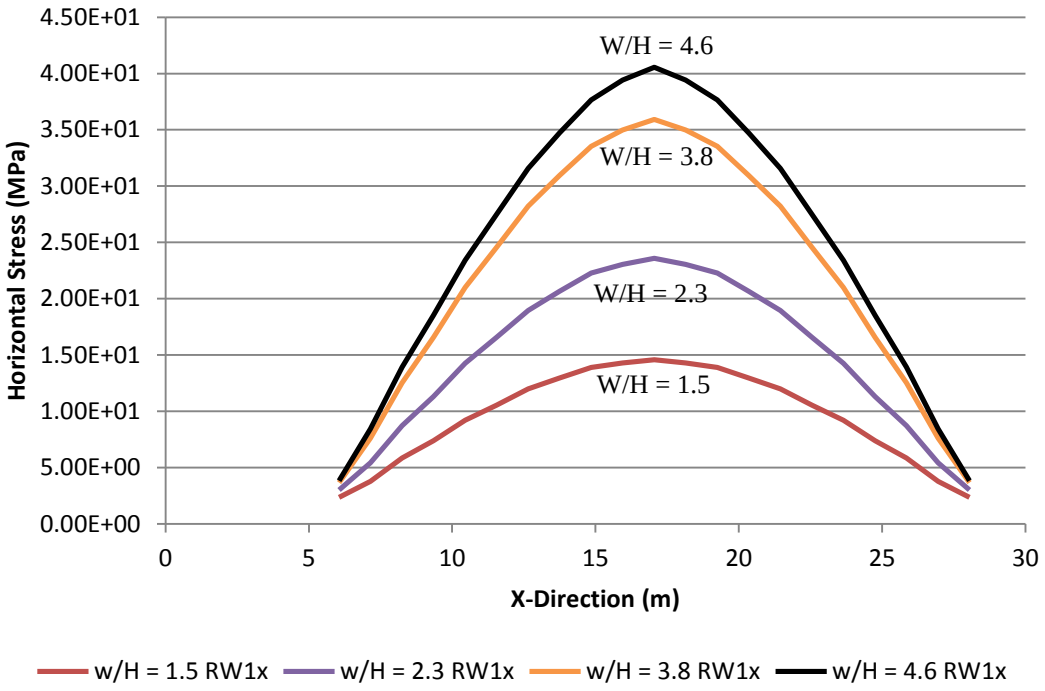

Figure 34. Horizontal stress for 0 m of salt thickness

The horizontal stress exhibited a stress distribution similar to the vertical stress, where the maximum horizontal stress is in the center of the pillar. The vertical profile of the horizontal stress at the center of the pillar in Figure 31 also displayed values at the center of the pillar, and the values in Figure 34 were averaged values across the pillar. Therefore, the vertical and horizontal profiles do not show the exact same trend. The horizontal stress is less than the vertical stress since the ratio of horizontal to vertical stress is usually less than one. The horizontal and vertical stresses determine the effective stresses, which are directly related to the R value. Figure 35 is the R value distribution for 0 m of salt thickness.

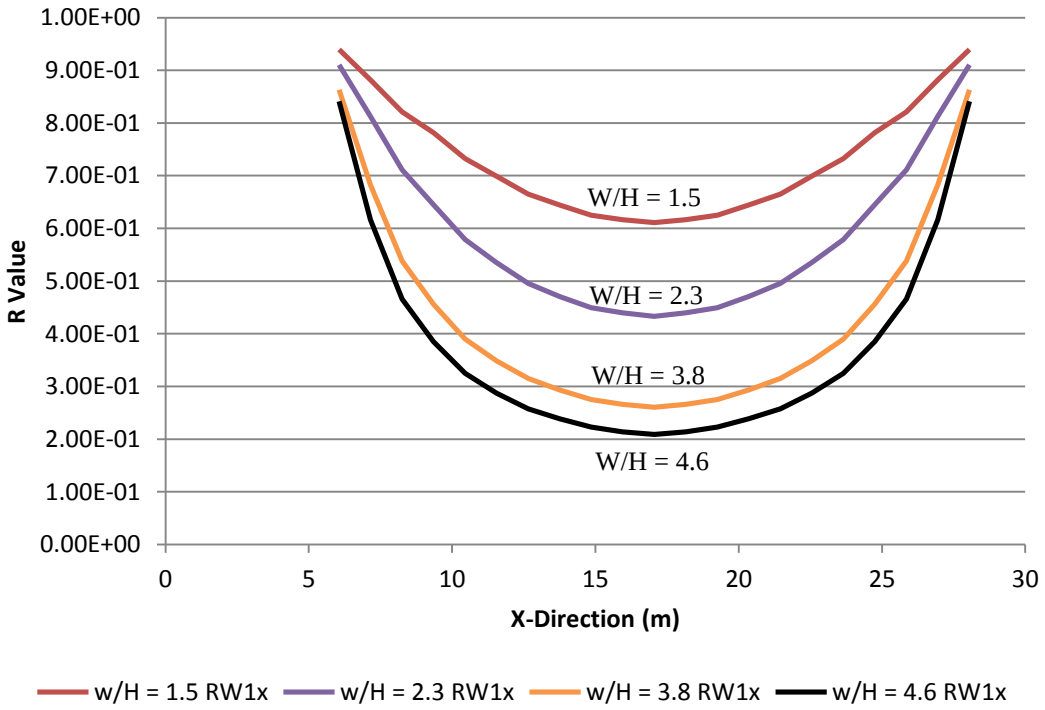

Figure 35. Average R value for 0 m of salt thickness

The R value ranged between zero and one. The R value does not exceed one because the effective stress will not exceed the vertical stress. Therefore, as the vertical stress increases, the R value decreases. The shape of the curves in Figure 33 and Figure 35 were the same for all of the salt thicknesses and the corresponding pillar width to pillar height ratio, but the values were not the same. Different room widths exhibited the same curve shapes, but the width of the parabolas increased as the room and pillar widths increased. All salt thicknesses exhibited an upright parabola for the R value and a downward parabola for the vertical stresses, and these graphs can be found in Appendix B.

7.4 The Relationship between Convergence Rate and R Value

To determine any trends or relationships within the modeled pillar width to pillar height ratios, the modeled convergence rates were normalized to the corresponding pillar width. An average was taken for each pillar width to pillar height ratio using the results of different

dimensions for each pillar width to pillar height ratio. The results showed in Figure 21 to Figure 24 were then simplified to Figure 36.

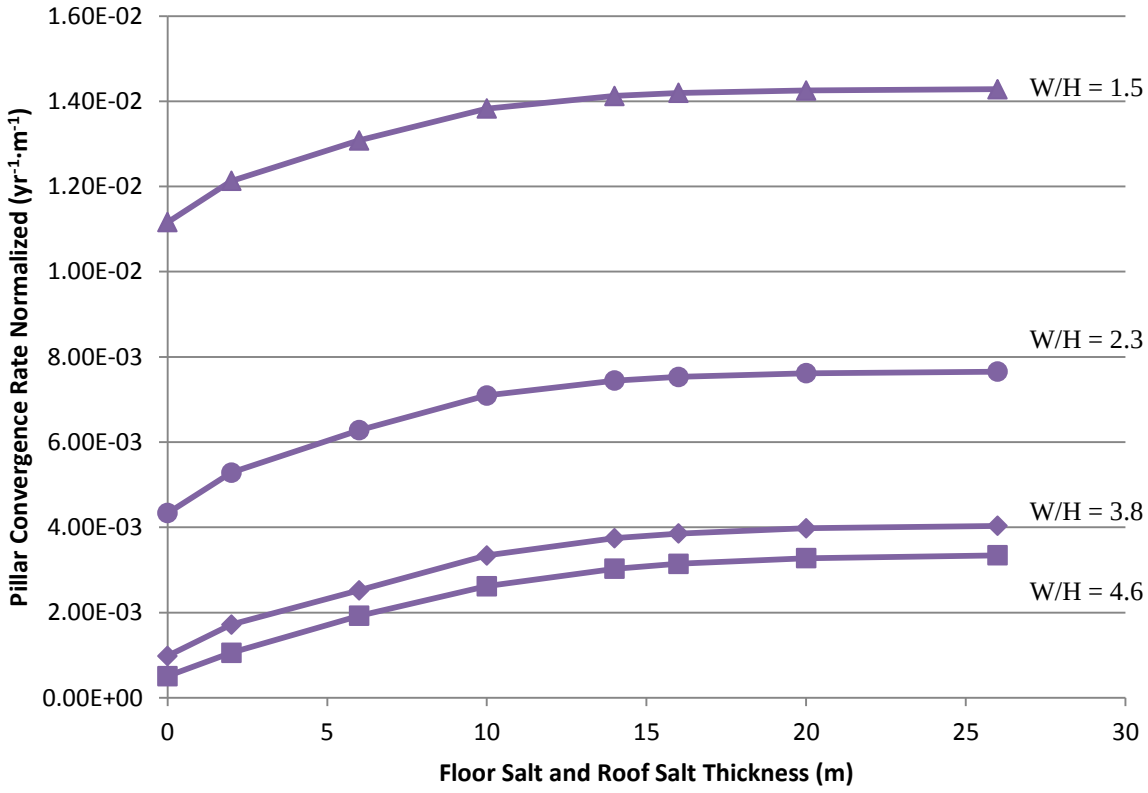

Figure 36. Average convergence rate values

It was found that the normalized convergence rates and the shapes of the curves in Figure 21 to Figure 24 all showed an exponential relationship between the salt thickness and the convergence rates. After the convergence rates were normalized to the corresponding pillar width, the main difference among all the pillar width to pillar height ratios was the convergence rate at 0 m of salt thickness for each pillar width to pillar height ratio. The convergence rate at larger than 0 m of salt thickness exhibited very similar shapes. Therefore, two components were required to describe the relationship between the convergence rate and the salt thickness. The first component is not dependent on the pillar width to pillar height ratio, and it describes the relationship between convergence rate and salt thicknesses larger than 0 m. The second component is dependent on the pillar width to pillar height ratio, and it describes the relationship between convergence rate and the salt thickness at 0 m.

The exponential function shown below was used as a starting point to develop the final relationship between convergence rate and salt thickness.

$$f(T) = 1 - e^{-\alpha T} \tag{14}$$

Where, T is the thickness of salt above and below the pillar in meters; and α is a unit less constant dependent on the pillar width to pillar height ratio. A unit less constant, β was introduced to adjust the shape of *f(T)* for a more accurate numerical relationship between the convergence rate and salt thicknesses greater than 0 m, which formed $f_1(T)$.

$$f_1(T) = \beta \times (1 - e^{-\alpha T}) \tag{15}$$

A linear relationship was found between α and the pillar width to pillar height ratio. The values for the slope and the y-intercept of the linear relationship are -0.0052 and 0.1365, respectively. The expression for the constant α is the following:

$$\alpha\left(\frac{W}{H}\right) = -0.0052\left(\frac{W}{H}\right) + 0.1365 \tag{16}$$

β was found to be a constant of 0.1027 for the various modeled pillar width to pillar height ratios. Function f_1 is only applicable to salt thicknesses greater than 0 m of salt, where it can only calculate the shape of the convergence curve and not the convergence rate for 0 m.

Another function was required to add to f_1 to determine the convergence rate for 0 m of salt thickness. The convergence rate for 0 m of salt thickness was plotted against the corresponding pillar width to pillar height ratio. An exponential relationship was found between the convergence rate at 0 m of salt thickness and the pillar width to pillar height ratio. The following expression describes the fore mentioned relationship.

$$f_2\left(\frac{W}{H}\right) = c \times e^{-d \times \frac{W}{H}} \quad (17)$$

Where, *c* and *d* are coefficients determined by drawing a relationship between all of the convergence rates at 0 m of salt thickness for each modeled pillar width to pillar height ratio. The coefficients were found to be 1.828 and 1.072 for coefficients *c* and *d*, respectively.

Since the R value is dependent on the pillar width to pillar height ratio, f_1 and f_2 are functions that make up the R value. In other words, the R value has the following expression:

$$R = \sqrt[3]{\frac{W}{H} \times (f_1 + f_2)} \quad (18)$$

The empirical function for calculating the convergence rate for a certain pillar height is the following expression:

$$\dot{\varepsilon} = \dot{\varepsilon}_0 H (R \frac{\bar{\sigma}}{\sigma_0})^3 \quad (19)$$

To validate the developed expression, the convergence rates from the modeling results were compared to the results calculated from the developed expression. Figure 37 presents all of the modeled data for pillar width to height ratios of 1.5 to 4.6. Three additional simulations of extraction ratios of 0.40, 0.64, and 0.75 for the pillar width to pillar height ratio of 4.6 were performed to determine if the developed empirical function would be applicable to any extraction ratio. The percentage error ranged between 0% and 30% for salt thicknesses above and below the pillar of 10 m or less. For the extraction ratio of 0.54, the percentage difference between the modeled and the calculated values was less than 20%. The majority of the error occurs for salt thicknesses of less than 10 m regardless of the extraction ratio.

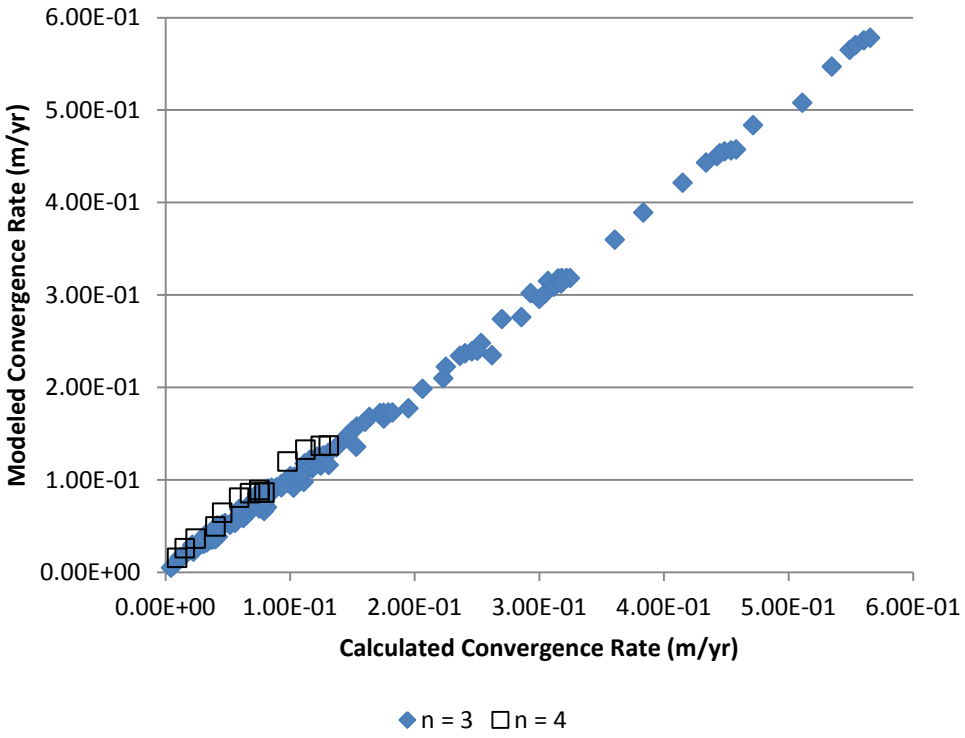

Figure 37. Modeled data and calculated data

The coefficient of determination between the calculated and modeled values was 0.99; and the average percentage difference between the modeled and calculated values was 11.29 percent. A set of data was modeled with a power law exponent of four, and it was found that there was more error compared to the power law exponent of three. The developed function was calibrated to fit materials governed by the third power law which resulted in more error when the power law exponent of four was used.

In order for the developed relationship to be applicable for a wide range of salt mine scenarios, the R values calculated from functions f_1 and f_2 were summarized for all of the simulated scenarios and shown in the following Figure 38. Functions f_1 and f_2 were derived from curve fitting methods for the convergence rate of the rooms. Whereas, the R values in Figure 29 were derived from pillar compression.

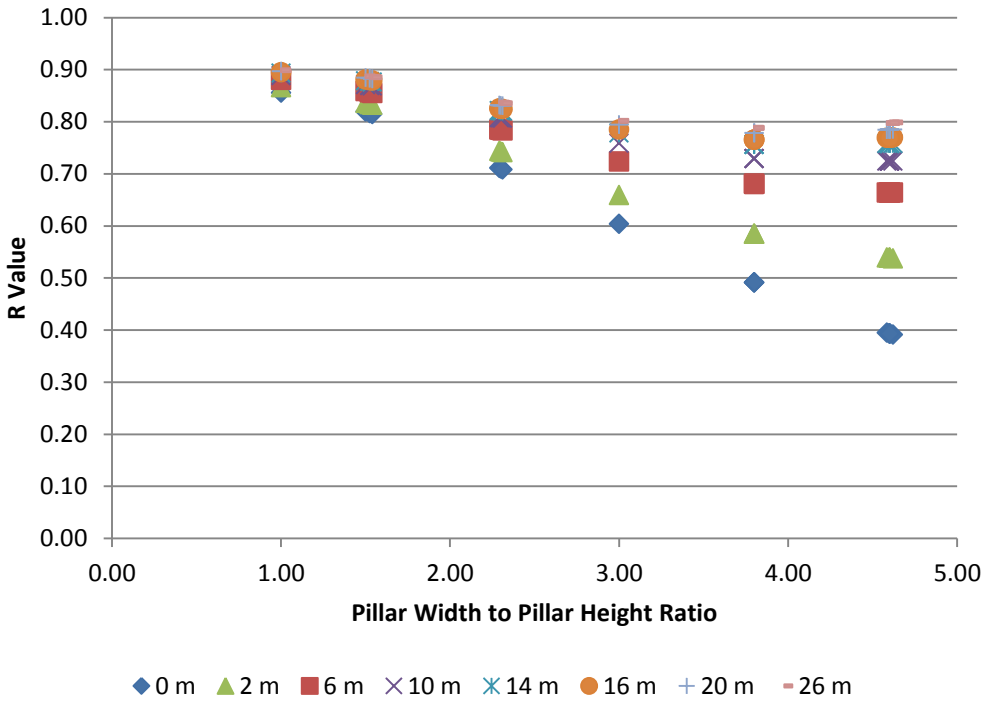

Figure 38. R Value for room convergence

The R values calculated from functions f_1 and f_2 showed trends similar to the R values for pillar compression. The R value decreased as the pillar width to pillar height ratio increased, and the R value increased as the salt thickness increased. In other words, there is less variability in the R value for low pillar width to pillar height ratios compared to high pillar width to pillar height ratios. When comparing the R values for room convergence and pillar compression, the R values for room convergence were less than the R values for pillar compression for salt thickness of 6 m or larger. This is due to more deformation in the roof and floor of the excavated rooms compared to the deformation in the pillars. In addition, there is less influence of the salt layers on the R values for pillar compression compared to the R values for room convergence.

Figure 38 is applicable to estimating the R value when calculating for the convergence rate of an excavated room; and Figure 29 is applicable to estimating the R values for the compression rate of a pillar. The estimated R value can then be used in the developed

expression of deformation rate. An example of using the developed expression to calculate for pillar compression and room convergence can be found in Appendix C.

7.5 The Effect of Room Width and Excavated Volume on the Convergence Rate

The developed relationship included a pillar width to pillar height ratio parameter, and the results from three sets of pillar dimensions were used in deriving the relationship. In order to assess whether different dimensions of rooms and pillars affect the convergence rate of the pillar, the excavated volume was calculated and plotted against the convergence rate of the pillar and the normalized convergence rate of the pillar. As the room width increased, the pillar height also increased to maintain a constant pillar width to pillar height ratio and a constant extraction ratio. Therefore, the excavated volume increased as the room width increases. Large pillar width to pillar height ratios resulted in short pillar heights where less volume was excavated.

The convergence rate of the pillar increased linearly for all pillar width to pillar height ratios as the excavated volume increased. Figure 39 is an example of the excavated volume plotted against the convergence rate at 0 m of salt thickness; and Figure 40 is an example of the excavated volume plotted against the normalized convergence rate at 0 m of salt thickness. The figures for the remaining salt thicknesses can be found in Appendix D .

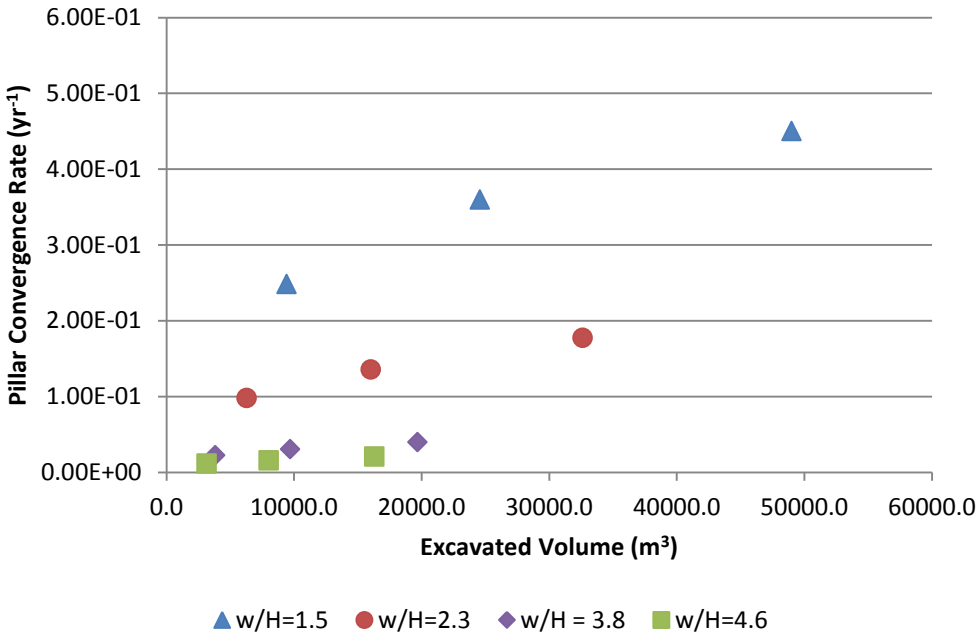

Figure 39. Excavated Volume and Convergence Rate at 0 m of Salt Thickness

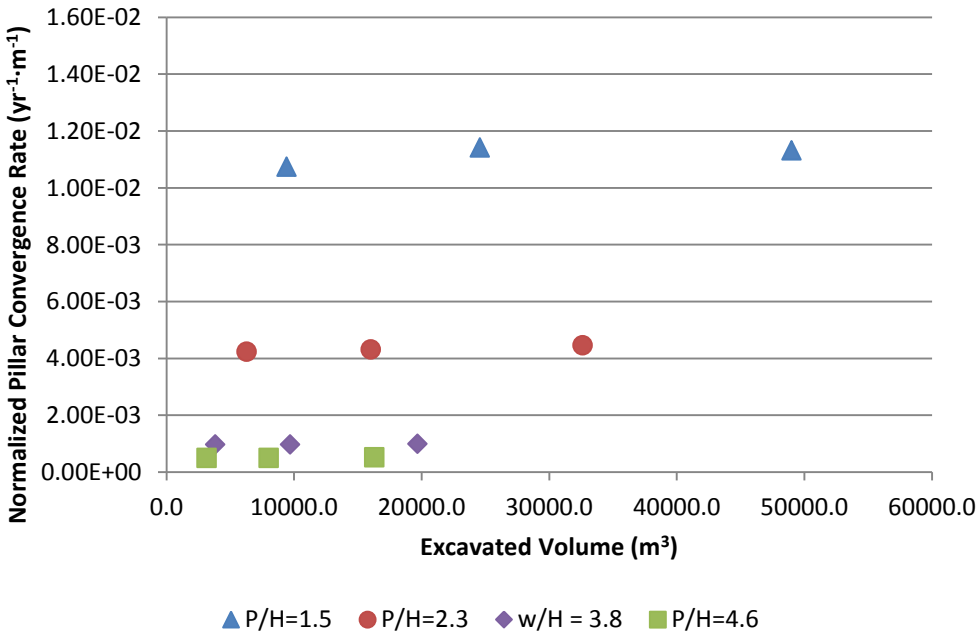

Figure 40. Excavated Volume and Normalized Convergence Rate at 0 m of Salt Thickness

There were three data points for each pillar width to pillar height ratio in Figure 39 and Figure 40 because three sets of pillar and room dimensions were modeled for each ratio at

each salt thickness. There was very little variability in the normalized convergence rate of the pillar for each pillar width to pillar height ratio according to Figure 40. This pattern can be found in all of the salt thicknesses. The normalized convergence rate changed less than 7% for most of the salt thicknesses except for salt thickness of 2 m, 6 m, and 10 m where the convergence rates changed between 7% and 18%. These percentages were calculated by taking the average normalized convergence rate of each pillar width to pillar height ratio, and calculating the percentage difference against this average for the three data points of each pillar width to pillar height ratio.

The common parameter between the salt thicknesses and pillar width to pillar height ratios was a constant extraction ratio of 0.54. As the room width increased, the pillar width to pillar height ratio remained constant which also caused the room width to pillar width ratio to remain constant. In other words, the excavated volume increased, but the normalized convergence rate remained in the same magnitude with low variability. Therefore, the developed empirical relationship did not include a room width variable.

The modeling results from FLAC3D were analyzed and summarized. Trends and patterns were concluded between the salt thickness and the pillar width to pillar height ratio. From observing the parameters of vertical stress, horizontal stress, and convergence rates, it was concluded that FLAC3D was able to model salt pillar behavior correctly. In addition, different room and pillar dimensions with the same pillar width to pillar height ratio resulted in very little variability in the convergence rates.

The relationship between the convergence rate and the salt thickness above and below the pillar was found. This relationship was first developed through the exponential function from the data results. Coefficients and constants were then added to the exponential function account for differences between the exponential function and the data results. The developed relationship predicted the convergence rate of materials governed by the third power law well. However, the developed relationship predicted convergence rates with much larger error for materials governed by the power law with an exponent of four.

Chapter 8 Conclusions

The third power creep law was used in the modeling of a square salt pillar in the finite difference software FLAC3D. A relationship between the convergence rate of rooms and the thickness of the salt roof and salt floor was developed. The developed relationship is composed mainly of two components, the convergence rate for 0 m of salt thickness and the convergence rate for larger than 0 m of salt thickness.

Trends were observed from the modeled results before the developed relationship was finalized. It was found that the convergence rate decreased as the pillar width to pillar height ratio increased. In addition, the convergence rate began to stabilize for salt thicknesses larger than 15 m for the modeled pillar width to pillar height ratios. This is due to the limitations of the stress bulb, where the overbearing capacity affects the stress in the underlying material until a certain depth. Vertical and horizontal stresses were also observed to verify the modeled results reflected actual room and pillar behavior in salt mines. After simulating the model for 20 years, the vertical stresses were the largest in the center of the pillar and near zero at the edges of the pillar. The convergence rate and the pillar width to pillar height ratio exhibited an exponential relationship for all modeled pillar width to pillar height ratios, which was used as the base for the developed relationship between convergence rate and pillar width to pillar height ratio. The convergence rate found from modeling and the convergence rate calculated from the developed relationship showed a strong correlation. The average percentage error between the modeled results and the calculated results was 5.92% for all of the simulations. The percentage error was higher for salt thicknesses larger than 10 m.

The expression for estimating the convergence rate is highly dependent on the R value. Two sets of R values were summarized, where one set describes the behavior for pillar compression and the second set described the room convergence. The R values for the room convergence was generally less than the R values for the pillar compression due to more deformation in rooms compared to pillars.

Chapter 9 Recommendations

There are endless variables that can be modeled and analyzed. A broader range of extraction ratios should be modeled to determine the reason for higher percentage difference for the extraction ratios of 0.40, 0.64, and 0.75. Various pillar width to pillar height ratios should also be modeled for each of the fore mentioned extraction ratios. This may then refine the coefficients, and the developed function will introduce less error.

The developed relationship was concluded from modeling a single pillar. For further verification of the developed relationship, the function should be applied to rectangular pillars of various pillar width to pillar height ratios. Also, the developed relationship should be compared with laboratory data or in-situ measurements.

References

Bachu, S. and Rothenburg, L. (2003). Carbon dioxide sequestration in salt caverns: capacity and long term fate. In Proceedings of NETL Second Annual Conference on Carbon Dioxide Sequestration, Alexandria, VA, May 5-8. Retrieved July 1, 2010, from the Waterloo Institute for Sustainable Energy Website: http://www.wise.uwaterloo.ca/pdf/rothenburg_co2_salt.pdf

Bérest, P., Brouard B., Feuga, B., Karimi.Jafari, M. (2008). The 1873 collapse of the Saint-Maximilien panel at the Varangeville salt mine. *International Journal of Rock Mechanics and Mining Sciences, 45,* 1025-1043.

Carnallite. (n. d.). Retrieved Sept 15, 2010, from http://www.mindat.org/min-906.html

Costa, A.M., Poiate, E.J., Falcão, J. L., and Coelho, L.F.M. (2005). Triaxial creep tests in salt - applied in drilling through thick salt layers in Campos Basin-Brazil. *International Society for Rock Mechanics News Journal, 9(1),* 14-24.

Dusseault, M. B. (2008). Halite – Mechanical behavior and engineering design [PowerPoint slides].

Hansen, F.D., Mellegard, K. D., and Senseny, P. E. (1984). Elasticity and strength of ten natural rock salts. In H. R. Hardy and M. Langer (Eds.), *Proceedings of the First Conference on Mechanical Behavior of Salts*, pp. 71-83. Clausthal: Trans Tech Publications.

Hedley, D.G.F. (1967). An appraisal of convergence measurements in salt mines. In *Proceedings of the 4th Canadian Rock Mechanics Symposium* (pp. 117–35). Ottawa: Mines Branch, Dept. of Mines and Technical Surveys

Hoek, E. (2007). *Practical Rock Engineering 2007* (2007 ed.) Retrieved June 30, 2010, from Rocscience: http://www.rocscience.com/hoek/PracticalRockEngineering.asp

Itasca Consulting Group, Inc. (1997). *FLAC3D Fast Lagrangian Anaylsis of Continua in 3 Dimensions Version 2.0*. Itasca Consulting Group, Inc.: Minneapolis, Minnesota.

Jeramic, M.L. (1994). *Rock Mechanics in Salt Mining*. Rotterdam: A.A. Balkem.

Lajtai, E.Z. and Duncan, E.J. (1988). The Mechanism of Deformation and Fracture in Potash Rock. Final Report for CRD Project 0038997, University of Manitoba, Winnipeg, Manitoba.

Mraz, D.Z. (1972). The theory of flow and its practical application for pillar design in deep potash mines. *Western Miner, April 1972*, 22-26.

Mraz, D.Z. (1973). Behavior of rooms and pillars in deep potash mines. *CIM Bulletin, July 1973*, 60-67.

Munson, D. and Devries, K. (1991). Development and validation of a predictive technology for creep closure of underground rooms in salt, In W. Wittke (ed.), *Proceedings of 7th International Congress on Rock Mechanics (Aachen, September 1991), Vol. 1, ISRM*, pp. 127-134. Rottermdam: A.A. Balkema

Munson, D. (1997). *Creep in rock salt. International Journal of Rock Mechanics and Mining Sciences, 34(2),* 233-247.

Potts, W.H. (1976). Development of a design procedure for a shallow rock salt mine. *CIM Bulletin, January 1976*, 60-67.

Potts, E. L. J. (1964). An Investigation into the Design of Room and Pillar Workings in Rock *Salt. Min Eng (London), No. 49*, pp 27-47.

Rothenburg, L., Frayne, M.A. & Mraz, D.Z. (1993). Application of two and three dimensional numerical models for intact salt rock. In W.F. Bawden & J.F. Archibald (Eds.), *Innovative Mine Design for the 21st Century* (pp. 609-620). Rotterdam: A.A. Balkema.

Rothenburg, L., Dusseault, M.B. & Mraz, D.Z. (2002). On the third-power creep law for salt in mine conditions. In N.D. Cristescu, H.R. Hardy & R.O. Simionescu (Eds.), *Basic and Applied Salt Mechanics: Proceedings of the Fifth Conference on Mechanical Behavior of Salt, MECASALT V: Bucharest, Romania, 9-11 August 1999* (pp. 171-176). Lisse (Netherlands): A.A. Balkema.

Rothenburg, L., Carvalho Jr., ALP, Dusseault, M. B. (2007). Performance of a mining panel over Ttchy-hydrite in Taquari-Vassouras Potash mine. In M. Wallner, K. Lux, W. Minkley, H. R. Hardy, Jr. (Eds.), *The Mechanical Behavior of Salt – Understanding of THMC Processes in Salt Proceedings of the 6th Conference (SaltMech6), Hannover, Germany, 22–25 May 2007* (pp. 305-314). Netherlands: Taylor & Francis Group.

Rothenburg, L. (2010). [PowerPoint slides].

Sylvite. (n. d.). Retrieved Sept 15, 2010, from http://www.mindat.org/min-3850.html

Van Sambeek, L. L.(1997). Salt pillar design equation. In S.S. Peng (Ed.), *16th International Conference on Ground Control in Mining (ICGCM), Morgantown, August 5-7* (Chapter 29).

Wikipedia: The free encyclopedia. (2010, Sept 20). FL: Wikipedia Foundation, Inc. Retrieved September 25, 2010, from http://en.wikipedia.org/wiki/Potash

Wikipedia: The free encyclopedia. (2010, Sept 20). FL: Wikipedia Foundation, Inc. Retrieved September 25, 2010, from http://en.wikipedia.org/wiki/Carnallite

Wikipedia: The free encyclopedia. (2010, Sept 20). FL: Wikipedia Foundation, Inc. Retrieved September 25, 2010, from http://en.wikipedia.org/wiki/Sylvite

Appendix A

Convergence Rates of Location 2

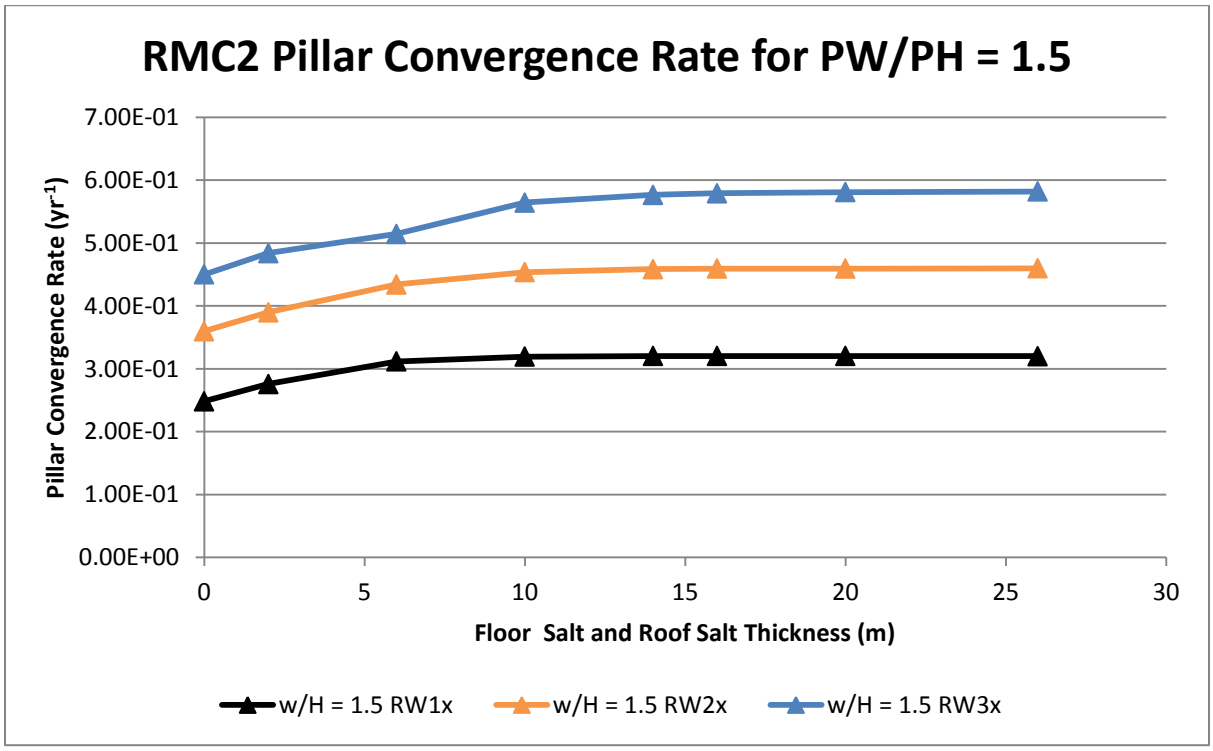
RMC2 Pillar Convergence Rate for PW/PH = 1.5
Pillar Convergence Rate (yr-1)
7.00E-01
6.00E-01
5.00E-01
4.00E-01
3.00E-01
2.00E-01
1.00E-01
0.00E+00
0
5
10
15
20
25
30
Floor Salt and Roof Salt Thickness (m)
w/H = 1.5 RW1x
w/H = 1.5 RW2x
w/H = 1.5 RW3x

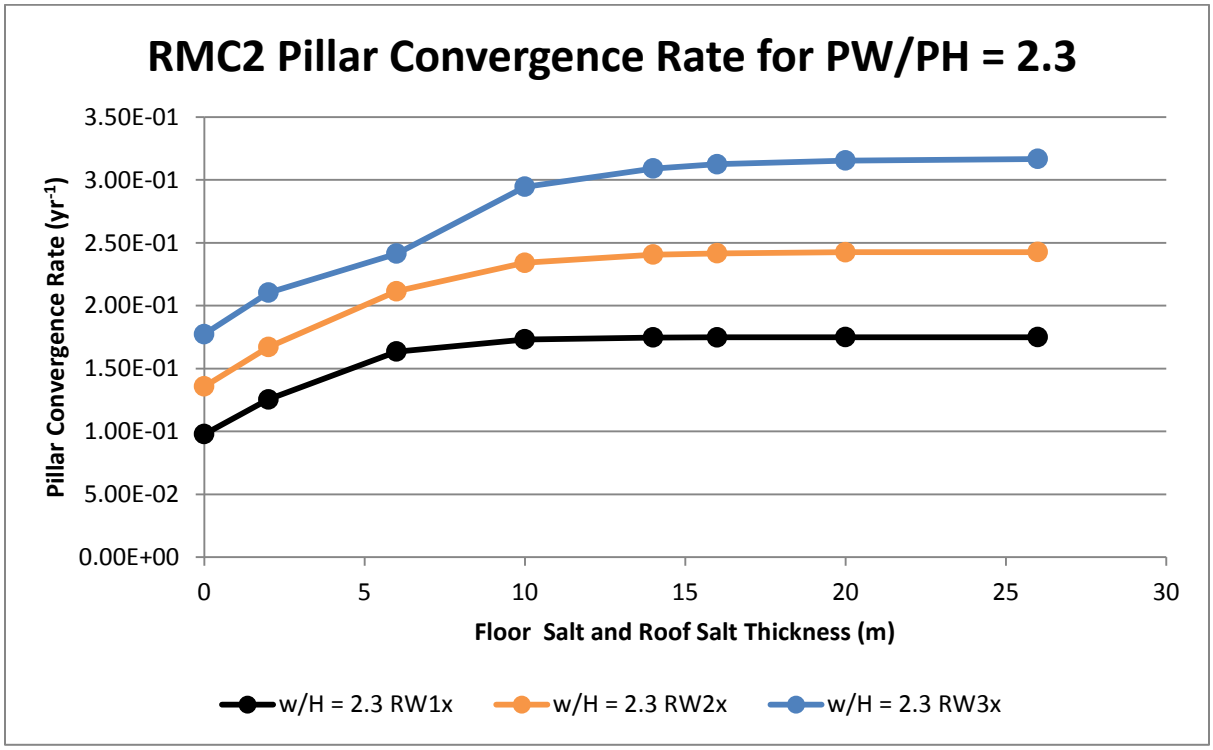
RMC2 Pillar Convergence Rate for PW/PH = 2.3
Pillar Convergence Rate (yr-1)
3.50E-01
3.00E-01
2.50E-01
2.00E-01
1.50E-01
1.00E-01
5.00E-02
0.00E+00
0
5
10
15
20
25
30
Floor Salt and Roof Salt Thickness (m)
w/H = 2.3 RW1x
w/H = 2.3 RW2x
w/H = 2.3 RW3x

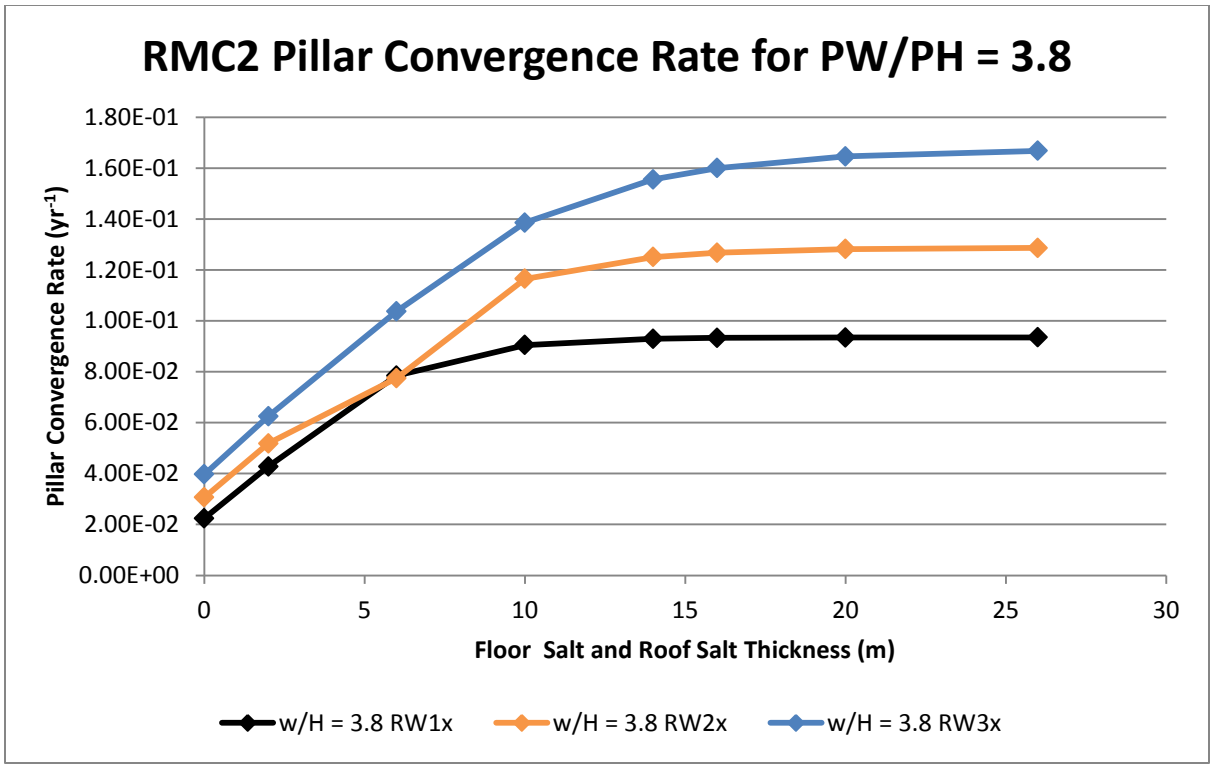
RMC2 Pillar Convergence Rate for PW/PH = 3.8
Pillar Convergence Rate (yr-1)
1.80E-01
1.60E-01
1.40E-01
1.20E-01
1.00E-01
8.00E-02
6.00E-02
4.00E-02
2.00E-02
0.00E+00
0
5
10
15
20
25
30
Floor Salt and Roof Salt Thickness (m)
w/H = 3.8 RW1x
w/H = 3.8 RW2x
w/H = 3.8 RW3x

Appendix B

Pillar Behavior Graphs (R value and Vertical Stress)

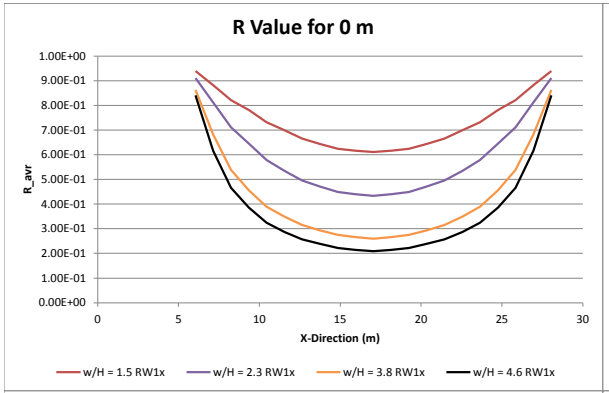
R Value for 0 m
R_avr
X-Direction (m)
w/H = 1.5 RW1x
w/H = 2.3 RW1x
w/H = 3.8 RW1x
w/H = 4.6 RW1x

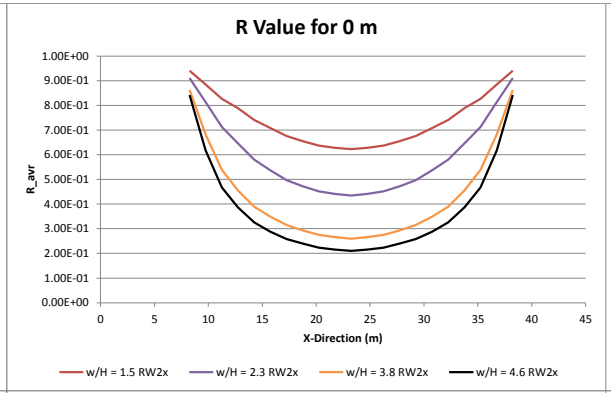
R Value for 0 m
R_avr
X-Direction (m)
w/H = 1.5 RW2x
w/H = 2.3 RW2x
w/H = 3.8 RW2x
w/H = 4.6 RW2x

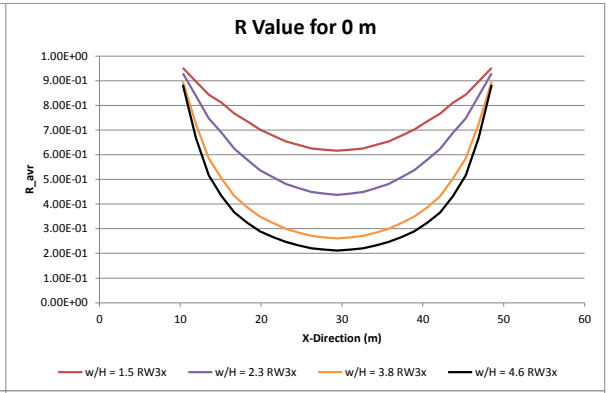
R Value for 0 m
R_avr
X-Direction (m)
w/H = 1.5 RW3x
w/H = 2.3 RW3x
w/H = 3.8 RW3x
w/H = 4.6 RW3x

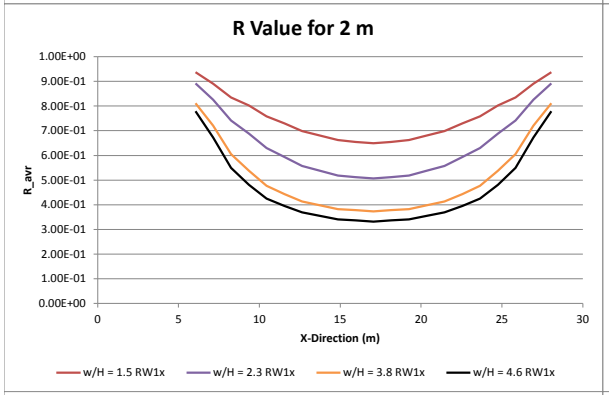
R Value for 2 m
R_avr
X-Direction (m)
w/H = 1.5 RW1x
w/H = 2.3 RW1x
w/H = 3.8 RW1x
w/H = 4.6 RW1x

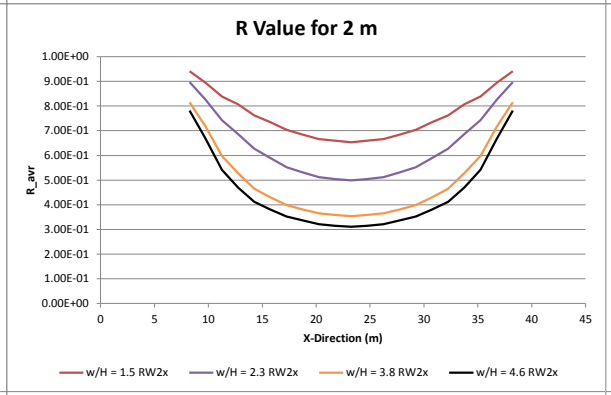
R Value for 2 m
R_avr
X-Direction (m)
w/H = 1.5 RW2x
w/H = 2.3 RW2x
w/H = 3.8 RW2x
w/H = 4.6 RW2x

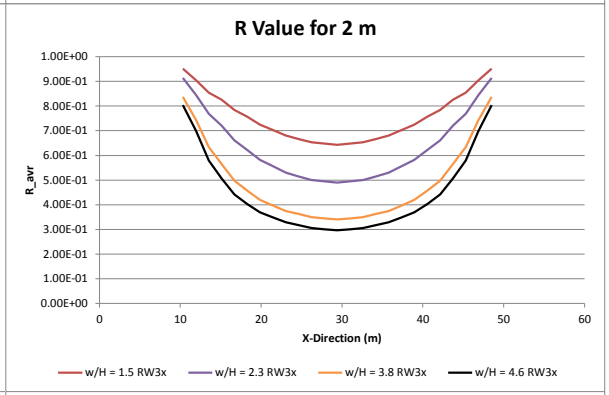
R Value for 2 m
R_avr
X-Direction (m)
w/H = 1.5 RW3x
w/H = 2.3 RW3x
w/H = 3.8 RW3x
w/H = 4.6 RW3x

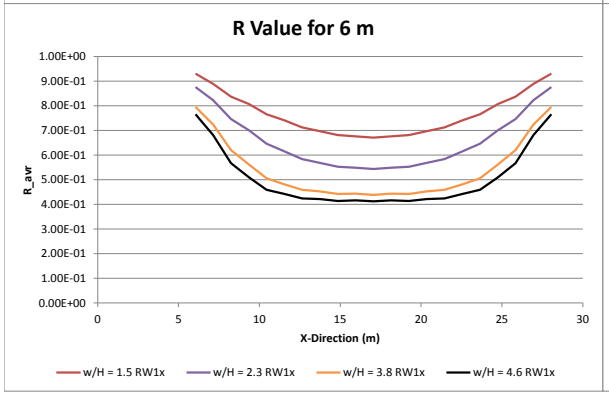
R Value for 6 m
R_avr
X-Direction (m)
w/H = 1.5 RW1x
w/H = 2.3 RW1x
w/H = 3.8 RW1x
w/H = 4.6 RW1x

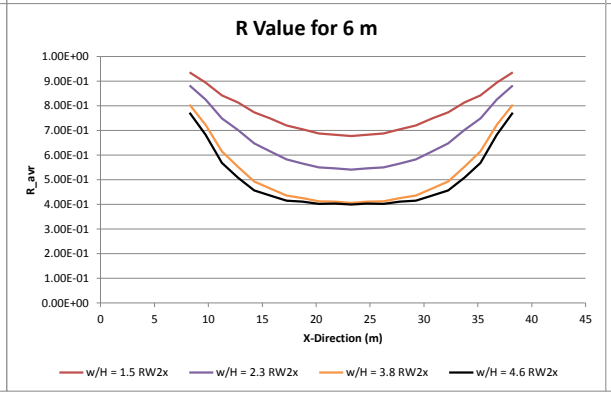
R Value for 6 m
R_avr
X-Direction (m)
w/H = 1.5 RW2x
w/H = 2.3 RW2x
w/H = 3.8 RW2x
w/H = 4.6 RW2x

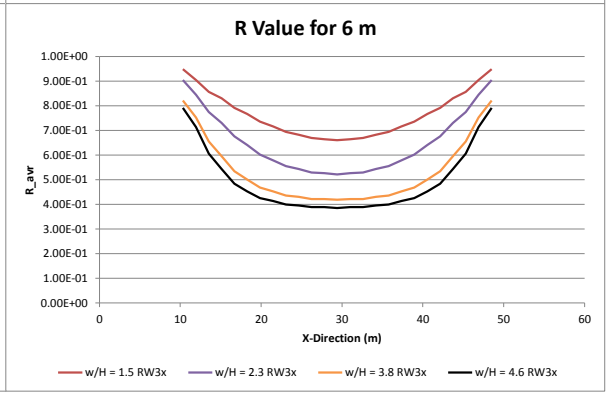
R Value for 6 m
R_avr
X-Direction (m)
w/H = 1.5 RW3x
w/H = 2.3 RW3x
w/H = 3.8 RW3x
w/H = 4.6 RW3x

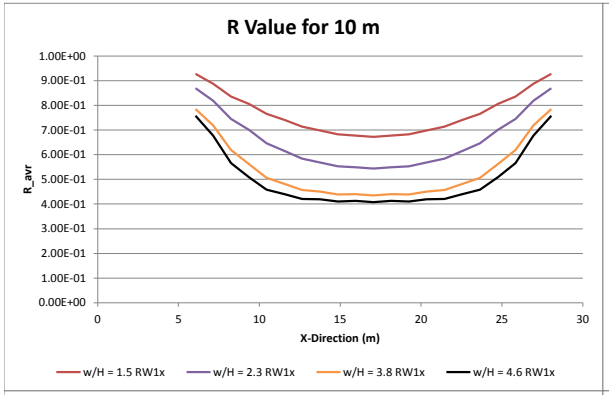
R Value for 10 m
R_avr
X-Direction (m)
w/H = 1.5 RW1x
w/H = 2.3 RW1x
w/H = 3.8 RW1x
w/H = 4.6 RW1x

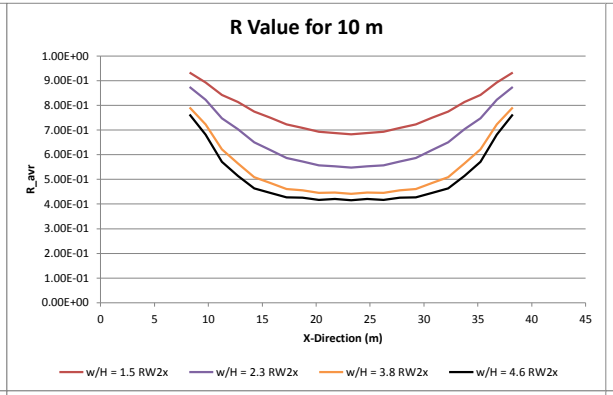
R Value for 10 m
R_avr
X-Direction (m)
w/H = 1.5 RW2x
w/H = 2.3 RW2x
w/H = 3.8 RW2x
w/H = 4.6 RW2x

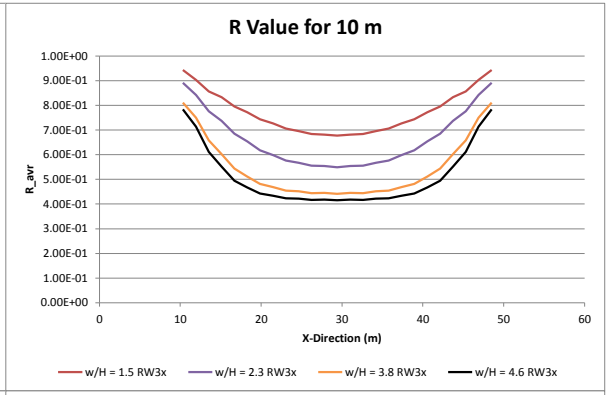
R Value for 10 m
R_avr
X-Direction (m)
w/H = 1.5 RW3x
w/H = 2.3 RW3x
w/H = 3.8 RW3x
w/H = 4.6 RW3x

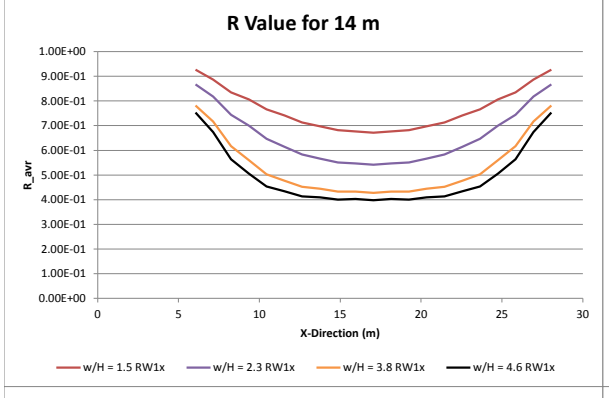
R Value for 14 m
R_avr
X-Direction (m)
w/H = 1.5 RW1x
w/H = 2.3 RW1x
w/H = 3.8 RW1x
w/H = 4.6 RW1x

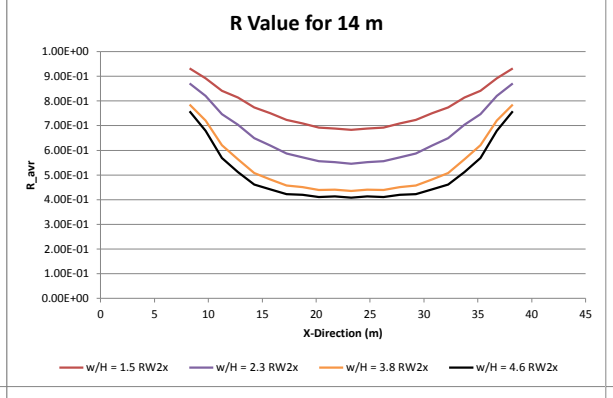
R Value for 14 m
R_avr
X-Direction (m)
w/H = 1.5 RW2x
w/H = 2.3 RW2x
w/H = 3.8 RW2x
w/H = 4.6 RW2x

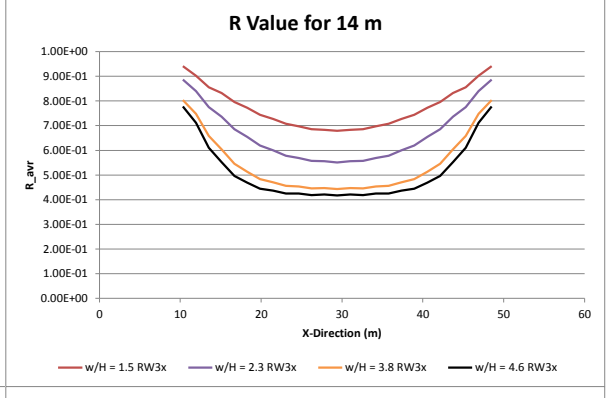
R Value for 14 m
R_avr
X-Direction (m)
w/H = 1.5 RW3x
w/H = 2.3 RW3x
w/H = 3.8 RW3x
w/H = 4.6 RW3x

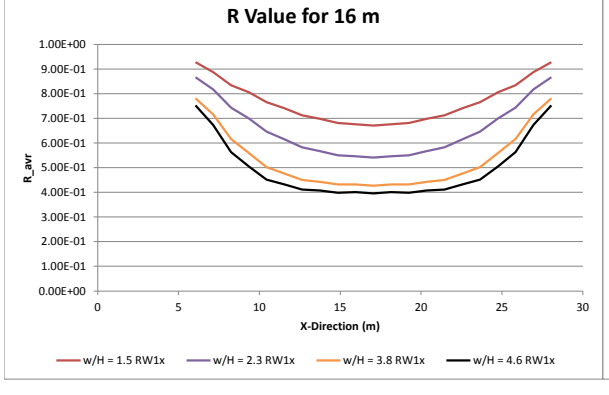
R Value for 16 m
R_avr
X-Direction (m)
w/H = 1.5 RW1x
w/H = 2.3 RW1x
w/H = 3.8 RW1x
w/H = 4.6 RW1x

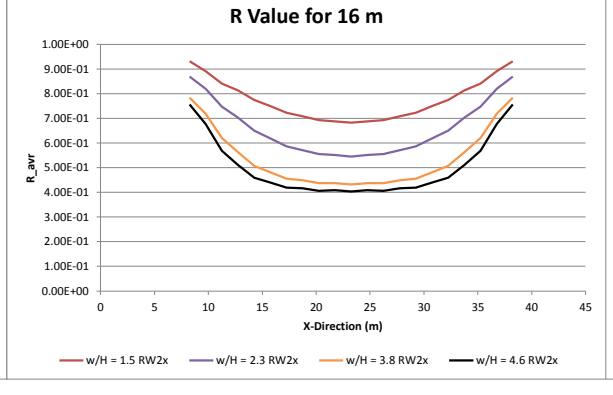
R Value for 16 m
R_avr
X-Direction (m)
w/H = 1.5 RW2x
w/H = 2.3 RW2x
w/H = 3.8 RW2x
w/H = 4.6 RW2x

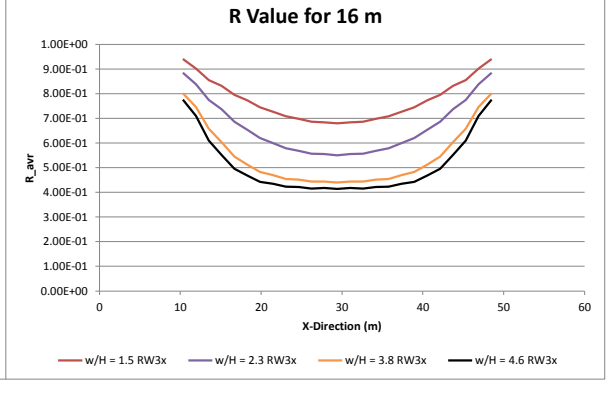
R Value for 16 m
R_avr
X-Direction (m)
w/H = 1.5 RW3x
w/H = 2.3 RW3x
w/H = 3.8 RW3x
w/H = 4.6 RW3x

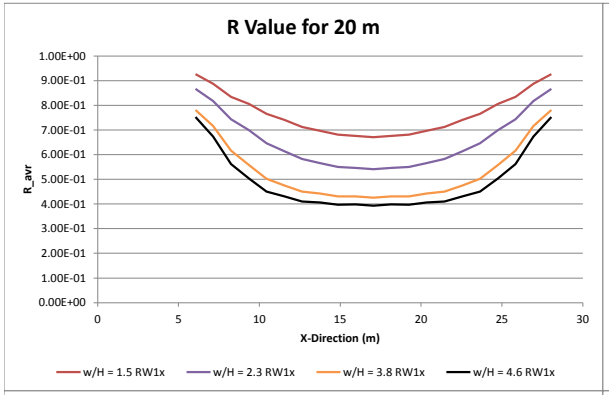
R Value for 20 m
R_avr
X-Direction (m)
w/H = 1.5 RW1x
w/H = 2.3 RW1x
w/H = 3.8 RW1x
w/H = 4.6 RW1x

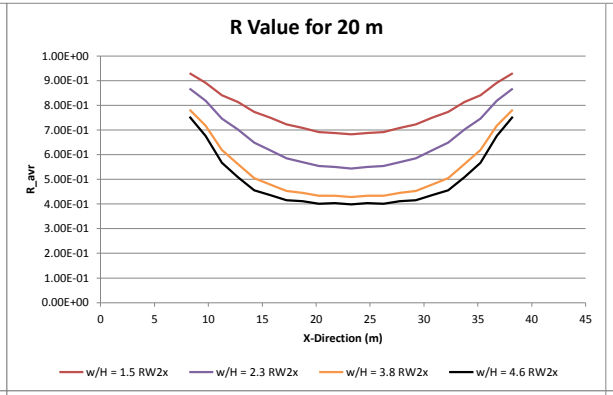
R Value for 20 m
R_avr
X-Direction (m)
w/H = 1.5 RW2x
w/H = 2.3 RW2x
w/H = 3.8 RW2x
w/H = 4.6 RW2x

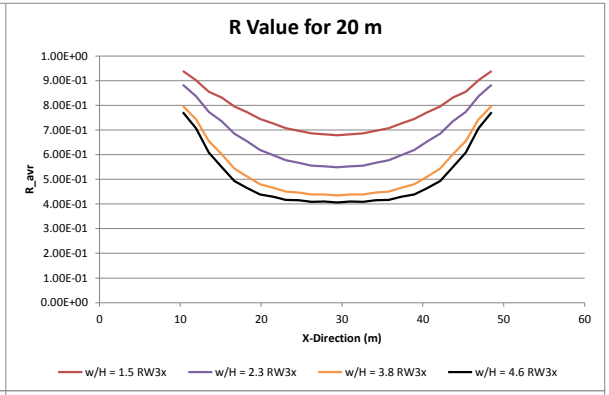
R Value for 20 m
R_avr
X-Direction (m)
w/H = 1.5 RW3x
w/H = 2.3 RW3x
w/H = 3.8 RW3x
w/H = 4.6 RW3x

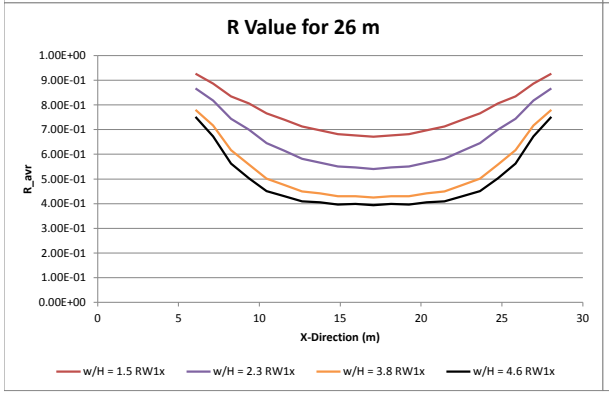
R Value for 26 m
R_avr
X-Direction (m)
w/H = 1.5 RW1x
w/H = 2.3 RW1x
w/H = 3.8 RW1x
w/H = 4.6 RW1x

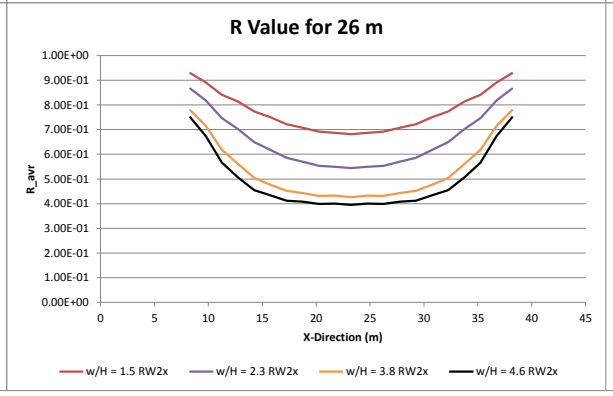
R Value for 26 m
R_avr
X-Direction (m)
w/H = 1.5 RW2x
w/H = 2.3 RW2x
w/H = 3.8 RW2x
w/H = 4.6 RW2x

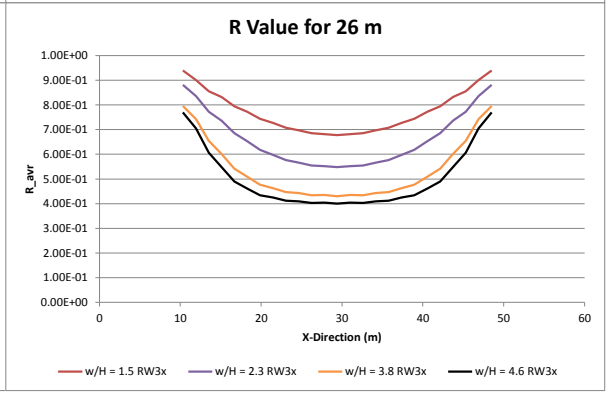
R Value for 26 m
R_avr
X-Direction (m)
w/H = 1.5 RW3x
w/H = 2.3 RW3x
w/H = 3.8 RW3x
w/H = 4.6 RW3x

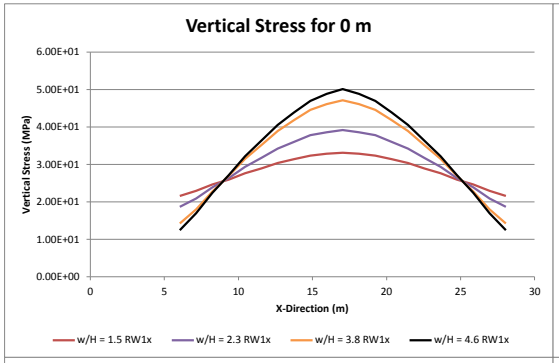
Vertical Stress for 0 m
Vertical Stress (MPa)
X-Direction (m)
w/H = 1.5 RW1x
w/H = 2.3 RW1x
w/H = 3.8 RW1x
w/H = 4.6 RW1x

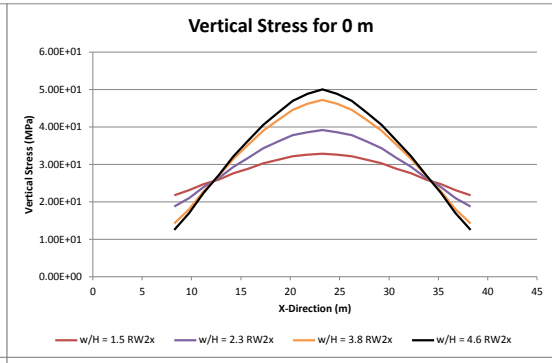
Vertical Stress for 0 m
Vertical Stress (MPa)
X-Direction (m)
w/H = 1.5 RW2x
w/H = 2.3 RW2x
w/H = 3.8 RW2x
w/H = 4.6 RW2x

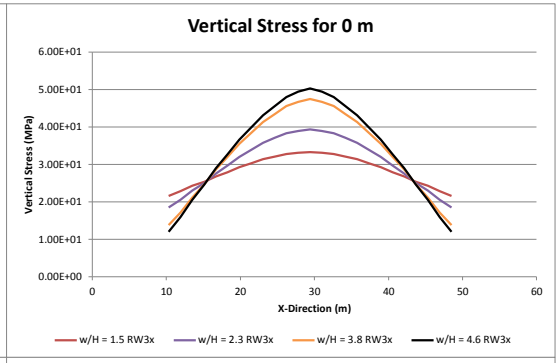
Vertical Stress for 0 m
Vertical Stress (MPa)
X-Direction (m)
w/H = 1.5 RW3x
w/H = 2.3 RW3x
w/H = 3.8 RW3x
w/H = 4.6 RW3x

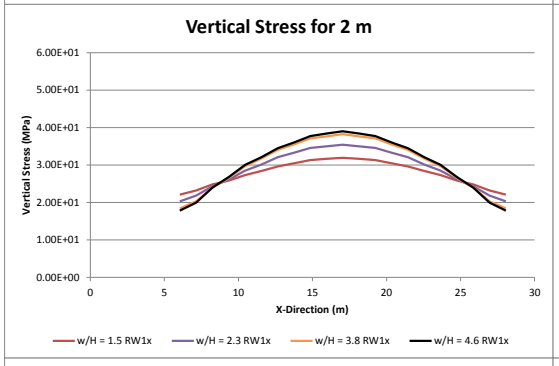
Vertical Stress for 2 m
Vertical Stress (MPa)
X-Direction (m)
w/H = 1.5 RW1x
w/H = 2.3 RW1x
w/H = 3.8 RW1x
w/H = 4.6 RW1x

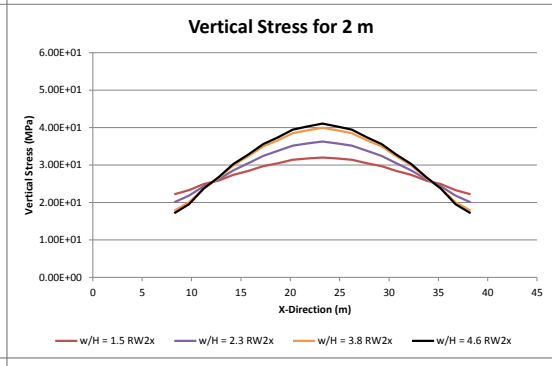
Vertical Stress for 2 m
Vertical Stress (MPa)
X-Direction (m)
w/H = 1.5 RW2x
w/H = 2.3 RW2x
w/H = 3.8 RW2x
w/H = 4.6 RW2x

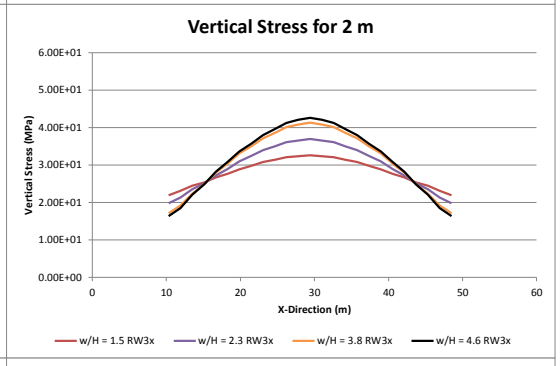
Vertical Stress for 2 m
Vertical Stress (MPa)
X-Direction (m)
w/H = 1.5 RW3x
w/H = 2.3 RW3x
w/H = 3.8 RW3x
w/H = 4.6 RW3x

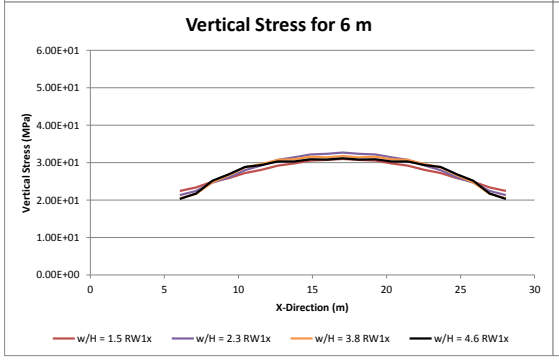
Vertical Stress for 6 m
Vertical Stress (MPa)
X-Direction (m)
w/H = 1.5 RW1x
w/H = 2.3 RW1x
w/H = 3.8 RW1x
w/H = 4.6 RW1x

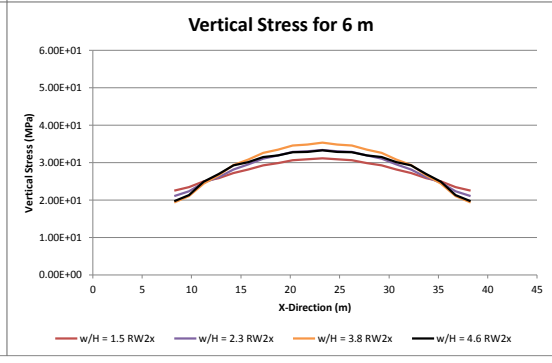
Vertical Stress for 6 m
Vertical Stress (MPa)
X-Direction (m)
w/H = 1.5 RW2x
w/H = 2.3 RW2x
w/H = 3.8 RW2x
w/H = 4.6 RW2x

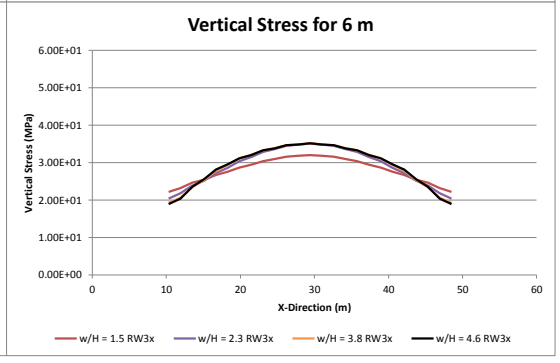
Vertical Stress for 6 m
Vertical Stress (MPa)
X-Direction (m)
w/H = 1.5 RW3x
w/H = 2.3 RW3x
w/H = 3.8 RW3x
w/H = 4.6 RW3x

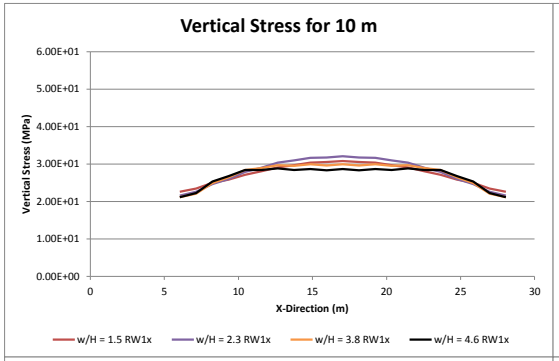
Vertical Stress for 10 m
Vertical Stress (MPa)
6.00E+01
5.00E+01
4.00E+01
3.00E+01
2.00E+01
1.00E+01
0.00E+00
0
5
10
15
20
25
30
X-Direction (m)
w/H = 1.5 RW1x
w/H = 2.3 RW1x
w/H = 3.8 RW1x
w/H = 4.6 RW1x

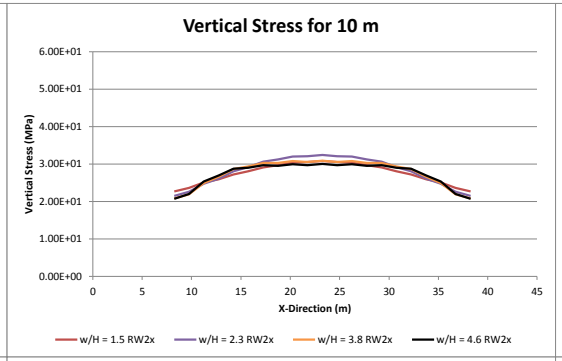
Vertical Stress for 10 m
Vertical Stress (MPa)
6.00E+01
5.00E+01
4.00E+01
3.00E+01
2.00E+01
1.00E+01
0.00E+00
0
5
10
15
20
25
30
35
40
45
X-Direction (m)
w/H = 1.5 RW2x
w/H = 2.3 RW2x
w/H = 3.8 RW2x
w/H = 4.6 RW2x

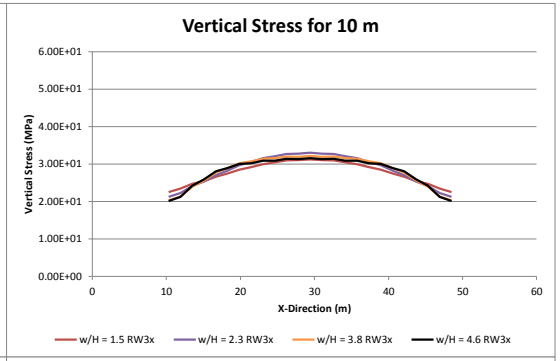
Vertical Stress for 10 m
Vertical Stress (MPa)
6.00E+01
5.00E+01
4.00E+01
3.00E+01
2.00E+01
1.00E+01
0.00E+00
0
10
20
30
40
50
60
X-Direction (m)
w/H = 1.5 RW3x
w/H = 2.3 RW3x
w/H = 3.8 RW3x
w/H = 4.6 RW3x

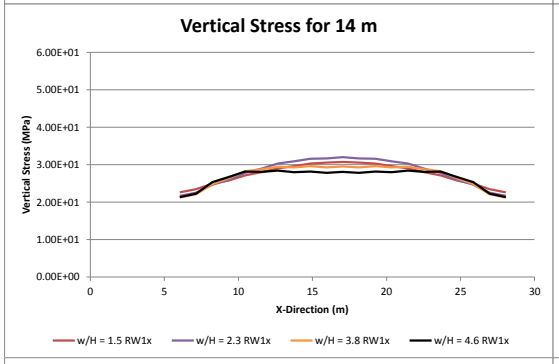
Vertical Stress for 14 m
Vertical Stress (MPa)
6.00E+01
5.00E+01
4.00E+01
3.00E+01
2.00E+01
1.00E+01
0.00E+00
0
5
10
15
20
25
30
X-Direction (m)
w/H = 1.5 RW1x
w/H = 2.3 RW1x
w/H = 3.8 RW1x
w/H = 4.6 RW1x

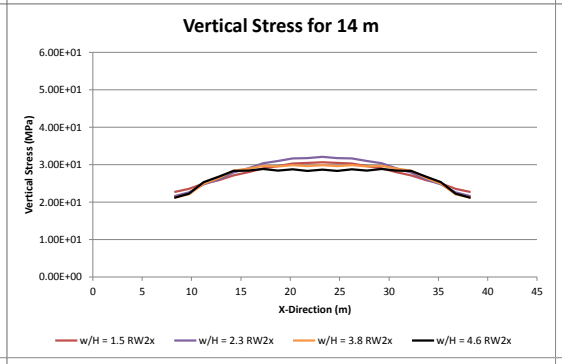
Vertical Stress for 14 m
Vertical Stress (MPa)
6.00E+01
5.00E+01
4.00E+01
3.00E+01
2.00E+01
1.00E+01
0.00E+00
0
5
10
15
20
25
30
35
40
45
X-Direction (m)
w/H = 1.5 RW2x
w/H = 2.3 RW2x
w/H = 3.8 RW2x
w/H = 4.6 RW2x

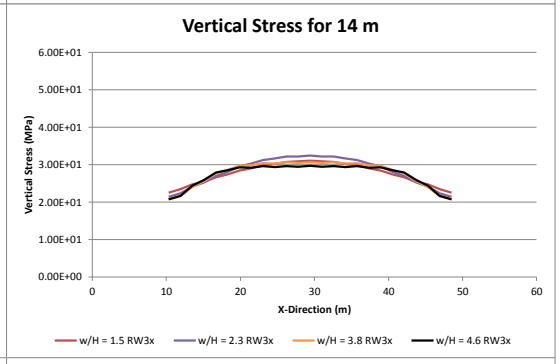
Vertical Stress for 14 m
Vertical Stress (MPa)
6.00E+01
5.00E+01
4.00E+01
3.00E+01
2.00E+01
1.00E+01
0.00E+00
0
10
20
30
40
50
60
X-Direction (m)
w/H = 1.5 RW3x
w/H = 2.3 RW3x
w/H = 3.8 RW3x
w/H = 4.6 RW3x

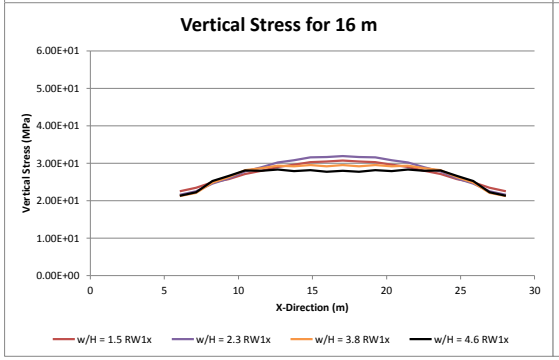
Vertical Stress for 16 m
Vertical Stress (MPa)
6.00E+01
5.00E+01
4.00E+01
3.00E+01
2.00E+01
1.00E+01
0.00E+00
0
5
10
15
20
25
30
X-Direction (m)
w/H = 1.5 RW1x
w/H = 2.3 RW1x
w/H = 3.8 RW1x
w/H = 4.6 RW1x

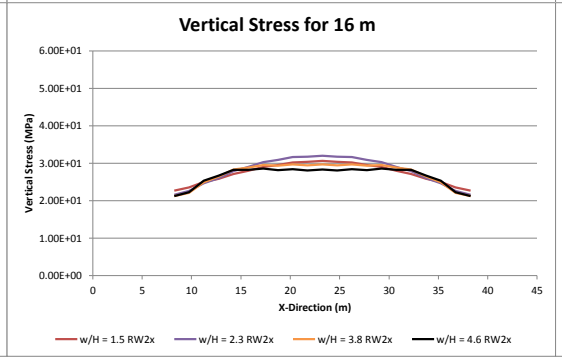
Vertical Stress for 16 m
Vertical Stress (MPa)
6.00E+01
5.00E+01
4.00E+01
3.00E+01
2.00E+01
1.00E+01
0.00E+00
0
5
10
15
20
25
30
35
40
45
X-Direction (m)
w/H = 1.5 RW2x
w/H = 2.3 RW2x
w/H = 3.8 RW2x
w/H = 4.6 RW2x

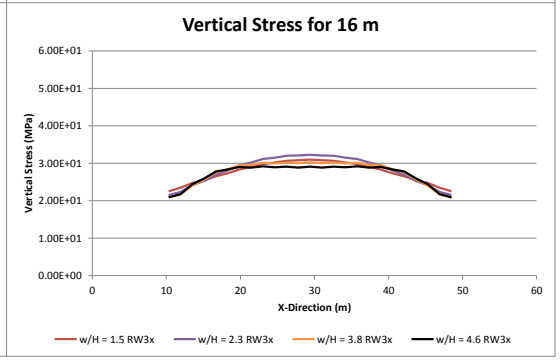
Vertical Stress for 16 m
Vertical Stress (MPa)
6.00E+01
5.00E+01
4.00E+01
3.00E+01
2.00E+01
1.00E+01
0.00E+00
0
10
20
30
40
50
60
X-Direction (m)
w/H = 1.5 RW3x
w/H = 2.3 RW3x
w/H = 3.8 RW3x
w/H = 4.6 RW3x

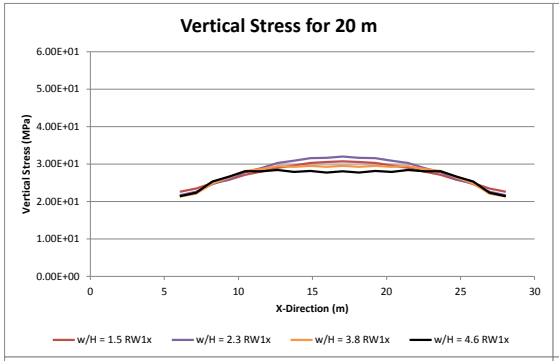
Vertical Stress for 20 m
Vertical Stress (MPa)
6.00E+01
5.00E+01
4.00E+01
3.00E+01
2.00E+01
1.00E+01
0.00E+00
0
5
10
15
20
25
30
X-Direction (m)
w/H = 1.5 RW1x
w/H = 2.3 RW1x
w/H = 3.8 RW1x
w/H = 4.6 RW1x

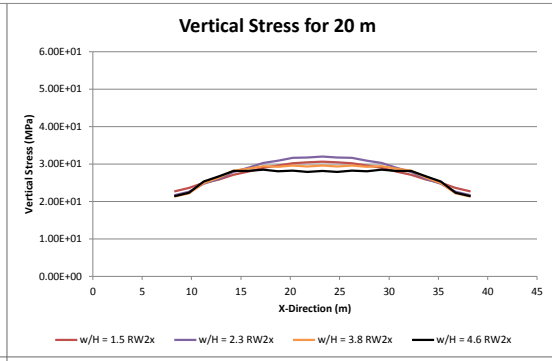
Vertical Stress for 20 m
Vertical Stress (MPa)
6.00E+01
5.00E+01
4.00E+01
3.00E+01
2.00E+01
1.00E+01
0.00E+00
0
5
10
15
20
25
30
35
40
45
X-Direction (m)
w/H = 1.5 RW2x
w/H = 2.3 RW2x
w/H = 3.8 RW2x
w/H = 4.6 RW2x

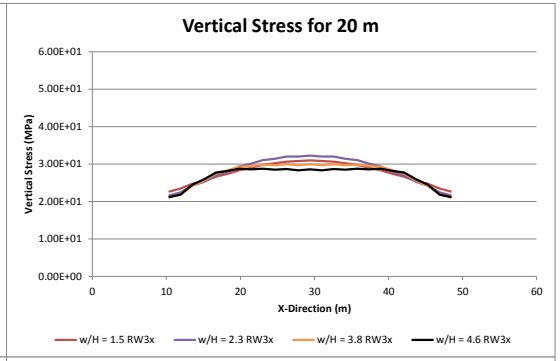
Vertical Stress for 20 m
Vertical Stress (MPa)
6.00E+01
5.00E+01
4.00E+01
3.00E+01
2.00E+01
1.00E+01
0.00E+00
0
10
20
30
40
50
60
X-Direction (m)
w/H = 1.5 RW3x
w/H = 2.3 RW3x
w/H = 3.8 RW3x
w/H = 4.6 RW3x

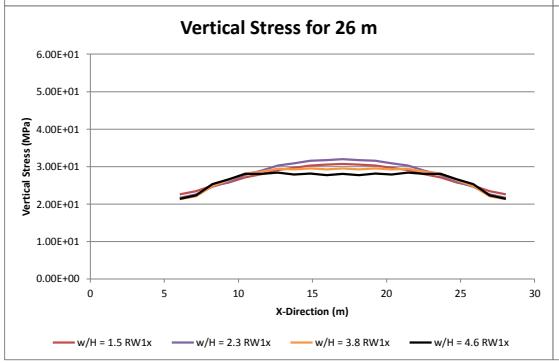
Vertical Stress for 26 m
Vertical Stress (MPa)
6.00E+01
5.00E+01
4.00E+01
3.00E+01
2.00E+01
1.00E+01
0.00E+00
0
5
10
15
20
25
30
X-Direction (m)
w/H = 1.5 RW1x
w/H = 2.3 RW1x
w/H = 3.8 RW1x
w/H = 4.6 RW1x

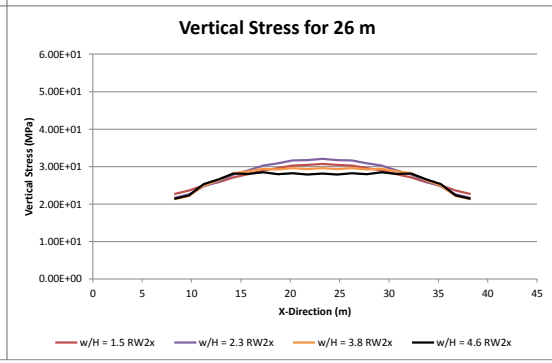
Vertical Stress for 26 m
Vertical Stress (MPa)
6.00E+01
5.00E+01
4.00E+01
3.00E+01
2.00E+01
1.00E+01
0.00E+00
0
5
10
15
20
25
30
35
40
45
X-Direction (m)
w/H = 1.5 RW2x
w/H = 2.3 RW2x
w/H = 3.8 RW2x
w/H = 4.6 RW2x

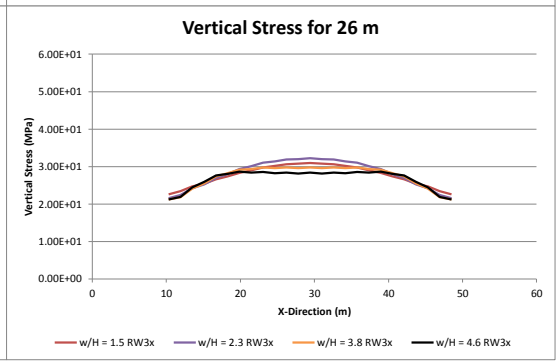
Vertical Stress for 26 m
Vertical Stress (MPa)
6.00E+01
5.00E+01
4.00E+01
3.00E+01
2.00E+01
1.00E+01
0.00E+00
0
10
20
30
40
50
60
X-Direction (m)
w/H = 1.5 RW3x
w/H = 2.3 RW3x
w/H = 3.8 RW3x
w/H = 4.6 RW3x

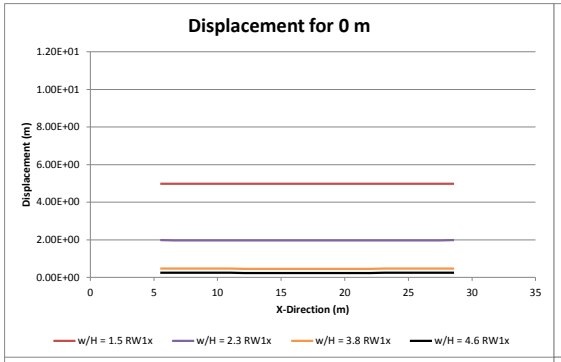
Displacement for 0 m
Displacement (m)
X-Direction (m)
w/H = 1.5 RW1x
w/H = 2.3 RW1x
w/H = 3.8 RW1x
w/H = 4.6 RW1x

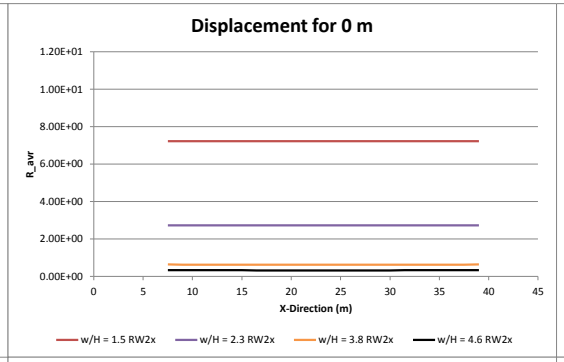
Displacement for 0 m
R_avr
X-Direction (m)
w/H = 1.5 RW2x
w/H = 2.3 RW2x
w/H = 3.8 RW2x
w/H = 4.6 RW2x

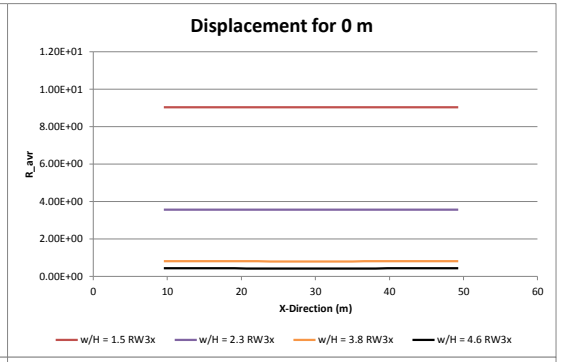
Displacement for 0 m
R_avr
X-Direction (m)
w/H = 1.5 RW3x
w/H = 2.3 RW3x
w/H = 3.8 RW3x
w/H = 4.6 RW3x

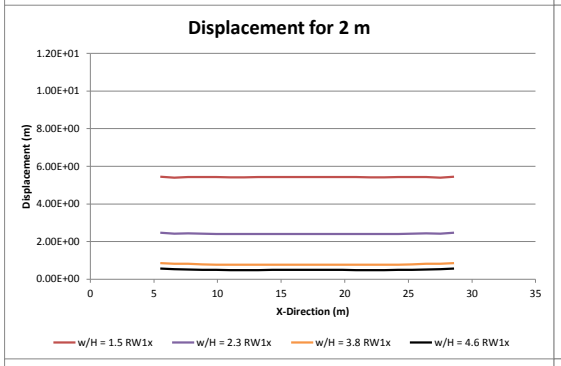
Displacement for 2 m
Displacement (m)
X-Direction (m)
w/H = 1.5 RW1x
w/H = 2.3 RW1x
w/H = 3.8 RW1x
w/H = 4.6 RW1x

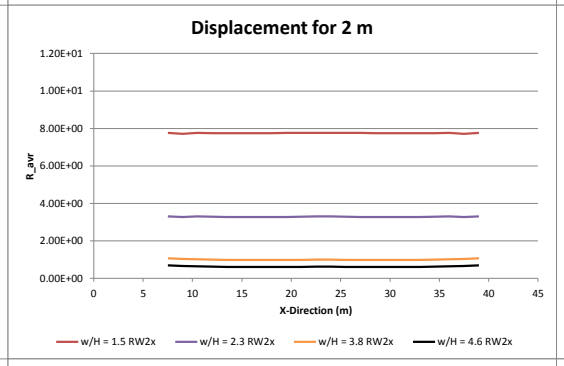
Displacement for 2 m
R_avr
X-Direction (m)
w/H = 1.5 RW2x
w/H = 2.3 RW2x
w/H = 3.8 RW2x
w/H = 4.6 RW2x

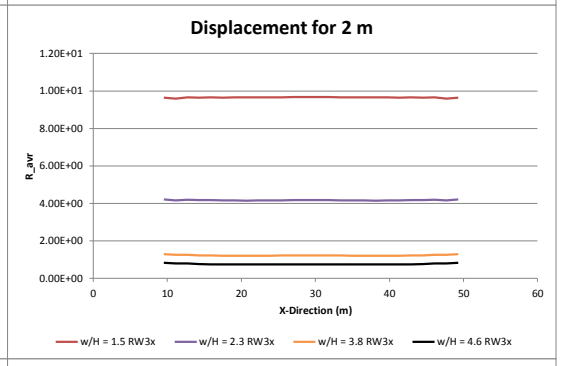
Displacement for 2 m
R_avr
X-Direction (m)
w/H = 1.5 RW3x
w/H = 2.3 RW3x
w/H = 3.8 RW3x
w/H = 4.6 RW3x

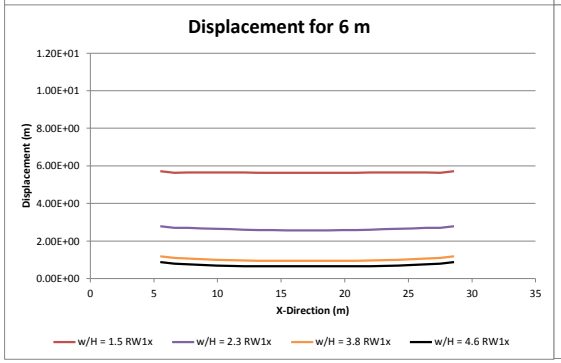
Displacement for 6 m
Displacement (m)
X-Direction (m)
w/H = 1.5 RW1x
w/H = 2.3 RW1x
w/H = 3.8 RW1x
w/H = 4.6 RW1x

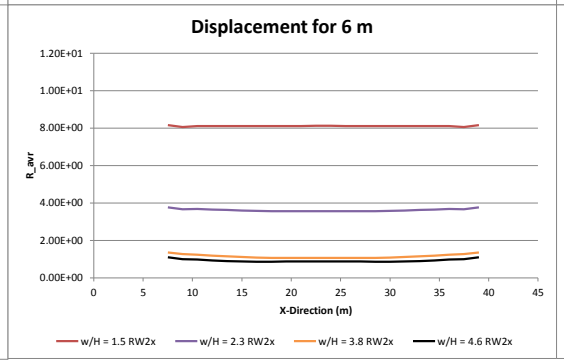
Displacement for 6 m
R_avr
X-Direction (m)
w/H = 1.5 RW2x
w/H = 2.3 RW2x
w/H = 3.8 RW2x
w/H = 4.6 RW2x

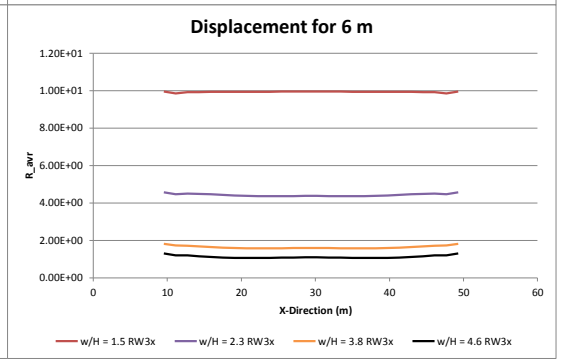
Displacement for 6 m
R_avr
X-Direction (m)
w/H = 1.5 RW3x
w/H = 2.3 RW3x
w/H = 3.8 RW3x
w/H = 4.6 RW3x

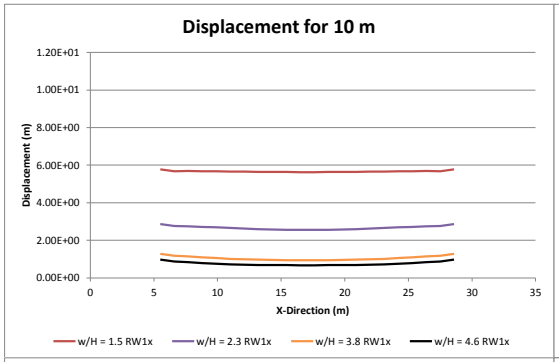
Displacement for 10 m
Displacement (m)
X-Direction (m)
w/H = 1.5 RW1x
w/H = 2.3 RW1x
w/H = 3.8 RW1x
w/H = 4.6 RW1x

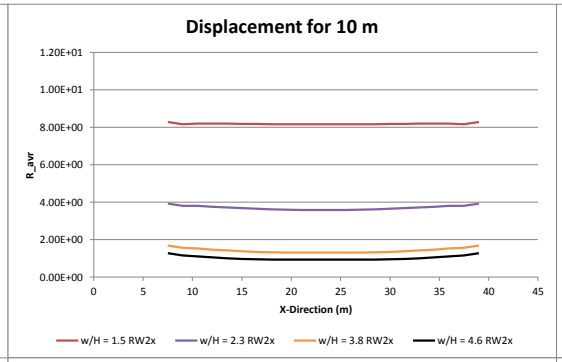
Displacement for 10 m
R_avr
X-Direction (m)
w/H = 1.5 RW2x
w/H = 2.3 RW2x
w/H = 3.8 RW2x
w/H = 4.6 RW2x

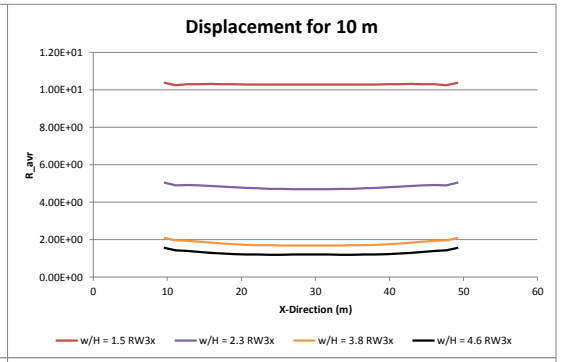
Displacement for 10 m
R_avr
X-Direction (m)
w/H = 1.5 RW3x
w/H = 2.3 RW3x
w/H = 3.8 RW3x
w/H = 4.6 RW3x

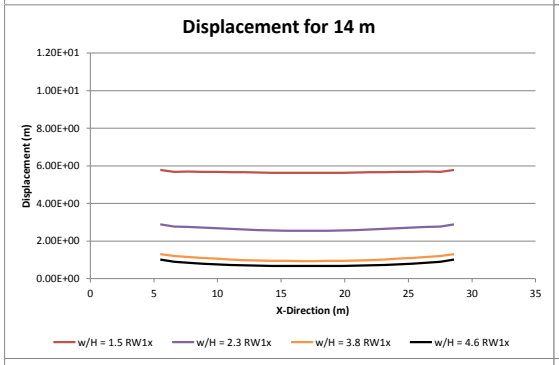
Displacement for 14 m
Displacement (m)
X-Direction (m)
w/H = 1.5 RW1x
w/H = 2.3 RW1x
w/H = 3.8 RW1x
w/H = 4.6 RW1x

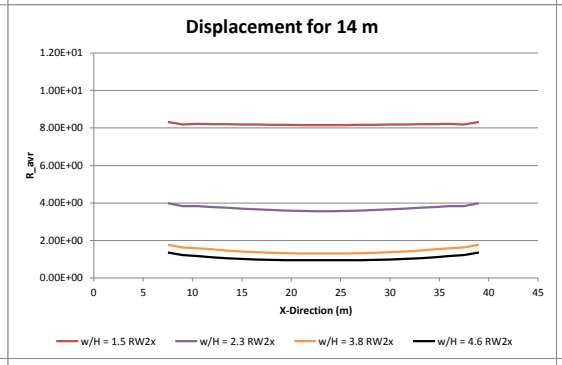
Displacement for 14 m
R_avr
X-Direction (m)
w/H = 1.5 RW2x
w/H = 2.3 RW2x
w/H = 3.8 RW2x
w/H = 4.6 RW2x

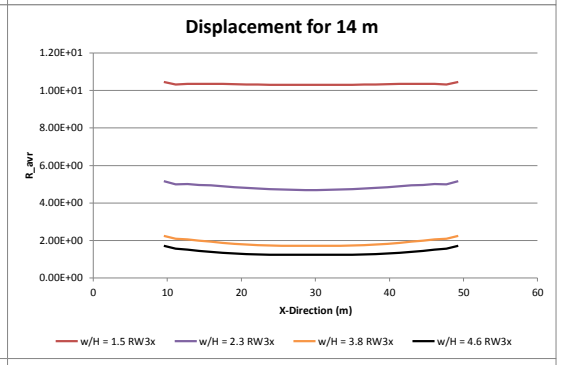
Displacement for 14 m
R_avr
X-Direction (m)
w/H = 1.5 RW3x
w/H = 2.3 RW3x
w/H = 3.8 RW3x
w/H = 4.6 RW3x

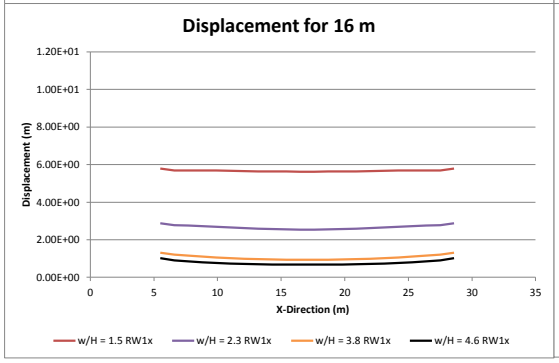
Displacement for 16 m
Displacement (m)
X-Direction (m)
w/H = 1.5 RW1x
w/H = 2.3 RW1x
w/H = 3.8 RW1x
w/H = 4.6 RW1x

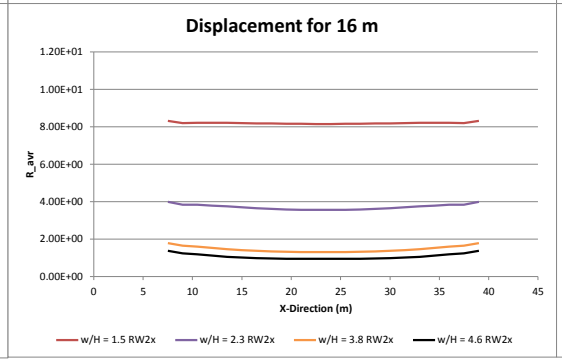
Displacement for 16 m
R_avr
X-Direction (m)
w/H = 1.5 RW2x
w/H = 2.3 RW2x
w/H = 3.8 RW2x
w/H = 4.6 RW2x

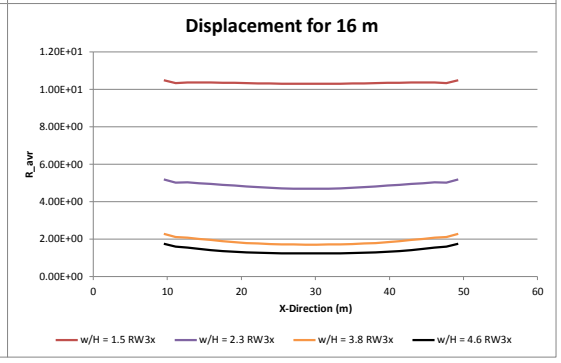
Displacement for 16 m
R_avr
X-Direction (m)
w/H = 1.5 RW3x
w/H = 2.3 RW3x
w/H = 3.8 RW3x
w/H = 4.6 RW3x

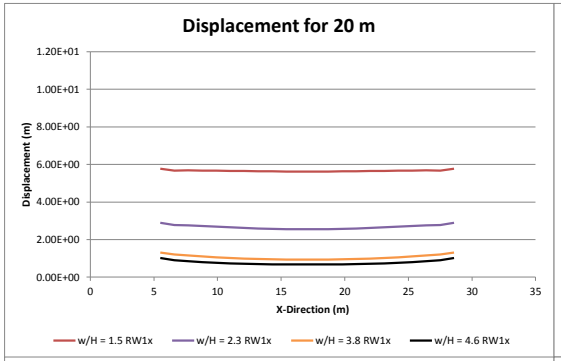
Displacement for 20 m
Displacement (m)
X-Direction (m)
w/H = 1.5 RW1x
w/H = 2.3 RW1x
w/H = 3.8 RW1x
w/H = 4.6 RW1x

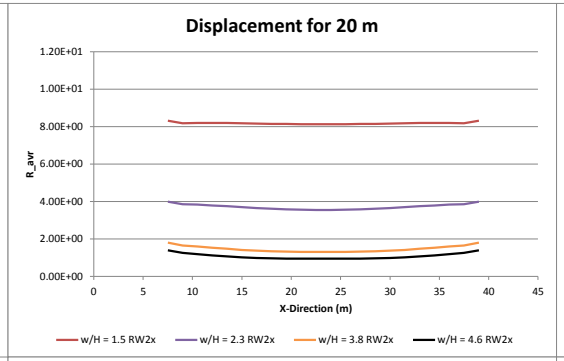
Displacement for 20 m
R_avr
X-Direction (m)
w/H = 1.5 RW2x
w/H = 2.3 RW2x
w/H = 3.8 RW2x
w/H = 4.6 RW2x

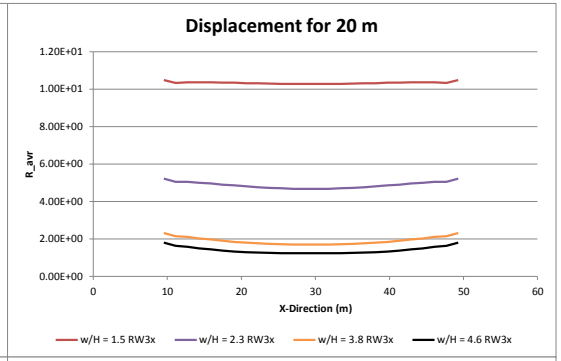
Displacement for 20 m
R_avr
X-Direction (m)
w/H = 1.5 RW3x
w/H = 2.3 RW3x
w/H = 3.8 RW3x
w/H = 4.6 RW3x

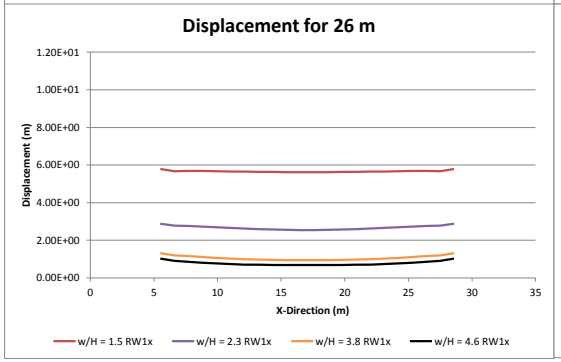
Displacement for 26 m
Displacement (m)
X-Direction (m)
w/H = 1.5 RW1x
w/H = 2.3 RW1x
w/H = 3.8 RW1x
w/H = 4.6 RW1x

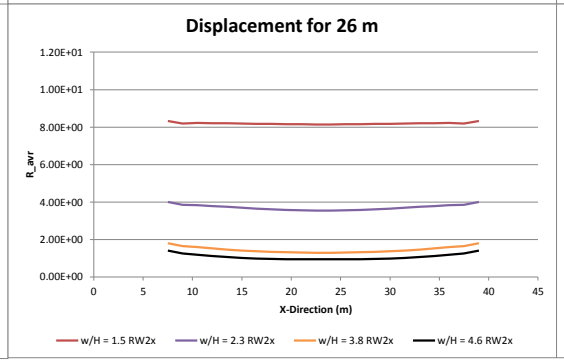
Displacement for 26 m
R_avr
X-Direction (m)
w/H = 1.5 RW2x
w/H = 2.3 RW2x
w/H = 3.8 RW2x
w/H = 4.6 RW2x

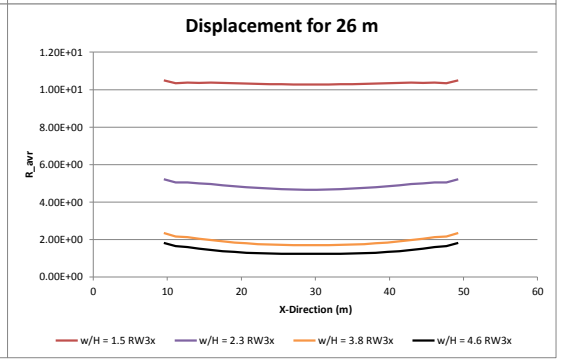
Displacement for 26 m
R_avr
X-Direction (m)
w/H = 1.5 RW3x
w/H = 2.3 RW3x
w/H = 3.8 RW3x
w/H = 4.6 RW3x

Appendix C

An example of using the developed expression to calculate for pillar compression and room convergence

The calculations for determining the pillar compression and the room convergence from the given dimensions are shown in this section. An example of pillar dimensions is a pillar height of 5 m, a pillar width of 11.5 m with 30 m of salt above and below the pillar, and using an extraction ratio of 0.54.

Given: H = 5 m

W/H = 2.3

T = 30 m

$\dot{\varepsilon}$ = 0.002

$\bar{\sigma}$ = 25 MPa

σ_0 = 10 MPa

Looking up the R value from Figure 25, the R value for pillar compression is 7.34×10^{-1}.

The pillar compression rate is calculated using the following relationship:

$$\dot{\varepsilon} = \dot{\varepsilon}_0 H (R\frac{\bar{\sigma}}{\sigma_0})^3$$

The pillar compression rate is then 0.06 m/yr.

The room convergence rate is calculated using the same relationship as the relationship for calculating pillar compression. For a salt thickness of 30 m, function f_1 from Section 7.4 was calculated and resulted in the R value of 0.84. The following are sample calculations using the developed expressions explained in Section 7.4.

$$\alpha\left(\frac{W}{H}\right) = -0.0052\left(\frac{W}{H}\right) + 0.1365$$

$$\alpha(2.3) = -0.0052(2.3) + 0.1365$$

$$\alpha(2.3) = 0.1245$$

$$f_1(T) = 0.1027 \times (1 - e^{-\alpha T})$$

$$f_1(30) = 0.1027 \times (1 - e^{-0.1245\times30})$$

$$f_1(30) = 0.1003$$

$$f_2\left(\frac{W}{H}\right) = 1.828 \times e^{-1.072\times\frac{W}{H}}$$

$$f_2(2.3) = 1.828 \times e^{-1.072\times2.3}$$

$f_2(2.3) = 0.1553$

$$R = \sqrt[3]{\frac{W}{H} \times (f_1 + f_2)}$$

$$R = \sqrt[3]{2.3 \times (0.1003 + 0.1553)}$$

$$R = 0.8377$$

Using the calculated R value of 0.84 and the developed expression, the room convergence rate was calculated to be 0.092 m/yr. The room convergence rate is larger than the pillar compression rate. This corresponds to the reasoning that there is more deformation in the excavated rooms compared to the amount of deformation in the pillar.

Appendix D

Convergence Rates for Various Excavated Volumes

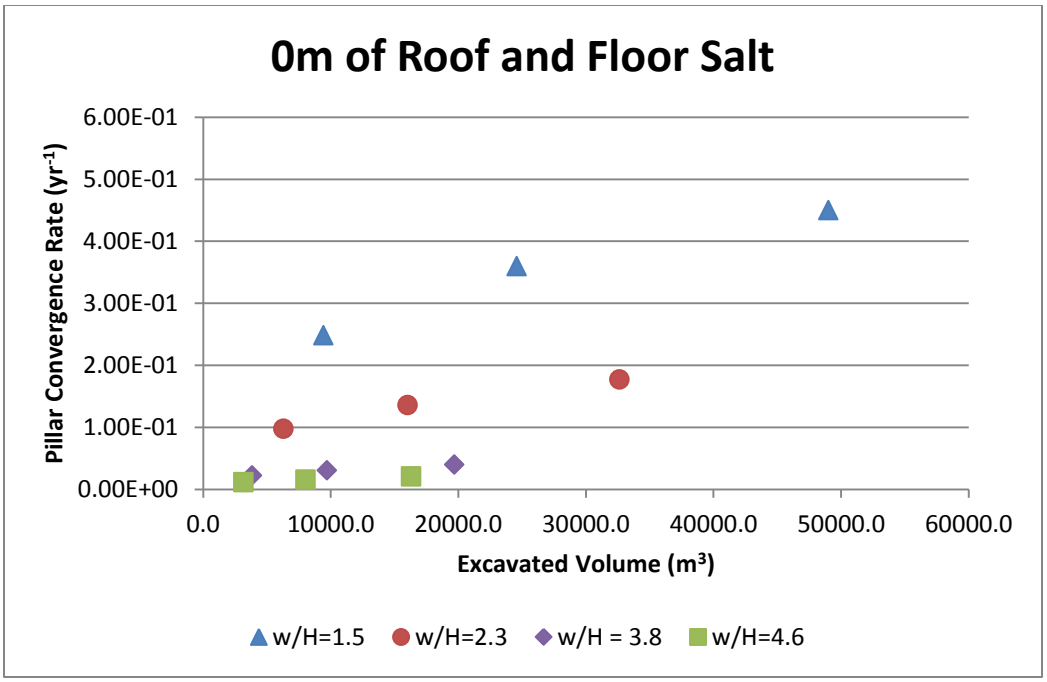
0m of Roof and Floor Salt
Pillar Convergence Rate (yr-1)
6.00E-01
5.00E-01
4.00E-01
3.00E-01
2.00E-01
1.00E-01
0.00E+00
0.0
10000.0
20000.0
30000.0
40000.0
50000.0
60000.0
Excavated Volume (m3)
w/H=1.5
w/H=2.3
w/H = 3.8
w/H=4.6

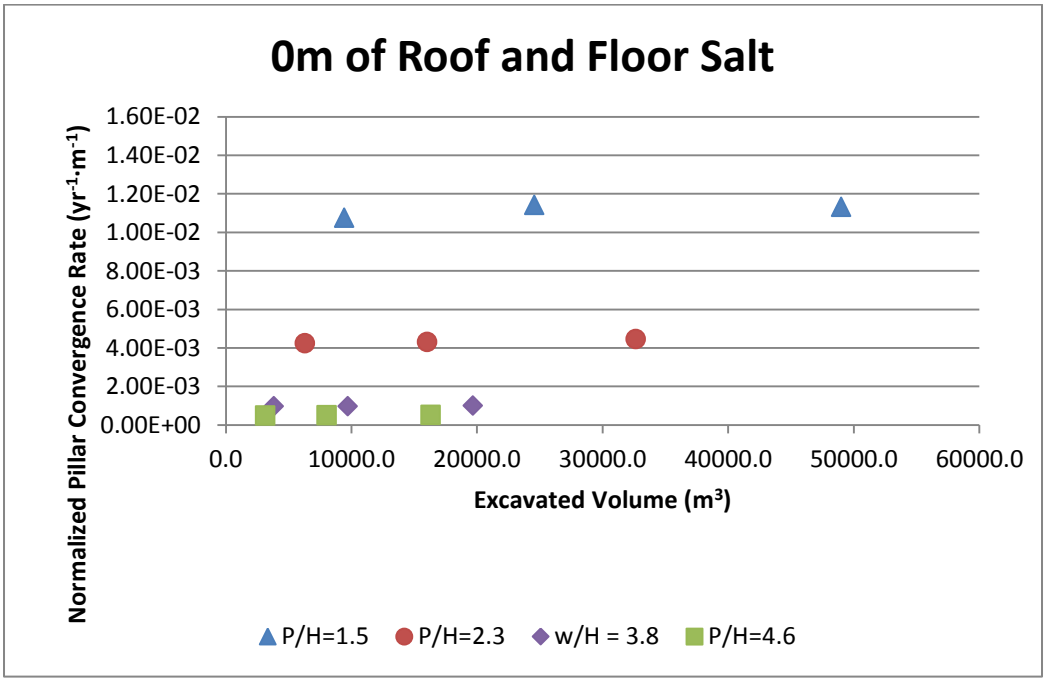
0m of Roof and Floor Salt
Normalized Pillar Convergence Rate (yr-1·m-1)
1.60E-02
1.40E-02
1.20E-02
1.00E-02
8.00E-03
6.00E-03
4.00E-03
2.00E-03
0.00E+00
0.0
10000.0
20000.0
30000.0
40000.0
50000.0
60000.0
Excavated Volume (m3)
P/H=1.5
P/H=2.3
w/H = 3.8
P/H=4.6

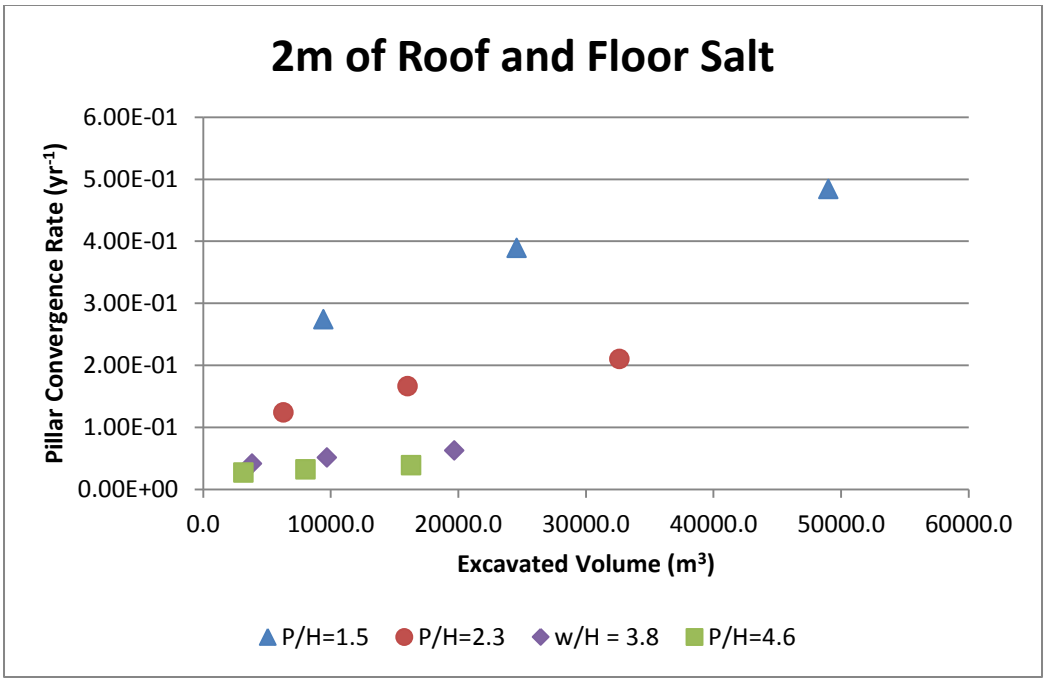
2m of Roof and Floor Salt
Pillar Convergence Rate (yr-1)
6.00E-01
5.00E-01
4.00E-01
3.00E-01
2.00E-01
1.00E-01
0.00E+00
0.0
10000.0
20000.0
30000.0
40000.0
50000.0
60000.0
Excavated Volume (m3)
P/H=1.5
P/H=2.3
w/H = 3.8
P/H=4.6

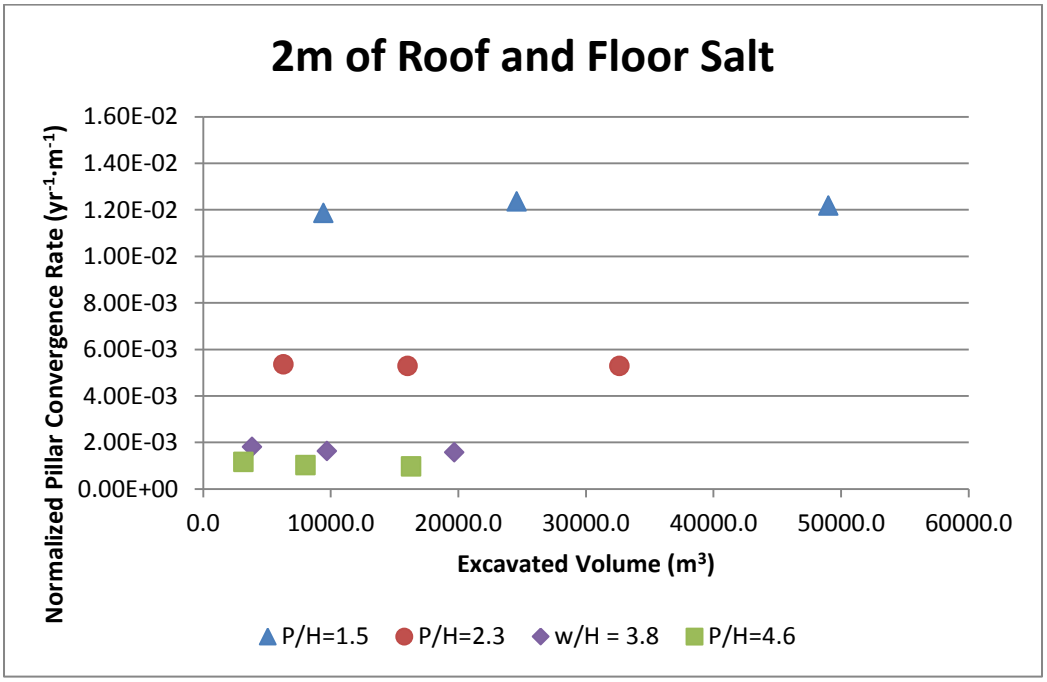
2m of Roof and Floor Salt
Normalized Pillar Convergence Rate (yr-1-m-1)
1.60E-02
1.40E-02
1.20E-02
1.00E-02
8.00E-03
6.00E-03
4.00E-03
2.00E-03
0.00E+00
0.0
10000.0
20000.0
30000.0
40000.0
50000.0
60000.0
Excavated Volume (m3)
P/H=1.5
P/H=2.3
w/H = 3.8
P/H=4.6

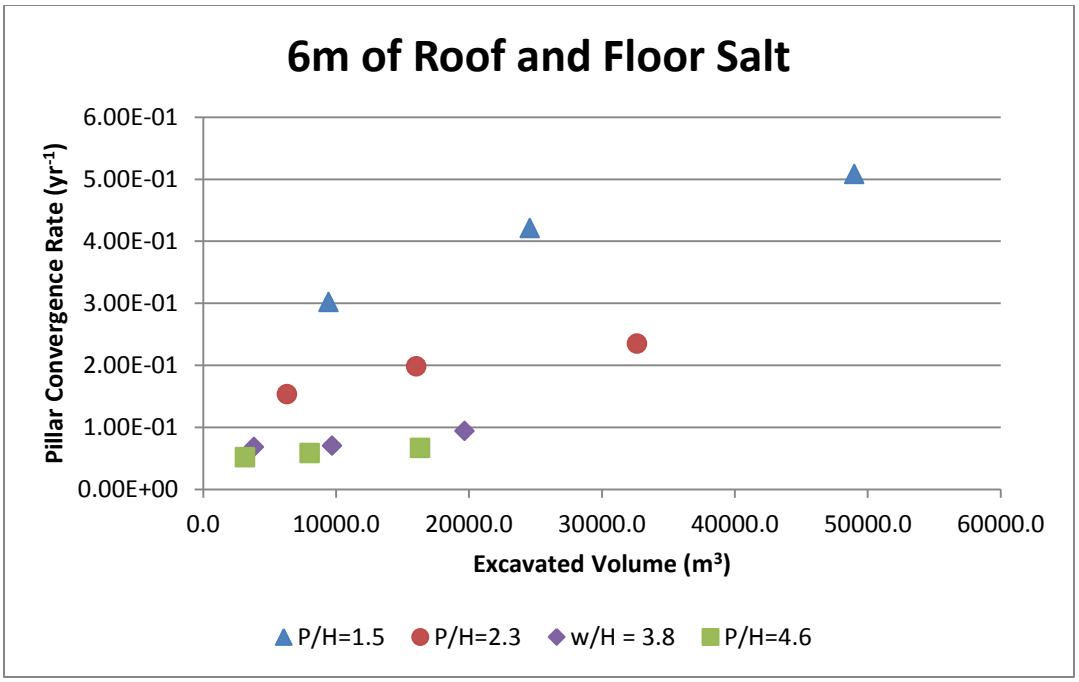
6m of Roof and Floor Salt
Pillar Convergence Rate (yr-1)
6.00E-01
5.00E-01
4.00E-01
3.00E-01
2.00E-01
1.00E-01
0.00E+00
0.0
10000.0
20000.0
30000.0
40000.0
50000.0
60000.0
Excavated Volume (m3)
P/H=1.5
P/H=2.3
w/H = 3.8
P/H=4.6

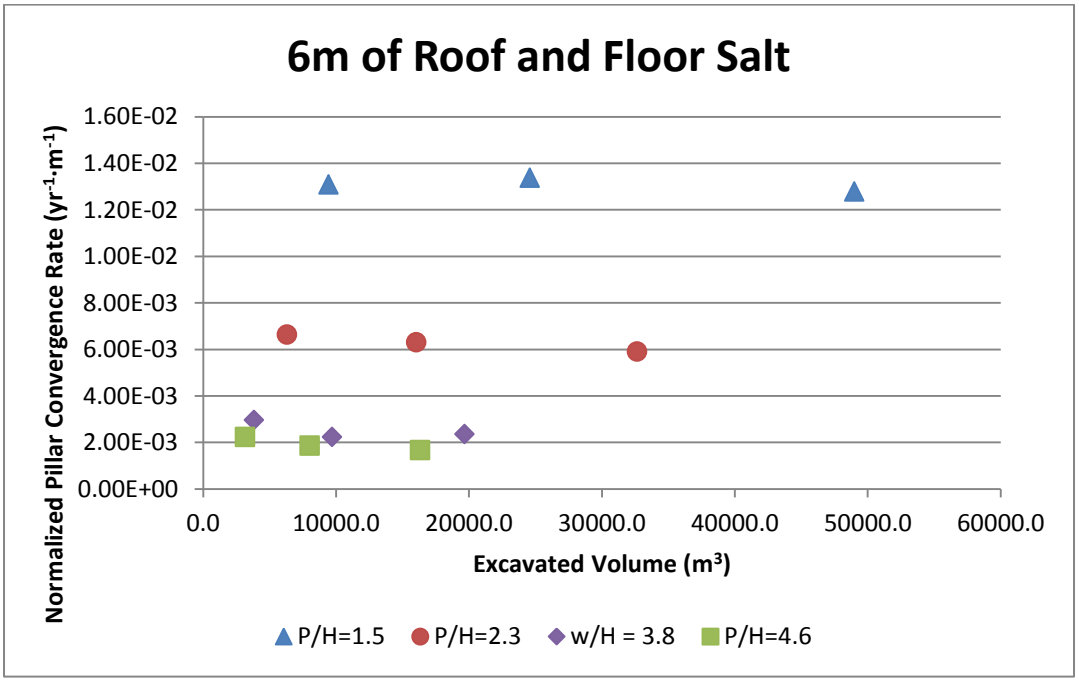
6m of Roof and Floor Salt
Normalized Pillar Convergence Rate (yr-1·m-1)
1.60E-02
1.40E-02
1.20E-02
1.00E-02
8.00E-03
6.00E-03
4.00E-03
2.00E-03
0.00E+00
0.0
10000.0
20000.0
30000.0
40000.0
50000.0
60000.0
Excavated Volume (m3)
P/H=1.5
P/H=2.3
w/H = 3.8
P/H=4.6

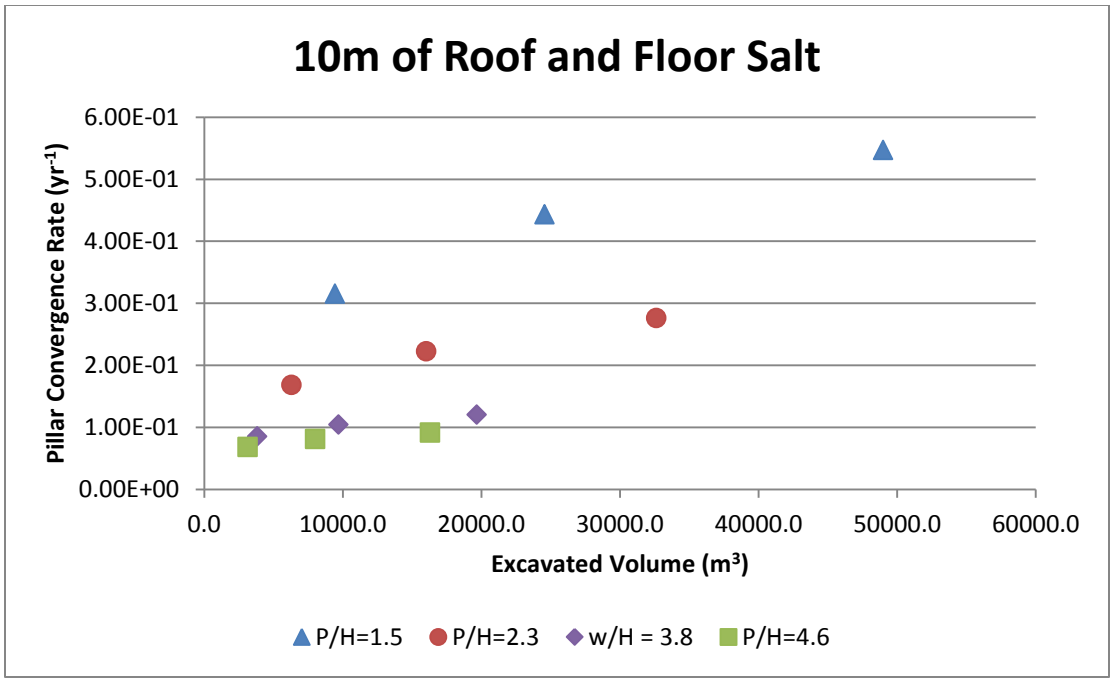
10m of Roof and Floor Salt
Pillar Convergence Rate (yr-1)
6.00E-01
5.00E-01
4.00E-01
3.00E-01
2.00E-01
1.00E-01
0.00E+00
0.0
10000.0
20000.0
30000.0
40000.0
50000.0
60000.0
Excavated Volume (m3)
P/H=1.5
P/H=2.3
w/H = 3.8
P/H=4.6

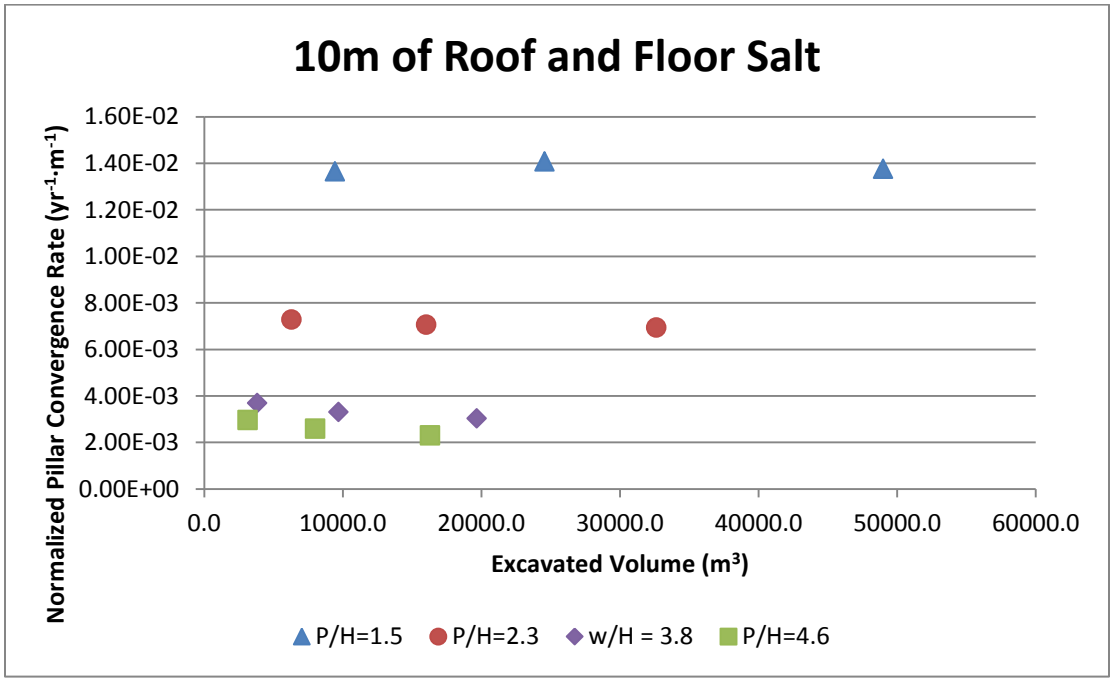
10m of Roof and Floor Salt
Normalized Pillar Convergence Rate (yr-1·m-1)
1.60E-02
1.40E-02
1.20E-02
1.00E-02
8.00E-03
6.00E-03
4.00E-03
2.00E-03
0.00E+00
0.0
10000.0
20000.0
30000.0
40000.0
50000.0
60000.0
Excavated Volume (m3)
P/H=1.5
P/H=2.3
w/H = 3.8
P/H=4.6

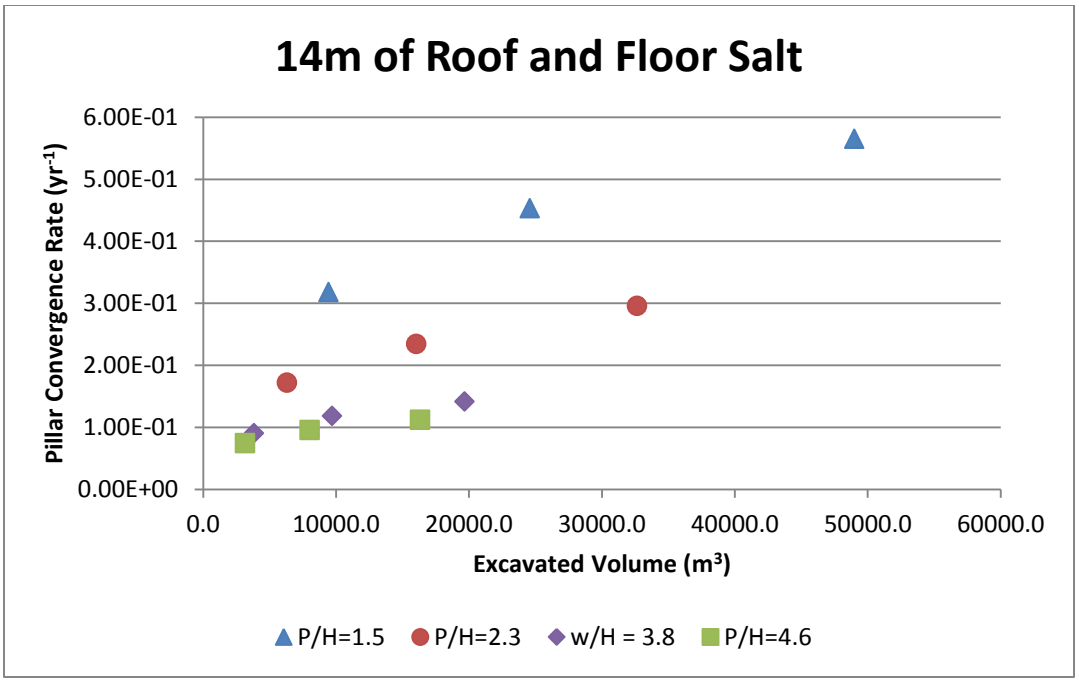
14m of Roof and Floor Salt
Pillar Convergence Rate (yr-1)
6.00E-01
5.00E-01
4.00E-01
3.00E-01
2.00E-01
1.00E-01
0.00E+00
0.0
10000.0
20000.0
30000.0
40000.0
50000.0
60000.0
Excavated Volume (m3)
P/H=1.5
P/H=2.3
w/H = 3.8
P/H=4.6

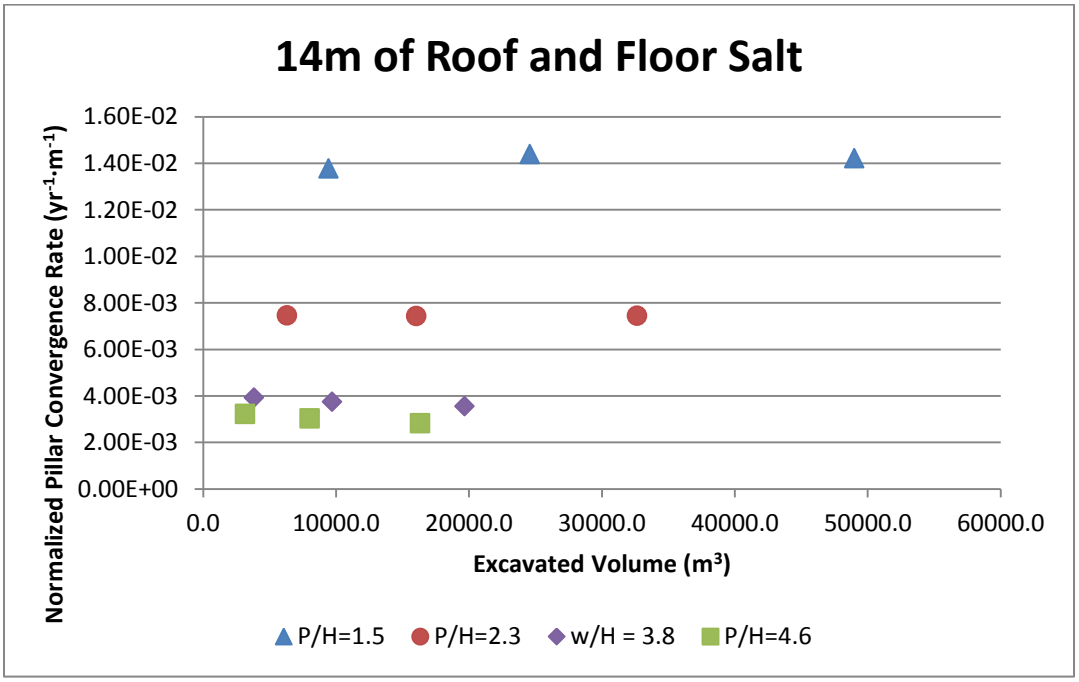
14m of Roof and Floor Salt
Normalized Pillar Convergence Rate (yr-1·m-1)
1.60E-02
1.40E-02
1.20E-02
1.00E-02
8.00E-03
6.00E-03
4.00E-03
2.00E-03
0.00E+00
0.0
10000.0
20000.0
30000.0
40000.0
50000.0
60000.0
Excavated Volume (m3)
P/H=1.5
P/H=2.3
w/H = 3.8
P/H=4.6

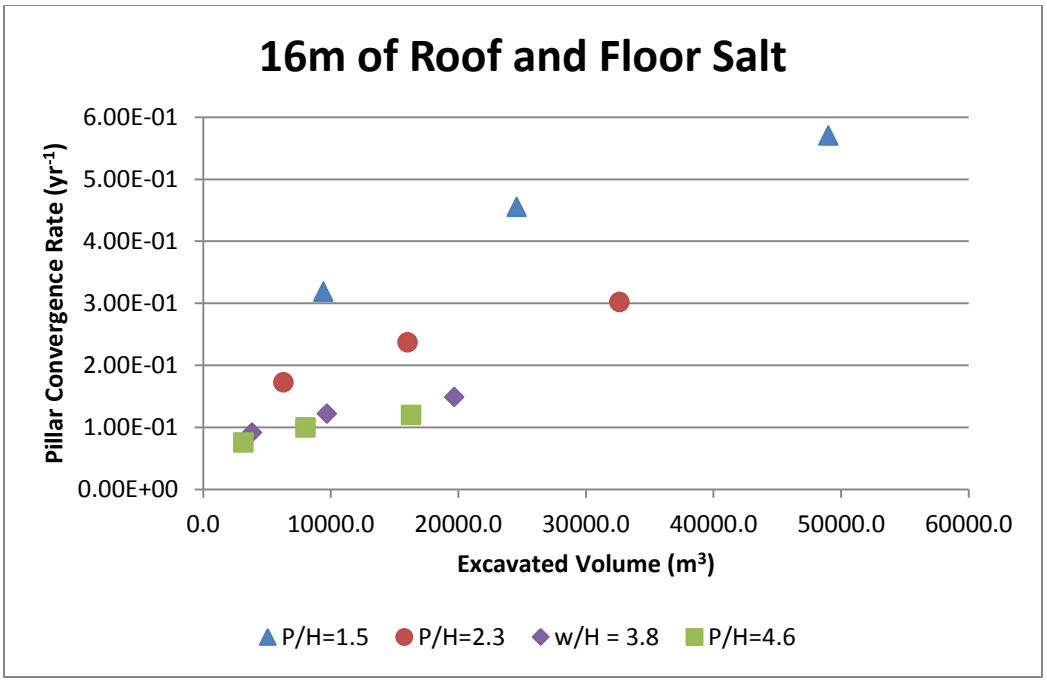
16m of Roof and Floor Salt
Pillar Convergence Rate (yr-1)
6.00E-01
5.00E-01
4.00E-01
3.00E-01
2.00E-01
1.00E-01
0.00E+00
0.0
10000.0
20000.0
30000.0
40000.0
50000.0
60000.0
Excavated Volume (m3)
P/H=1.5
P/H=2.3
w/H = 3.8
P/H=4.6

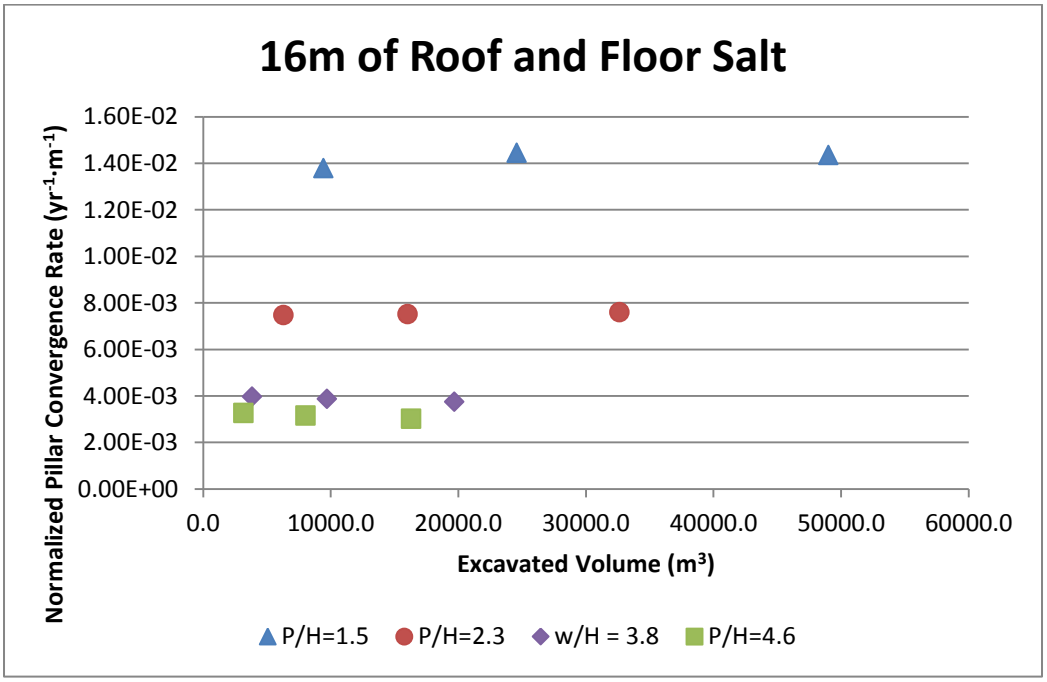
16m of Roof and Floor Salt
Normalized Pillar Convergence Rate (yr-1·m-1)
1.60E-02
1.40E-02
1.20E-02
1.00E-02
8.00E-03
6.00E-03
4.00E-03
2.00E-03
0.00E+00
0.0
10000.0
20000.0
30000.0
40000.0
50000.0
60000.0
Excavated Volume (m3)
P/H=1.5
P/H=2.3
w/H = 3.8
P/H=4.6

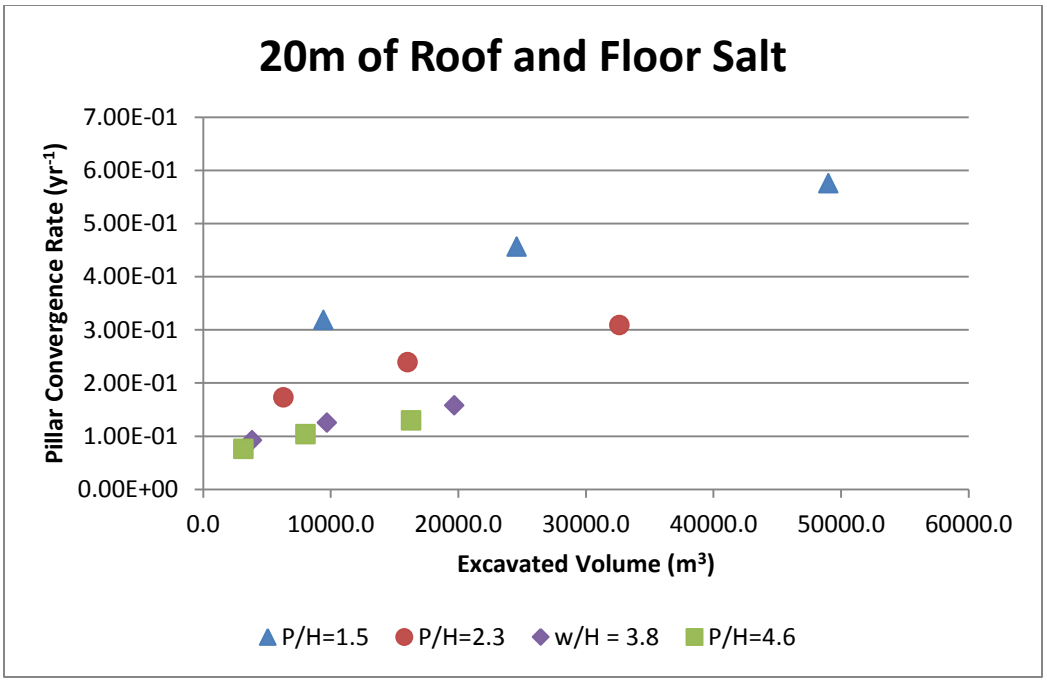
20m of Roof and Floor Salt
Pillar Convergence Rate (yr-1)
7.00E-01
6.00E-01
5.00E-01
4.00E-01
3.00E-01
2.00E-01
1.00E-01
0.00E+00
0.0
10000.0
20000.0
30000.0
40000.0
50000.0
60000.0
Excavated Volume (m3)
P/H=1.5
P/H=2.3
w/H = 3.8
P/H=4.6

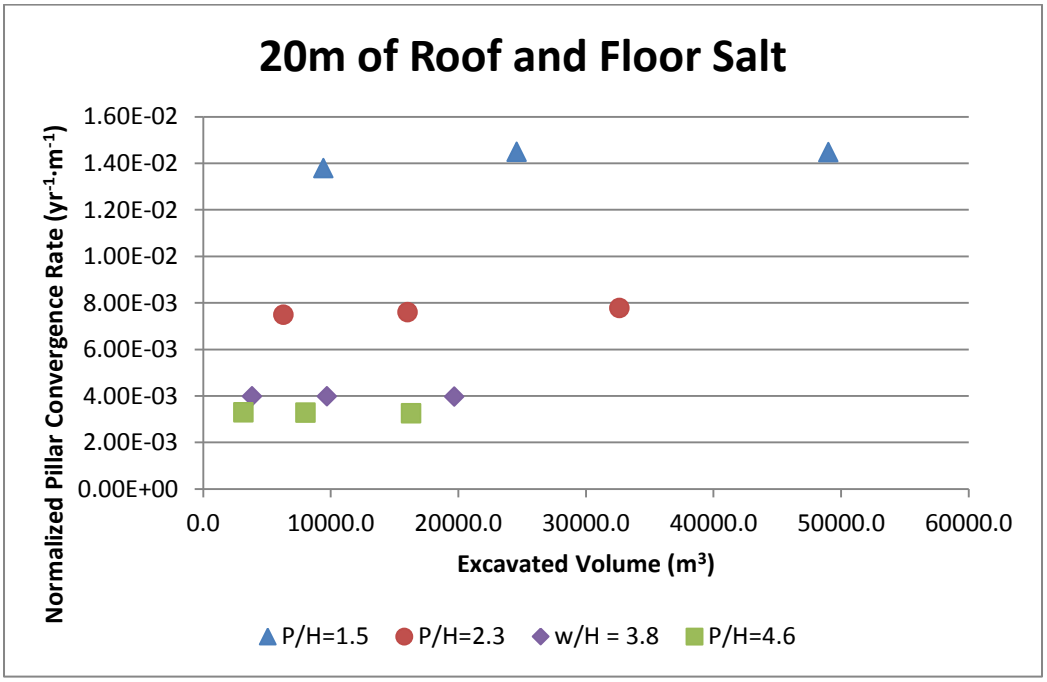
20m of Roof and Floor Salt
Normalized Pillar Convergence Rate (yr-1·m-1)
1.60E-02
1.40E-02
1.20E-02
1.00E-02
8.00E-03
6.00E-03
4.00E-03
2.00E-03
0.00E+00
0.0
10000.0
20000.0
30000.0
40000.0
50000.0
60000.0
Excavated Volume (m3)
P/H=1.5
P/H=2.3
w/H = 3.8
P/H=4.6

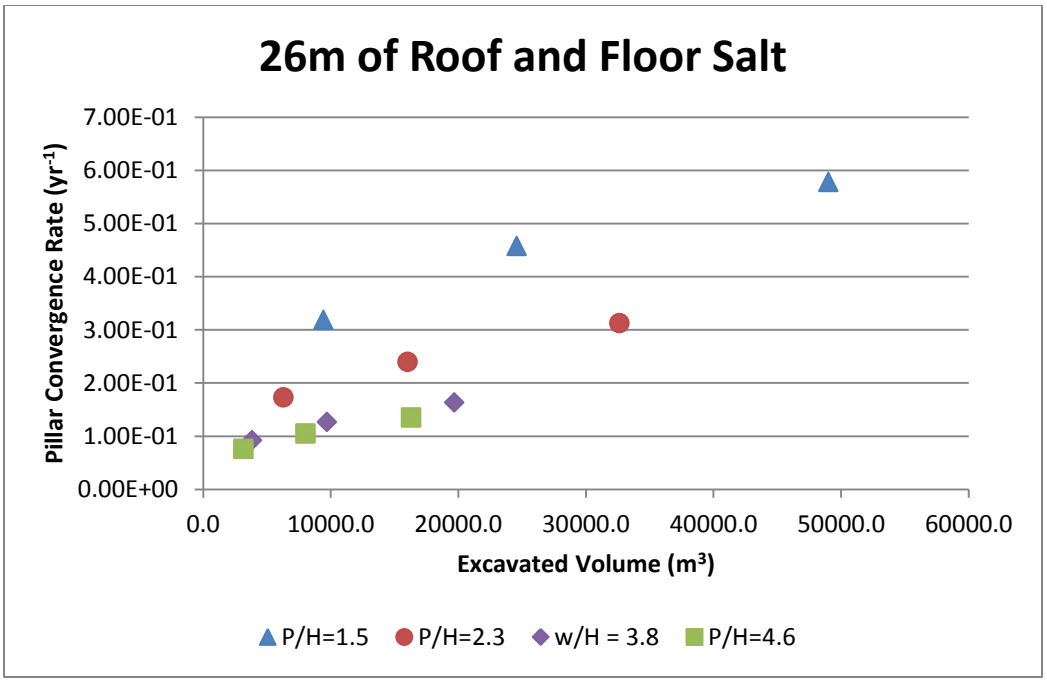
26m of Roof and Floor Salt
Pillar Convergence Rate (yr-1)
7.00E-01
6.00E-01
5.00E-01
4.00E-01
3.00E-01
2.00E-01
1.00E-01
0.00E+00
0.0
10000.0
20000.0
30000.0
40000.0
50000.0
60000.0
Excavated Volume (m3)
P/H=1.5
P/H=2.3
w/H = 3.8
P/H=4.6

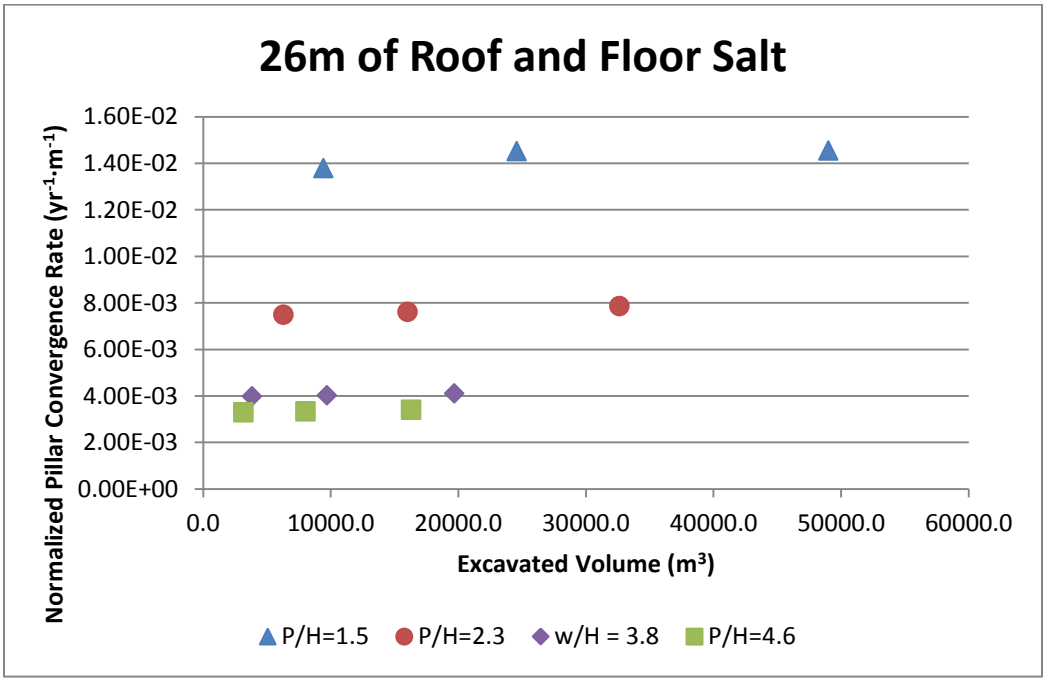
26m of Roof and Floor Salt
Normalized Pillar Convergence Rate (yr-1·m-1)
1.60E-02
1.40E-02
1.20E-02
1.00E-02
8.00E-03
6.00E-03
4.00E-03
2.00E-03
0.00E+00
0.0
10000.0
20000.0
30000.0
40000.0
50000.0
60000.0
Excavated Volume (m3)
P/H=1.5
P/H=2.3
w/H = 3.8
P/H=4.6